



ARISTOTLE UNIVERSITY OF THESSALONIKI

# **Search for New Physics in the Diboson WZ Production Mode with the ATLAS detector**

Panagiotis Ziakas

A thesis submitted in partial fulfillment for the degree of  
Master in Science

in the  
Faculty of Sciences  
School of Physics

Supervising Professor: Chara Petridou

July, 2024

# Declaration of Authorship

I, Panagiotis Ziakas, declare that this thesis titled, Search for New Physics in the Diboson WZ Production Mode with the ATLAS detector and the work presented in it are my own. I confirm that:

- This work was done wholly or mainly while in candidature for a research degree at this University.
- Where any part of this thesis has previously been submitted for a degree or any other qualification at this University or any other institution, this has been clearly stated.
- Where I have consulted the published work of others, this is always clearly attributed.
- Where I have quoted from the work of others, the source is always given. With the exception of such quotations, this thesis is entirely my own work.
- I have acknowledged all main sources of help.
- Where the thesis is based on work done by myself jointly with others, I have made clear exactly what was done by others and what I have contributed myself.

Signed:

---

Date:

---

*On and on through eternity  
Pathways through the galaxies  
We were, we are, will we be?  
Will our cries be heard or echo endlessly?*

**Oblivion, Black Future, Vektor, 2009**

# Abstract

Standard Model has been proven to be the most successful theory in interpreting the majority of the experimental data obtained from our detectors. However, unsolved problems do exist, giving rise to new theories that might lead us to the discoveries of New Physics. Aim of this thesis is to search for New Physics via the Heavy Vector Triplets Model, which predicts a charged, spin-1  $W'$  boson. More specifically, this thesis focuses on the study of resonant WZ diboson production, decaying into leptonic final states (electrons or muons).

First of all, a brief overview of the SM particles, the formalism of the Higgs Mechanism, as well as the beyond SM theory of the HVT are presented. Next, the main characteristics of the Large Hadron Collider and the ATLAS detector are described, followed by a brief discussion of the data and MC samples used in this analysis. Moreover, the determination of some basic kinematic variables, the event selection criteria for the WZ Inclusive phase space, as well as the definition of the Drell-Yan SR are presented. The main backgrounds associated with the diboson WZ production, the selection criteria for the dedicated CRs and the estimation of the normalization factors for each one, are also presented. Additionally, the post-fit background distributions along with a signal candidate in the Drell-Yan SR are presented and statistical process of extracting 95% CL upper limits is discussed. Finally, the extracted 95% CL upper limits plots are presented, as well as comparison plots for the observed and expected limits.

# Περίληψη

Το Καθιερωμένο Πρότυπο της σωματιδιακής φυσικής είναι η πιο επιτυχημένη φυσική θεωρία η οποία υπάρχει μέχρι σήμερα, όσον αφορά την εξήγηση της πλειονότητας των πειραματικών δεδομένων που λαμβάνουμε από τους ανιχνευτές μας. Ωστόσο, υπάρχουν φυσικά φαινόμενα τα οποία το Καθιερωμένο Πρότυπο δεν μπορεί να εξηγήσει, δίνοντας έναυσμα σε νέες φυσικές θεωρίες πέραν του Καθιερωμένου Προτύπου, με σκοπό την αναζήτηση Νέας Φυσικής. Σκοπός της παρούσας διπλωματικής εργασίας είναι η αναζήτηση Νέας Φυσικής μέσω της θεωρίας Heavy Vector Triplet Model, η οποία προβλέπει ένα φορτισμένο, spin-1  $W'$  μποζόνιο. Πιο συγκεκριμένα, η παρούσα διπλωματική εργασία στοχεύει στην μελέτη συντονισμών που προέρχονται από την παραγωγή WZ μποζονίων, τα οποία διασπώνται λεπτονικά (ηλεκτρόνια και μύονια).

Αρχικά, γίνεται μια σύντομη περιγραφή του Καθιερωμένου Προτύπου, παρουσιάζεται ο φορμαλισμός του Μηχανισμού Higgs καθώς και το θεωρητικό πλαίσιο της θεωρίας Heavy Vector Triplet Model. Στην συνέχεια, περιγράφονται τα κύρια χαρακτηριστικά του Large Hadron Collider και του ανιχνευτή ATLAS, όπως επίσης και τα data και Monte Carlo δείγματα τα οποία χρησιμοποιήθηκαν σε αυτή την ανάλυση. Επίσης, παρουσιάζονται η μεθοδολογία υπολογισμού βασικών κινηματικών μεταβλητών, τα κριτήρια επιλογής για την διαμόρφωσης του WZ Inclusive Phase Space, καθώς και ο ορισμός της Drell-Yan Signal Region. Στην συνέχεια, παρουσιάζονται οι κύριες διαδικασίες υποβάθρου που σχετίζονται με την παραγωγή των W και Z μποζονίων, τα κριτήρια επιλογής για τις Control Regions και η εκτίμηση των παραγόντων κανονικοποίησης για κάθε μια από αυτές. Ακόμα, παρουσιάζονται οι post-fit κατανομές μαζί με μια πιθανή κατανομή της διεργασίας σήματος στην Drell-Yan Signal Region, καθώς και η στατιστική διαδικασία υπολογισμού 95% CL άνω ορίων. Τέλος, παρουσιάζονται τα διαγράμματα 95% CL άνω ορίων, καθώς και διαγράμματα σύγκρισης ανάμεσα σε παρατηρούμενα και αναμενόμενα άνω όρια.

# Acknowledgements

First and foremost, I would like to express my deepest gratitude to my supervising professor, Chara Petridou. I would like to thank her for all the knowledge she shared with me, for her eagerness to answer my countless at times questions, for the constant support and belief she showed in me, even from our very first encounter. Without her patient and enlightening guidance, the completion of this thesis would not have been feasible.

Also, I owe a big thank you to Maria-Evanthia Tsopoulou (PhD, ATh), Eirini Kasimi (Postdoctoral Researcher, ATh), Dimitra Amperiadou (PhD candidate), and Konstantinos Bachas (Associate Professor, UTh) . I am grateful for the time they spent helping me with all the technical issues that came up during the preparation of this thesis, as well as for clarifying many parts of the procedure that make up a Particle Physics analysis. Without their input, this thesis would have been far from complete.

Moreover, I would like to thank my family for all their love and support during my studies. Thank you for all the sacrifices you have made for me, for always encouraging me to pursue my dream, and for letting me share with you my sheer enthusiasm and passion for the subatomic realm.

Last but not least, I would like to thank all the professors who managed to inspire me, throughout my years of being a high-school, undergraduate and postgraduate student. Thank you for inspiring me to study Physics, and eventually leading me to fall in love with Particle Physics.

Dear music, thank you for lifting me up when I was at the verge of quitting.

## CONTENTS

<b>Declaration of Authorship</b>	<b>i</b>
<b>Abstract</b>	<b>iii</b>
<b>Περίληψη</b>	<b>iv</b>
<b>Acknowledgements</b>	<b>v</b>
<b>List of Figures</b>	<b>ix</b>
<b>List of Tables</b>	<b>xii</b>
<b>Abbreviations</b>	<b>xiii</b>
<b>1 Introduction</b>	<b>1</b>
<b>2 Theoretical Introduction</b>	<b>3</b>
2.1 Brief Description of the Standard Model . . . . .	3
2.1.1 Elementary particles . . . . .	3
2.1.2 Fermions . . . . .	3
2.1.3 Bosons . . . . .	4
2.2 The Higgs Mechanism . . . . .	6
2.2.1 The need for the Higgs Boson . . . . .	6
2.2.2 Spontaneous Symmetry Breaking . . . . .	7
2.2.3 Complex Scalar Field . . . . .	9
2.2.4 The Higgs Mechanism under a U(1) local gauge symmetry . . .	12
2.2.5 The Standard Model Higgs . . . . .	16
2.3 Beyond Standard Model Theories . . . . .	21
2.3.1 Heavy Vector Triplet Model . . . . .	22
<b>3 The Large Hadron Collider and the ATLAS detector</b>	<b>26</b>

3.1	The Large Hadron Collider . . . . .	26
3.2	The ATLAS detector . . . . .	28
3.2.1	ATLAS structure . . . . .	28
3.2.2	ATLAS coordinate system . . . . .	29
<b>4</b>	<b>Data and Monte Carlo Samples</b>	<b>31</b>
4.1	Data Samples . . . . .	31
4.2	Monte-Carlo Signal Samples . . . . .	31
4.3	Monte-Carlo Background Samples . . . . .	32
<b>5</b>	<b>Event Selection</b>	<b>34</b>
5.1	Determination of basic variables . . . . .	34
5.1.1	WZ system Invariant Mass . . . . .	34
5.1.2	W boson and WZ system Transverse Mass . . . . .	35
5.2	Inclusive WZ event selection . . . . .	36
5.3	WZ Inclusive Control Distributions . . . . .	37
5.4	Drell-Yan Signal Region Definition . . . . .	39
<b>6</b>	<b>Background Estimation</b>	<b>41</b>
6.1	Reducible Background . . . . .	41
6.2	Irreducible Background . . . . .	42
6.3	Drell-Yan Control Regions . . . . .	43
6.4	The Binned Maximum Likelihood Model . . . . .	43
6.5	ZZ Drell-Yan Control Region . . . . .	44
6.6	WZ-QCD Drell Yan Control Region . . . . .	49
6.7	Incorporating a Systematic Uncertainty . . . . .	54
6.8	Simultaneous Maximum Likelihood Fit . . . . .	58
<b>7</b>	<b>Drell-Yan Signal Region</b>	<b>61</b>
7.1	Drell-Yan Signal Region Distributions . . . . .	61
7.2	Estimating the signal strength parameter . . . . .	63
7.3	Drell-Yan Signal Region Post-Fit Yields . . . . .	65
<b>8</b>	<b>Statistical Methods for upper limits</b>	<b>67</b>
8.1	Definition of a statistical test . . . . .	67
8.2	Test Statistic for upper limits . . . . .	68
8.3	Asymptotic Approximations . . . . .	69
8.4	The Asimov dataset and the variance of $\hat{\mu}$ . . . . .	70
8.5	The $CL_s$ method . . . . .	71
8.5.1	Observed Limits . . . . .	72
8.5.2	Expected Limits . . . . .	73
<b>9</b>	<b>Results</b>	<b>75</b>
9.1	Limits . . . . .	75
9.2	Observed and expected limits comparison . . . . .	80



<b>10 Conclusions</b>	<b>82</b>
<b>A Signal Monte Carlo Samples</b>	<b>83</b>
<b>B Hypothesis Testing</b>	<b>84</b>
<b>C The Maximum Likelihood Method</b>	<b>86</b>
 <b>Bibliography</b>	 <b>89</b>

## LIST OF FIGURES

2.1.1	Brief overview of the Standard Model Particles and their fundamental properties. . . . .	5
2.2.1	The three point interaction vertex in QED (left) and the four point interaction vertex for the scalar field $\phi$ (right). . . . .	7
2.2.2	The potential $V(\phi)$ for $\lambda > 0$ and the cases $\mu^2 > 0$ (a) and $\mu^2 < 0$ (b). . . . .	8
2.2.3	The triple and quartic vertices of the field $\eta$ . . . . .	9
2.2.4	The potential $V(\phi)$ for $\lambda > 0$ and the cases $\mu^2 > 0$ (a) and $\mu^2 < 0$ (b). . . . .	10
2.2.5	The triple and quartic vertices of the fields $\eta$ and $\xi$ . . . . .	11
2.2.6	Field $\eta(x)$ and $\xi(x)$ with respect to the vacuum state. . . . .	12
2.2.7	The interactions of the Higgs boson under a U(1) local gauge symmetry. . . . .	16
2.2.8	The $W^+W^-H$ and $ZZH$ vertices, with their couplings. . . . .	21
2.3.1	Feynman diagram of the $W'$ production via the Drell-Yan process, its decay to W and Z bosons and the subsequent production of $l^+l^-l^\pm\nu$ . . . . .	25
3.1.1	LHC acceleration complex. . . . .	27
3.2.1	The ATLAS detector and its main components. . . . .	29
3.2.2	The coordinate system of the ATLAS detector. . . . .	30
3.2.3	The correspondence between $\eta$ and the polar angle $\theta$ . . . . .	30
5.3.1	Control distributions of Z boson mass $m_Z$ (upper left), W boson transverse mass $m_T^W$ (upper right), missing transverse energy $E_T^{miss}$ (down left) and WZ system transverse mass $m_T^{WZ}$ (down right). All MC expectations are scaled to the scaling factor of 5.3.0.1. . . . .	37
5.3.2	Control distributions of PtBalanceZ $p_T^Z/m_{WZ}$ (upper left), PtBalanceW $p_T^W/m_{WZ}$ (upper right), first and third lepton transverse momenta $p_T^{Lep1}$ (down left) and $p_T^{Lep3}$ (down right). . . . .	38
5.3.3	Control distributions of first and third lepton pseudorapidities $\eta^{Lep1}$ (upper left) and $\eta^{Lep3}$ (upper right) and the pseudorapidities of the Z and W bosons $\eta^Z$ (down left) and $\eta^W$ (down right). . . . .	38
5.3.4	Control distributions of the W and Z bosons transverse momenta $p_T^Z$ (upper left) and $p_T^W$ (upper right), the transverse momentum of the WZ system $p_T^{WZ}$ (down left) and the invariant mass of the WZ system $m_{WZ}$ (down right). . . . .	39
5.4.1	WZ QCD background versus various Drell-Yan signals for PtBalanceZ normalized to unit. . . . .	40

5.4.2 WZ QCD background versus various Drell-Yan signals for PtBalanceW normalized to unit. . . . .	40
6.5.1 Pre-fit $m_{WZ}$ distribution in the ZZ Drell-Yan CR. . . . .	44
6.5.2 Pre-fit $Sum3Pt$ distribution in the ZZ Drell-Yan CR. . . . .	45
6.5.3 Pre-fit $m_{WZ}^T$ distribution in the ZZ Drell-Yan CR. . . . .	45
6.5.4 $\mu_{ZZ}$ NLL ratio estimation using $m_{WZ}$ as input. . . . .	46
6.5.5 $\mu_{ZZ}$ NLL ratio estimation using $Sum3Pt$ as input. . . . .	46
6.5.6 $\mu_{ZZ}$ NLL ratio estimation using $m_{WZ}^T$ as input. . . . .	47
6.5.7 Post-fit $m_{WZ}$ distribution in the ZZ Drell-Yan CR. . . . .	47
6.5.8 Post-fit $Sum3Pt$ distribution in the ZZ Drell-Yan CR. . . . .	48
6.5.9 Post-fit $m_{WZ}^T$ distribution in the ZZ Drell-Yan CR. . . . .	48
6.6.1 Pre-fit $m_{WZ}$ distribution in the WZ-QCD Drell-Yan CR. . . . .	49
6.6.2 Pre-fit $Sum3Pt$ distribution in the WZ-QCD Drell-Yan CR. . . . .	50
6.6.3 Pre-fit $m_{WZ}^T$ distribution in the WZ-QCD Drell-Yan CR. . . . .	50
6.6.4 $\mu_{WZ}^{QCD}$ NLL ratio estimation using $m_{WZ}$ as input. . . . .	51
6.6.5 $\mu_{WZ}^{QCD}$ NLL ratio estimation using $Sum3Pt$ as input. . . . .	51
6.6.6 $\mu_{WZ}^{QCD}$ NLL ratio estimation using $m_{WZ}^T$ as input. . . . .	52
6.6.7 Post-fit $m_{WZ}$ distribution in the WZ-QCD Drell-Yan CR. . . . .	52
6.6.8 Post-fit $Sum3Pt$ distribution in the WZ-QCD Drell-Yan CR. . . . .	53
6.6.9 Post-fit $m_{WZ}^T$ distribution in the WZ-QCD Drell-Yan CR. . . . .	53
6.7.1 $\mu_{ZZ}$ PLR ratio estimation using $m_{WZ}$ as input. . . . .	55
6.7.2 $\mu_{ZZ}$ PLR ratio estimation using $Sum3Pt$ as input. . . . .	56
6.7.3 $\mu_{ZZ}$ PLR ratio estimation using $m_{WZ}^T$ as input. . . . .	56
6.7.4 $\mu_{WZ}^{QCD}$ PLR ratio estimation using $m_{WZ}$ as input. . . . .	57
6.7.5 $\mu_{WZ}^{QCD}$ PLR ratio estimation using $Sum3Pt$ as input. . . . .	57
6.7.6 $\mu_{WZ}^{QCD}$ PLR ratio estimation using $m_{WZ}^T$ as input. . . . .	58
6.8.1 Pre-fit $m_{WZ}$ distribution in the Drell-Yan SR. . . . .	59
6.8.2 Pre-fit $Sum3Pt$ distribution in the Drell-Yan SR. . . . .	59
6.8.3 Pre-fit $m_{WZ}^T$ distribution in the Drell-Yan SR. . . . .	60
7.1.1 Postfit $m_{WZ}$ distribution in the Drell-Yan SR. . . . .	61
7.1.2 Postfit $Sum3Pt$ distribution in the Drell-Yan SR. . . . .	62
7.1.3 Postfit $m_{WZ}^T$ distribution in the Drell-Yan SR. . . . .	62
7.2.1 Signal Strength parameter $\mu$ NLL ratio estimation using $m_{WZ}$ as input. . . . .	63
7.2.2 Signal Strength parameter $\mu$ NLL ratio estimation using $Sum3Pt$ as input. . . . .	64
7.2.3 Signal Strength parameter $\mu$ NLL ratio estimation using $m_{WZ}^T$ as input. . . . .	64
8.5.1 Demonstration of the p-values associated with the signal plus background hypothesis and the background only hypothesis. . . . .	72
9.1.1 Observed and expected limits on the cross section multiplied by the branching fraction, using $m_{WZ}$ as input. . . . .	76
9.1.2 Observed and expected limits on the cross section multiplied by the branching fraction, using $Sum3Pt$ as input. . . . .	77

9.1.3	Observed and expected limits on the cross section multiplied by the branching fraction, using $m_{WZ}^T$ as input. . . . .	77
9.1.4	Correlation plot between $m_{3l}$ and $p_{3l}^T$ . . . . .	78
9.1.5	Unrolled distributions obtained from $m_{3l}$ and $p_{3l}^T$ . . . . .	79
9.1.6	Observed and expected limits on the cross section multiplied by the branching fraction, using $m_{3l}$ and $p_{3l}^T$ as input. . . . .	79
9.2.1	Observed limits comparison for different variables in the Drell-Yan SR.	80
9.2.2	Expected limits comparison for different variables in the Drell-Yan SR.	80
B.0.1	Illustration of the type one error probability $\alpha$ , type two error probability $\beta$ and power $1 - \beta$ of a statistical test. . . . .	85
C.0.1	The variance of the Least Squares estimator using the graphical method.	87

## LIST OF TABLES

5.2.1 The analysis' event selection criteria . . . . .	36
6.2.1 Selection Criteria for the Drell-Yan SR and the dedicated CRs. . . . .	42
7.3.1 Expected and Observed total post-fit events in the Drell-Yan SR, obtained from the $m_{WZ}$ distributions. . . . .	65
7.3.2 Expected and Observed total post-fit events in the Drell-Yan SR, obtained from the $Sum3Pt$ distributions. . . . .	65
7.3.3 Expected and Observed total post-fit events in the Drell-Yan SR, obtained from the $m_{WZ}^T$ distributions. . . . .	66
A.0.1 Summary of the HVT signal samples used in the analysis. . . . .	83

## ABBREVIATIONS

<b>SM</b>	<b>Standard Model</b>
<b>MC</b>	<b>Monte Carlo</b>
<b>SR</b>	<b>Signal Region</b>
<b>CR</b>	<b>Control Region</b>
<b>NLL</b>	<b>Negative Log Likelihood</b>
<b>PLR</b>	<b>Profile Likelihood Ratio</b>
<b>CL</b>	<b>Confidence Level</b>
<b>HVT</b>	<b>Heavy Vector Triplet</b>
<b>LO</b>	<b>Leading Order</b>

# CHAPTER 1

## INTRODUCTION

Since the dawn of philosophy, one of the most fundamental questions we have posed to ourselves as humanity, is what are we comprised of. The curiosity of mankind for the structure of matter dates back to era of Ancient Greek and Ancient Indian civilizations. The natural theory of Atomism is a natural philosophy that proposes that the Universe is composed of fundamental invisible components known as atoms. References to the concept of Atomism are found in both the Ancient Greek and Ancient Indian philosophical traditions. In fact, Leucippus, who was an Ancient Greek philosopher and is usually credited as the pioneer of Atomism, theorized that nature consists of two fundamental components: *atoms and void*.

As the centuries went by, natural sciences made huge progress in describing the laws that permeate our Universe and succeeded in making accurate predictions about the mechanics of nature. As a result, the initial philosophical question, quickly disintegrated into a challenge that natural sciences had to face and overcome. Out of all the natural sciences, Physics has to address some of the most important and complex scientific issues. One of them is what are the most fundamental constituents of our Universe, and how do they interact with each other to bind us together.

Our current understanding of the building blocks of our Universe is both complex and counter-intuitive. Particles are described as quantum excitations of fields. The laws that govern their interactions are described by **Quantum Field Theory**, which is a theory that combines **Quantum Mechanics** and **Special Relativity** in order to describe the subatomic particles moving at speeds close to the speed of light.

All the known particles and models that describe the fundamental forces of nature are assembled into a single theory, known as the **Standard Model**. SM is the most accurate theory that describes the behaviour of the subatomic realm and has been tested

experimentally with great success. The latest triumph of the SM was the prediction of the Higgs boson, which was discovered experimentally in 2012 by the ATLAS and CMS experiments at the Large Hadron Collider (LHC) at CERN near Geneva, Switzerland.

However, despite its experimental success, SM is not a complete theory. Several physical phenomena still remain unexplained such as the origin of the neutrinos' masses, dark matter and dark energy or a quantum theory of gravity. These "holes" in SM have given rise to many beyond SM theories, in order to enhance our understanding of the subatomic world and predict the existence of possible new particles.

The present thesis concentrates in the probe of new Physics via resonance searches that come from beyond SM theories. More specifically, we have studied the existence of heavy resonances that arise from the **Heavy Vector Triplet** model via the **Drell-Yan** process. These heavy resonances decay into a W and a Z boson, producing three leptons (electrons and muons) plus a neutrino. The data that were used to perform the study were collected by the ATLAS experiment at the Large Hadron Collider (LHC) at a center of mass energy of 13 TeV, corresponding to an integrated luminosity of  $139\text{ fb}^{-1}$ .

A brief presentation of the thesis' structure is follows below.

In **Chapter 2**, a brief overview of the SM particles, the formalism of the Higgs Mechanism, as well as the beyond SM theory of the HVT are presented. In **Chapter 3**, the main characteristic of the Large Hadron Collider and the ATLAS detector are described. **Chapter 4** briefly discusses the data and MC samples used in this analysis. In **Chapter 5**, some of the basic kinematic variables are determined and the event selection criteria for the WZ Inclusive phase space, as well as the definition of the Drell-Yan SR are presented. **Chapter 6** discusses the backgrounds associated with the diboson WZ production, shows the selection criteria for the dedicated CRs and presents the estimation of the normalization factors for each one. **Chapter 7** shows the background distributions along with a signal candidate in the Drell-Yan SR and presents the post-fit expected and observed events. In **Chapter 8**, the statistical process of extracting upper limits is discussed. Finally, in **Chapter 9**, the extracted 95% CL upper limits plots are presented, as well as comparison plots for the observed and expected limits.



## THEORETICAL INTRODUCTION

### 2.1 Brief Description of the Standard Model

As stated in **Chapter 1**, **Standard Model** is currently the best theory that describes the physical laws that govern the subatomic particles. It can be characterized as a well-tested physics theory, due to its success in interpreting all the experimental data that have been acquired so far.

#### 2.1.1 Elementary particles

Up until now, we are aware of the existence of 17 elementary particles. These particles are characterized as elementary, due to fact that they are not made of other particles and therefore, they constitute the most fundamental building blocks of our Universe. Elementary particles can be split into two big categories: **fermions** and **bosons**.

#### 2.1.2 Fermions

Particles that have half-integer spin, and thus obey Fermi-Dirac Statistics, are named fermions. Fermions can be further split into two categories: **quarks** and **leptons**. Each of these categories is comprised of six particles. The six quarks come in groups of three, where the first three are called "up type", where the other three are called "down type". Up type quarks consist of the "up quark", the "charm quark" and the "top quark", where the order used is ascending with respect to their mass. Down type quarks consist of the "down quark", the "strange quark" and the "bottom quark", where

again the order is ascending with respect to their mass.

Leptons on the other hand, are also comprised of six particles. Once again using an ascending mass order, leptons consist of the "electron", the "muon" and the "tau". All of these three particles have their corresponding neutrino, "electron neutrino", "muon neutrino" and "tau neutrino". Whilst neutrinos are thought to be massless according to SM, an extremely interesting phenomenon called neutrino oscillations, which has been verified experimentally, has proven once and for all that neutrinos do have a small mass.

### 2.1.3 Bosons

Particles that have integer spin, and thus obey Bose-Einstein Statistics, are named bosons. Bosons are responsible for mediating the four fundamental forces of Nature: the electromagnetic force, the gravitational force, the strong force and the weak force. According to **Quantum Field Theory**, forces are comprehended via the virtual particle exchange. A matter particle emits a virtual force-carrying boson, which is later absorbed by another matter particle. Therefore, the first particle transfers momentum to the other particle. This change in momentum for both particles manifests itself as a force.

Each of the forces has its own mediator. The electromagnetic force, is the force that is experienced by particles that carry the property of electric charge, and is described by **QED** (Quantum ElectroDynamics). Its mediator is the photon ( $\gamma$ ), which is massless and carries no electric charge. As a matter of fact, photons do not interact with each other via the electromagnetic force.

The strong force, is the force that is experienced by particles that carry the property of colour, and is described by **QCD** (Quantum ChromoDynamics). Its mediators are the eight gluons ( $g$ ), which are massless and carry color charge. As a matter of fact, gluons do interact with each other via the strong force. These interactions between gluons are thought to be responsible for the color confinement, which states that particles that carry color charge cannot be free particles.

The weak force, which is responsible for the radioactive beta decay, is mediated through the  $W^{\pm}$  and  $Z$  bosons. Whilst the weak force is intrinsically stronger than the electromagnetic force, its probability of occurring is inversely dependent to the fourth

power of the mediator's mass. Since  $W^\pm$  and  $Z$  bosons are very massive, this dependence suppresses the probability of the weak force to occur, and thus it is considered as weak. However, the weak force plays a vital role in our Universe's existence because it violates an important symmetry, known as the CP symmetry. This symmetry violation is known as the CP violation and produces a slight asymmetry in the production of matter versus antimatter in the early Universe. Hence, we exist, because this force exists.

The gravitational force, which is the most common force of our daily experience, is thought to be mediated through a spin-2 boson, called the graviton. However, this is only a speculation due to our inability to describe gravity with a quantum theory.

Last but not least, the final piece of the SM is the Higgs boson. The Higgs boson is a massive particle responsible for giving mass to all the elementary particles, by breaking the Electroweak symmetry. Without the Higgs boson, there would be no stable structure in our Universe.

A brief overview of the SM particles is given in **Figure 2.1.1**:

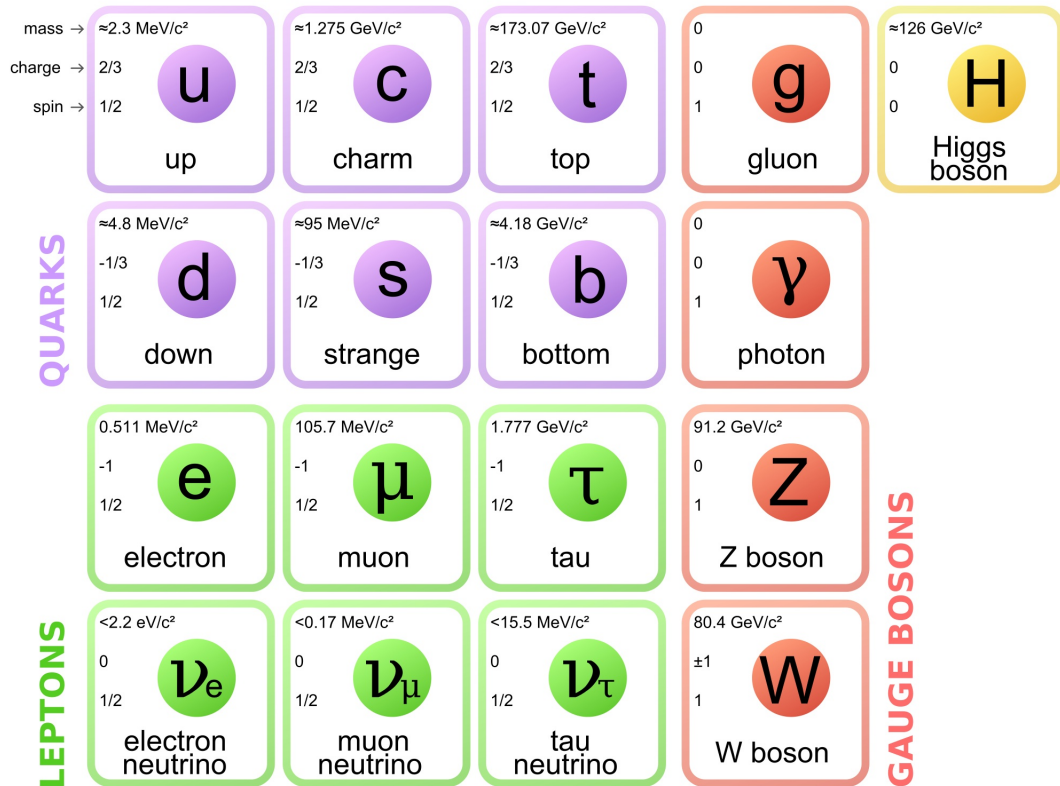


FIGURE 2.1.1: Brief overview of the Standard Model Particles and their fundamental properties.

## 2.2 The Higgs Mechanism

### 2.2.1 The need for the Higgs Boson

The Higgs mechanism is not predicted by the Standard Model. Instead, it is a theory that has been inserted in the Standard Model, in order to preserve its local gauge invariance. It has been shown mathematically that only gauge invariant theories are renormalisable. However, as we are about to show below, if the Lagrangians that describe the interactions between particles and gauge bosons contain mass terms, they are not invariant under a local gauge transformation. As described in [18], the Lagrangian that describes the electron field, the photon field, and the interactions between them is given by:

$$\mathcal{L}_{QED} = \bar{\psi} (\gamma^\mu \partial_\mu - m_e) \psi + e \bar{\psi} \gamma^\mu \psi A_\mu - \frac{1}{4} F^{\mu\nu} F_{\mu\nu} \quad (2.2.1.1)$$

In **Equation 2.2.1.1**, the first term is a kinetic term for the electron field, the second term describes the interaction between the electron field and the photon field and the last term is a kinetic term associated with the photon field. Now let's introduce a local gauge transformation for the electron field:

$$\psi(x) \rightarrow \psi'(x) = e^{iq\chi(x)} \psi(x) \quad (2.2.1.2)$$

In **Equation 2.2.1.2**, the term local refers to the fact that the arbitrary function  $\chi(x)$  is a function of space-time, and not just an dimensionless phase. In order for the Lagrangian **Equation 2.2.1.1** to remain invariant under the local gauge transformation, the photon field  $A_\mu$  must also transform as:

$$A_\mu \rightarrow A'_\mu = A_\mu - \partial_\mu \chi \quad (2.2.1.3)$$

Using **Equation 2.2.1.3**, and considering the fact that the third term of **Equation 2.2.1.1** is invariant under a local gauge transformations, it can be easily shown that the whole Lagrangian is local gauge invariant. Now, let's consider the special case where the field  $A_\mu$  becomes massive. Then, the new Lagrangian describing the interaction between the electron field and the photon field would be altered as:

$$\mathcal{L}_{QED} = \bar{\psi} (\gamma^\mu \partial_\mu - m_e) \psi + e \bar{\psi} \gamma^\mu \psi A_\mu - \frac{1}{4} F^{\mu\nu} F_{\mu\nu} + \frac{1}{2} m_\gamma^2 A_\mu A^\mu \quad (2.2.1.4)$$

The above Lagrangian is known as the **Proca Lagrangian**. Considering the local gauge transformation of **Equation 2.2.1.2**, the last term of **Equation 2.2.1.4** would

be transformed as:

$$\frac{1}{2}m_\gamma^2 A_\mu A^\mu \rightarrow \frac{1}{2}m_\gamma^2 (A_\mu - \partial_\mu \chi) (A^\mu - \partial^\mu \chi) \neq \frac{1}{2}m_\gamma^2 A_\mu A^\mu \quad (2.2.1.5)$$

From **Equation 2.2.1.5** it becomes clear that a massive photon would violate the local gauge invariance. Whilst no problem arises with QED and QCD, due to the massless mediators, it is experimentally very well established that  $W^\pm$  and  $Z$  bosons are massive. Thus, this would make SM a non-renormalisable theory, as it would not respect the need for gauge invariance. This problem is solved through the Higgs Mechanism. Gauge bosons are thought to be massless initially so as to respect the local gauge invariance, and by interacting with the Higgs field they acquire mass, while at the same time breaking the local gauge symmetry.

## 2.2.2 Spontaneous Symmetry Breaking

Now, let's consider a scalar field  $\phi$ , under the influence of a potential  $V(\phi)$ . The corresponding Lagrangian can be written as:

$$\begin{aligned} \mathcal{L} &= \frac{1}{2} (\partial_\mu \phi) (\partial^\mu \phi) - V(\phi) \\ &= \frac{1}{2} (\partial_\mu \phi) (\partial^\mu \phi) - \frac{1}{2} \mu^2 \phi^2 - \frac{1}{4} \lambda \phi^4 \end{aligned} \quad (2.2.2.1)$$

In **Equation 2.2.2.1**, the first term represents a kinetic term for the scalar particle, the second term can be thought of as the mass term and the third term is associated with the four point vertex interaction vertex.

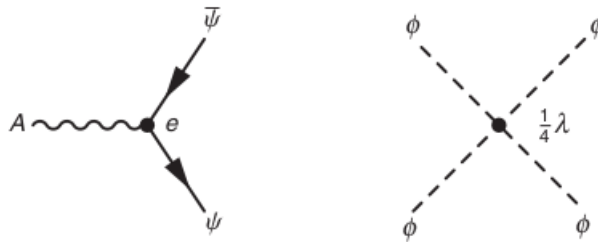


FIGURE 2.2.1: The three point interaction vertex in QED (left) and the four point interaction vertex for the scalar field  $\phi$  (right).

The vacuum state, which corresponds to the lowest energy state of the field  $\phi$ , corresponds to the minimum of the potential. In order for the potential to have a minimum,

$\lambda$  should be positive. Now, if  $\mu^2 > 0$ , then the potential has one minimum at  $\phi = 0$ , and the term associated with  $\mu^2$  can be thought of as the mass term for the field  $\phi$ . However, there is not restriction regarding  $\mu^2$ . Let's consider the case where  $\mu^2 < 0$  and let's try to calculate the vacuum state by minimizing the potential:

$$\begin{aligned} \frac{dV(\phi)}{d\phi} = 0 &\iff \\ \phi = \pm v &= \pm \left| \sqrt{\frac{-\mu^2}{\lambda}} \right| \end{aligned} \quad (2.2.2.2)$$

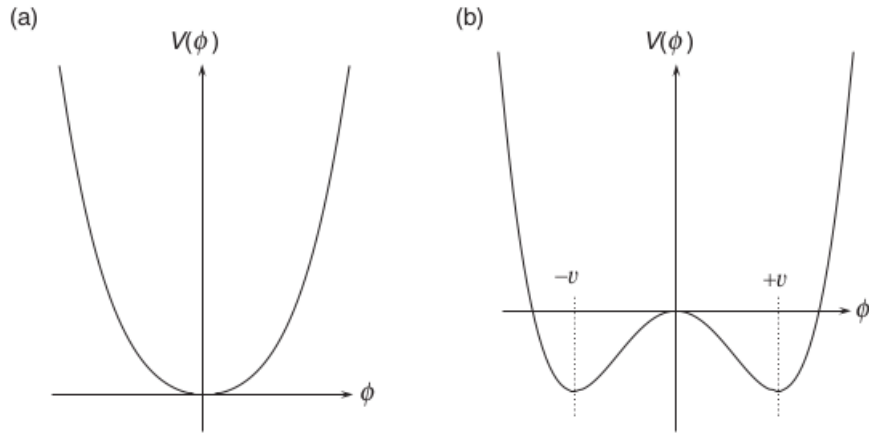


FIGURE 2.2.2: The potential  $V(\phi)$  for  $\lambda > 0$  and the cases  $\mu^2 > 0$  (a) and  $\mu^2 < 0$  (b).

Of course, the existence of two vacua is not allowed, so the value  $\phi = +v$  is chosen as the vacuum expectation value. This choice of vacuum state breaks the initial symmetry of the Lagrangian, a process known as **spontaneous symmetry breaking**.

In **Quantum Field Theory**, particles are perceived as excitations of the vacuum state. So, let's consider a perturbation around the vacuum state  $\phi(x) = v + \eta(x)$ . Since  $v$  is just a scalar, the Lagrangian for a perturbation around the vacuum state will be expressed as:

$$\begin{aligned} \mathcal{L} &= \frac{1}{2} (\partial_\mu \eta) (\partial^\mu \eta) - V(\eta) \\ &= \frac{1}{2} (\partial_\mu \eta) (\partial^\mu \eta) - \frac{1}{2} \mu^2 (\eta + v)^2 - \frac{1}{4} \lambda (\eta + v)^4 \end{aligned} \quad (2.2.2.3)$$

According to **Equation 2.2.2.2**, the minimum of the potential is given by  $\mu^2 = -\lambda v^2$  and so, **Equation 2.2.2.3** can be written as:

$$\mathcal{L} = \frac{1}{2} (\partial_\mu \eta) (\partial^\mu \eta) - \lambda v^2 \eta^2 - \lambda v \eta^3 - \frac{1}{4} \lambda \eta^4 + \frac{1}{4} \lambda v^4 \quad (2.2.2.4)$$

Since  $\mu^2 < 0$ , which means that the second term has opposite sign compared to the first kinetic term, the former can be interpreted as a mass term, by considering the comparison of **Equation 2.2.2.4** with the Lagrangian of a free scalar field:

$$\mathcal{L} = \frac{1}{2} (\partial_\mu \phi) (\partial^\mu \phi) - \frac{1}{2} m^2 \phi^2 \quad (2.2.2.5)$$

By comparing the two equations, it can be easily seen that:

$$m_\eta = \sqrt{2\lambda v^2} = \sqrt{-2\mu^2} \quad (2.2.2.6)$$

The most important conclusion that can be drawn from **Equation 2.2.2.4**, is that after the spontaneous symmetry breaking, the Lagrangian describes a massive field. The remaining terms can be thought of as a new potential  $V(\eta)$ . Terms proportional to  $\eta^3$  and  $\eta^4$  can be identified as the triple and quartic interaction terms, while the last term is just a constant with no physical meaning.

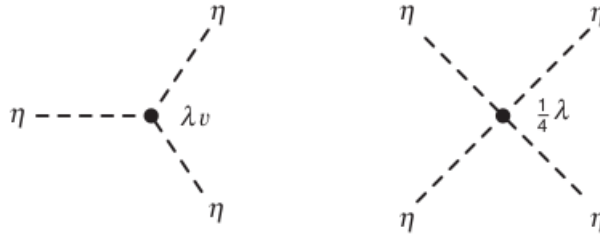


FIGURE 2.2.3: The triple and quartic vertices of the field  $\eta$ .

### 2.2.3 Complex Scalar Field

The same idea of the Spontaneous Symmetry Breaking can be introduced for a complex scalar field, where the field  $\phi$  can be expressed as:

$$\phi = \frac{1}{\sqrt{2}} (\phi_1 + i\phi_2) \quad (2.2.3.1)$$

Let's consider again the Lagrangian that describes this field:

$$\begin{aligned}
 \mathcal{L} &= \frac{1}{2} (\partial_\mu \phi)^* (\partial^\mu \phi) - V(\phi) \\
 &= \frac{1}{2} (\partial_\mu \phi)^* (\partial^\mu \phi) - \mu^2 (\phi^* \phi) - \lambda (\phi^* \phi)^2 \\
 &= \frac{1}{2} (\partial_\mu \phi_1)^* (\partial^\mu \phi_1) + \frac{1}{2} (\partial_\mu \phi_2)^* (\partial^\mu \phi_2) - \frac{1}{2} \mu^2 (\phi_1^2 + \phi_2^2) - \frac{1}{4} \lambda (\phi_1^2 + \phi_2^2)^2
 \end{aligned} \tag{2.2.3.2}$$

As stated above, in order for the potential to have a minimum,  $\lambda > 0$ . Again, if  $\mu^2 > 0$ , then the potential has one minimum at  $\phi_1 = \phi_2 = 0$ , and the term associated with  $\mu^2$  can be thought of as the mass term for the field  $\phi$ . Of course, there is possibility of  $\mu^2 < 0$ , where after minimizing the potential, it is obtained that:

$$\phi_1^2 + \phi_2^2 = \frac{-\mu^2}{\lambda} = v^2 \tag{2.2.3.3}$$

From **Equation** 2.2.3.3, it can be seen that the vacuum state belongs to a circle formed by the contour of the potential plot, which breaks the initial symmetry of the Lagrangian.

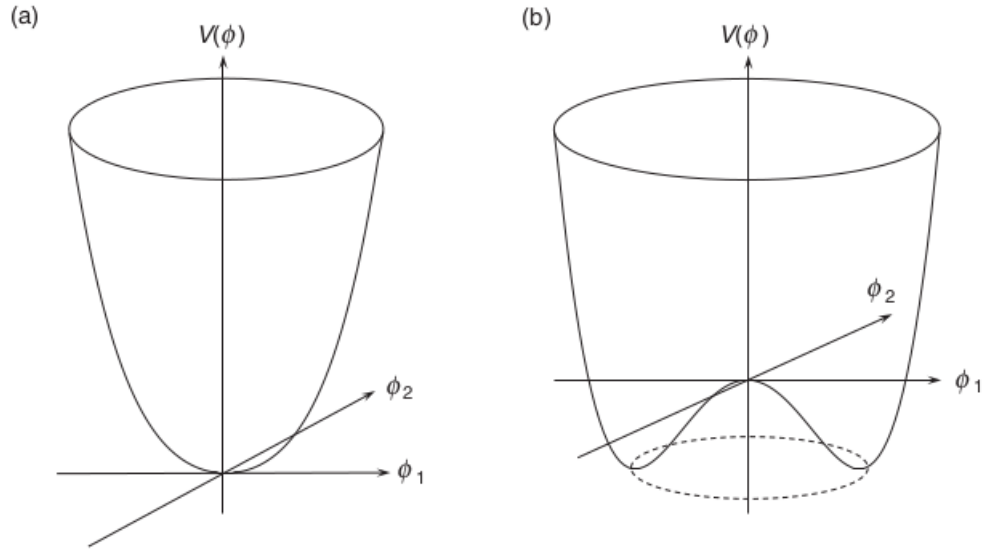


FIGURE 2.2.4: The potential  $V(\phi)$  for  $\lambda > 0$  and the cases  $\mu^2 > 0$  (a) and  $\mu^2 < 0$  (b).

The vacuum state is chosen to be in the real direction,  $(\phi_1, \phi_2) = (v, 0)$ . Now let's consider a perturbation around this vacuum state  $\phi_1 = v + \eta(x)$  and  $\phi_2 = \xi(x)$ . The



perturbed field will be expressed as:

$$\phi = \frac{1}{\sqrt{2}} (v + \eta + i\xi) \quad (2.2.3.4)$$

Of course, the expression of the potential will be have to altered and expressed in terms of the perturbations. Also using  $\mu^2 = -\lambda v^2$ , it can be derived that:

$$\begin{aligned} V(\phi) &= \mu^2 (\phi^* \phi) + \lambda (\phi^* \phi)^2 \\ &= -\frac{1}{2} \lambda v^2 \{(v + \eta)^2 + \xi^2\} + \frac{1}{4} \lambda \{(v + \eta)^2 + \xi^2\}^2 \\ &= -\frac{1}{2} \lambda v^4 + \lambda v^2 \eta^2 + \lambda v \eta^3 + \frac{1}{2} \lambda \eta^4 + \frac{1}{2} \lambda \xi^4 + \lambda v \eta \xi^2 + \frac{1}{2} \lambda \eta^2 \xi^2 \end{aligned} \quad (2.2.3.5)$$

The full expression of the Lagrangian will be:

$$\mathcal{L} = \frac{1}{2} (\partial_\mu \eta) (\partial^\mu \eta) - \lambda v^2 \eta^2 + \frac{1}{2} (\partial_\mu \xi) (\partial^\mu \xi) - V_{int}(\eta, \xi) \quad (2.2.3.6)$$

Since  $\mu^2 < 0$ , the second term in **Equation** 2.2.3.6, can be identified as the mass term for the field  $\eta(x)$ . Comparing this equation, with **Equation** 2.2.2.5, it can be easily seen that:

$$m_\eta = \sqrt{2\lambda v^2} = \sqrt{-2\mu^2} \quad (2.2.3.7)$$

The remaining term  $V_{int}(\eta, \xi)$  is the following:

$$V_{int}(\eta, \xi) = \lambda v \eta^3 + \frac{1}{2} \lambda \eta^4 + \frac{1}{2} \lambda \xi^4 + \lambda v \eta \xi^2 + \frac{1}{2} \lambda \eta^2 \xi^2 \quad (2.2.3.8)$$

The term  $-\frac{1}{2} \lambda v^4$  is just a constant, with no physical meaning. The term in **Equation** 2.2.3.8 describes triple and quartic interactions of the fields  $\eta$  and  $\xi$ .

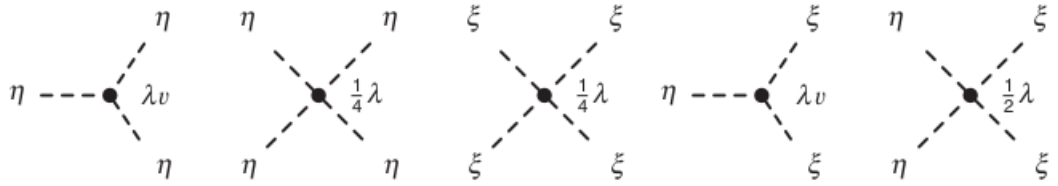


FIGURE 2.2.5: The triple and quartic vertices of the fields  $\eta$  and  $\xi$ .

An important remark arising from **Equation** 2.2.3.6 is that the field  $\xi$  remains massless. This massless field is known as the Goldstone boson. Its masslessness is a consequence of the direction of the symmetry breaking. The initial symmetry of the Lagrangian was

broken in the real direction with the choice of the vacuum state, and thus, only the field  $\eta$  acquires mass. This concept can be better understood via the **Figure 2.2.6**:

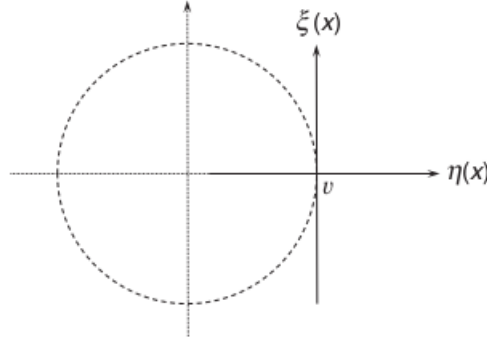


FIGURE 2.2.6: Field  $\eta(x)$  and  $\xi(x)$  with respect to the vacuum state.

#### 2.2.4 The Higgs Mechanism under a $U(1)$ local gauge symmetry

So far, the concept of the spontaneous symmetry breaking was introduced only for the case of a **global** gauge symmetry. Now, let's introduce an example of a  $U(1)$  **local** gauge symmetry:

$$\psi(x) \rightarrow \psi'(x) = e^{ig\chi(x)}\psi(x) \quad (2.2.4.1)$$

Let's also consider a complex field  $\phi$ , under the influence of a potential:

$$V(\phi) = \mu^2\phi^2 + \lambda\phi^4 \quad (2.2.4.2)$$

The Lagrangian of the complex field  $\phi$  is not invariant under the new local gauge transformation. In order for the Lagrangian to remain unaffected by the local gauge transformation, a new gauge field must be introduced. The new field will alter the expression of the covariant derivatives as:

$$\partial_\mu \rightarrow D_\mu = \partial_\mu + igB_\mu \quad (2.2.4.3)$$

Also, in order for the Lagrangian to be local gauge invariant, the new gauge field appearing in **Equation 2.2.4.3** must transform as:

$$B_\mu \rightarrow B'_\mu = B_\mu - \partial_\mu\chi(x) \quad (2.2.4.4)$$

As it is obvious, the invariance of the Lagrangian under a local gauge transformation requires the existence of a new gauge field, that has very specific transformation properties. The total Lagrangian, that will take into account both the complex field  $\phi$  and the new gauge field, will be expressed as:

$$\mathcal{L} = -\frac{1}{4}F_{\mu\nu}F^{\mu\nu} + (D_\mu\phi)^*(D^\mu\phi) - \mu^2\phi^2 - \lambda\phi^4 \quad (2.2.4.5)$$

The first term of **Equation 2.2.4.5** is a kinetic term for the new gauge field, and is given by:

$$F^{\mu\nu} = \partial^\mu B^\nu - \partial^\nu B^\mu \quad (2.2.4.6)$$

Of course, the new gauge field must be massless in order to preserve the local gauge invariance. The term that involves the covariant derivatives can be simplified, and written as:

$$\begin{aligned} (D_\mu\phi)^*(D^\mu\phi) &= (\partial_\mu - igB_\mu)\phi^*(\partial^\mu - igB^\mu)\phi \\ &= (\partial_\mu\phi)^*(\partial^\mu\phi) - igB_\mu\phi^*(\partial^\mu\phi) + ig(\partial_\mu\phi)^*B^\mu\phi + g^2B_\mu B^\mu\phi\phi^* \end{aligned} \quad (2.2.4.7)$$

Substituting **Equation 2.2.4.7** in **Equation 2.2.4.5**, the Lagrangian will be expressed as:

$$\begin{aligned} \mathcal{L} &= -\frac{1}{4}F_{\mu\nu}F^{\mu\nu} + (\partial_\mu\phi)^*(\partial^\mu\phi) - \mu^2\phi^2 - \lambda\phi^4 \\ &\quad - igB_\mu\phi^*(\partial^\mu\phi) + ig(\partial_\mu\phi)^*B^\mu\phi + g^2B_\mu B^\mu\phi\phi^* \end{aligned} \quad (2.2.4.8)$$

For the case of  $\mu^2 < 0$ , the vacuum state breaks the initial symmetry of the Lagrangian. By choosing the vacuum state to be  $\phi_1^2 + \phi_2^2 = \frac{-\mu^2}{\lambda} = v^2$ , and perturbing the field  $\phi$  around the vacuum state, it can be written that:

$$\phi = \frac{1}{\sqrt{2}}(v + \eta(x) + i\xi(x)) \quad (2.2.4.9)$$

Substituting **Equation 2.2.4.9** in **Equation 2.2.4.8**, it can be shown that the Lagrangian will be expressed as:

$$\mathcal{L} = \underbrace{\frac{1}{2}(\partial_\mu\eta)(\partial^\mu\eta) - \lambda v^2\eta^2}_{\text{massive } \eta} + \underbrace{\frac{1}{2}(\partial_\mu\xi)(\partial^\mu\xi)}_{\text{massless } \xi} - \underbrace{\frac{1}{4}F_{\mu\nu}F^{\mu\nu} + \frac{1}{2}g^2vB_\mu B^\mu}_{\text{massive gauge field}} - V_{int} + gvB_\mu(\partial^\mu\xi) \quad (2.2.4.10)$$

As can be seen from **Equation 2.2.4.5**, the spontaneous symmetry breaking of the initial Lagrangian produces a massive scalar field  $\eta$  and a massless Goldstone boson  $\xi$ . Moreover, the initially massless gauge field  $B_\mu$ , has now acquired mass via the mass term  $\frac{1}{2}g^2vB_\mu B^\mu$ .

However, the massiveness of the gauge field gives rise to a problem. The initial Lagrangian was characterized by four degrees of freedom. Two came from the scalar fields  $\phi_1$  and  $\phi_2$ , and the other two came from the two transverse polarization states of the massless field  $B_\mu$ . Now that the field  $B_\mu$  has become massive, its polarization states have become three, two transverse plus one longitudinal, giving a total of five degrees of freedom in the final Lagrangian. It seems that in some way, during the spontaneous symmetry breaking, a new degree of freedom has appeared. This issue can be treated via the elimination of the Goldstone boson from **Equation 2.2.4.10**. It can be noticed that:

$$\frac{1}{2}(\partial_\mu \xi)(\partial^\mu \xi) + gvB_\mu(\partial^\mu \xi) + \frac{1}{2}g^2v^2B_\mu B^\mu = \frac{1}{2}g^2v^2 \left[ B_\mu + \frac{1}{gv}(\partial_\mu \xi) \right]^2 \quad (2.2.4.11)$$

According to **Equation 2.2.4.11**, we can make the following gauge transformation:

$$B_\mu \rightarrow B'_\mu = B_\mu + \frac{1}{gv}(\partial_\mu \xi) \quad (2.2.4.12)$$

Using to **Equation 2.2.4.12**, **Equation 2.2.4.10** can be written as:

$$\mathcal{L} = \underbrace{\frac{1}{2}(\partial_\mu \eta)(\partial^\mu \eta) - \lambda v^2 \eta^2}_{\text{massive } \eta} - \underbrace{\frac{1}{4}F_{\mu\nu}F^{\mu\nu} + \frac{1}{2}g^2vB'_\mu B'^\mu}_{\text{massive gauge field}} - V_{int} \quad (2.2.4.13)$$

As it is obvious from **Equation 2.2.4.13**, with the correct choice of gauge, the Goldstone boson vanishes from the Lagrangian. By comparing **Equation 2.2.4.4** and **Equation 2.2.4.12**, it is derived that  $\chi(x) = -\xi(x)/gv$ . So, the corresponding gauge transformation for  $\phi$  will be:

$$\phi(x) \rightarrow \phi'(x) = e^{-ig\frac{\xi(x)}{gv}}\phi(x) = e^{-i\frac{\xi(x)}{v}}\phi(x) \quad (2.2.4.14)$$

**Equation 2.2.4.9**, in terms of first order of the fields, can be rewritten as:

$$\phi(x) \approx \frac{1}{\sqrt{2}}(v + \eta(x))e^{i\frac{\xi(x)}{v}} \quad (2.2.4.15)$$

Consequently, the effect of the gauge transformation on the perturbation around the vacuum state will be:

$$\phi(x) \rightarrow \phi'(x) = \frac{1}{\sqrt{2}} e^{-i\frac{\xi(x)}{v}} (v + \eta(x)) e^{i\frac{\xi(x)}{v}} = \frac{1}{\sqrt{2}} (v + \eta(x)) \quad (2.2.4.16)$$

From **Equation 2.2.4.16** it can be seen that in the gauge in which the Goldstone boson is eliminated from the Lagrangian, also known as the *Unitary Gauge*, the perturbation around the vacuum state of the  $\phi$  is chosen to be entirely real:

$$\phi(x) = \frac{1}{\sqrt{2}} (v + \eta(x)) = \frac{1}{\sqrt{2}} (v + h(x)) \quad (2.2.4.17)$$

The field  $\eta(x)$  has been replaced by the Higgs field  $h(x)$  so as to emphasize that this is the physical field. Following the same procedure as before, and replacing  $\mu^2 = -\lambda v^2$ , the Lagrangian of **Equation 2.2.4.5**, can be expressed as:

$$\begin{aligned} \mathcal{L} &= (D_\mu \phi)^* (D^\mu \phi) - \frac{1}{4} F_{\mu\nu} F^{\mu\nu} - \mu^2 \phi^2 - \lambda \phi^4 \\ &= \frac{1}{2} (\partial_\mu - ig B_\mu) (v + h) (\partial^\mu + ig B^\mu) (v + h) - \frac{1}{4} F_{\mu\nu} F^{\mu\nu} - \frac{1}{2} \mu^2 (v + h)^2 - \frac{1}{4} \lambda (v + h)^4 \\ &= \frac{1}{2} (\partial_\mu h) (\partial^\mu h) + \frac{1}{2} g^2 B_\mu B^\mu (v + h)^2 - \frac{1}{4} F_{\mu\nu} F^{\mu\nu} - \lambda v^2 h^2 - \lambda v h^3 - \frac{1}{4} \lambda h^4 + \frac{1}{4} \lambda v^4 \end{aligned} \quad (2.2.4.18)$$

Gathering up all the terms and ignoring the final term, which is a constant with no physical meaning, **Equation 2.2.4.18** can be written as:

$$\begin{aligned} \mathcal{L} &= \underbrace{\frac{1}{2} (\partial_\mu h) (\partial^\mu h) - \lambda v^2 h^2}_{\text{massive } h \text{ scalar}} - \underbrace{\frac{1}{4} F_{\mu\nu} F^{\mu\nu} + \frac{1}{2} g^2 v^2 B_\mu B^\mu}_{\text{massive gauge boson}} \\ &\quad + \underbrace{g^2 v B_\mu B^\mu h + \frac{1}{2} g^2 B_\mu B^\mu h^2}_{h, B \text{ interactions}} - \underbrace{\lambda v h^3 - \frac{1}{4} \lambda h^4}_{h \text{ self-interactions}} \end{aligned} \quad (2.2.4.19)$$

The Lagrangian of **Equation 2.2.4.19** describes a massive scalar Higgs, a massive gauge boson, the interactions between the two and the self-interactions of the Higgs boson. From the mass term associated with the massive gauge boson, it can be derived that:

$$m_B = gv \quad (2.2.4.20)$$

Whereas, for the Higgs boson itself:

$$m_H = \sqrt{2\lambda} v \quad (2.2.4.21)$$

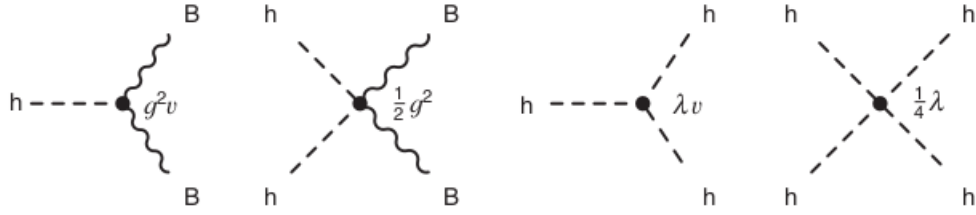


FIGURE 2.2.7: The interactions of the Higgs boson under a  $U(1)$  local gauge symmetry.

### 2.2.5 The Standard Model Higgs

In the above subsection, the Higgs mechanism was considered under a  $U(1)$  local gauge symmetry. Of course, it is widely known that the Higgs mechanism breaks the electroweak symmetry, which is a  $SU(2)_L \times U(1)_Y$  local gauge symmetry. In order to describe the fields, an electroweak isospin doublet is needed, where the upper and the lower component will differ by one unit of electric charge.

The Higgs mechanism under the electroweak local gauge symmetry is required to generate the masses of the electroweak gauge boson. Thus, one of the fields in the doublet will be neutral, denoted as  $\phi^0$ , and the other field, which is required to have electric charge, will be denoted as  $\phi^+$ , where  $(\phi^+)^* = \phi^-$ . Consequently, the isospin doublet, will be expressed with the help of two complex fields:

$$\phi = \begin{pmatrix} \phi^+ \\ \phi^0 \end{pmatrix} = \frac{1}{\sqrt{2}} \begin{pmatrix} \phi_1 + i\phi_2 \\ \phi_3 + i\phi_4 \end{pmatrix} \quad (2.2.5.1)$$

The Lagrangian describing the field in **Equation 2.2.5.1** will be:

$$\mathcal{L} = (\partial_\mu \phi)^\dagger (\partial^\mu \phi) - V(\phi) \quad (2.2.5.2)$$

Where:

$$V(\phi) = \mu^2 \phi^\dagger \phi + \lambda (\phi^\dagger \phi)^2 \quad (2.2.5.3)$$

For  $\mu^2 < 0$ , the minima of the potential satisfy:

$$\phi^\dagger \phi = \phi_1^2 + \phi_2^2 + \phi_3^2 + \phi_4^2 = \frac{v^2}{2} = \frac{-\mu^2}{2\lambda} \quad (2.2.5.4)$$

Therefore, the vacuum state will be expressed as:

$$\langle 0|\phi|0\rangle = \frac{1}{\sqrt{2}} \begin{pmatrix} 0 \\ v \end{pmatrix} \quad (2.2.5.5)$$

Then, the field can be perturbed around the vacuum state in order to induce the spontaneous symmetry breaking. The field perturbation will be expressed as:

$$\phi(x) = \frac{1}{\sqrt{2}} \begin{pmatrix} \phi_1(x) + i\phi_2(x) \\ v + \eta(x) + i\phi_4(x) \end{pmatrix} \quad (2.2.5.6)$$

After the spontaneous symmetry breaking, one massive scalar and three massless Goldstone bosons will arise. Instead of repeating the same procedure and absorbing the Goldstone bosons as a local gauge transformation, the Higgs double is immediately expressed in the *Unitary gauge*, as:

$$\phi(x) = \frac{1}{\sqrt{2}} \begin{pmatrix} 0 \\ v + h(x) \end{pmatrix} \quad (2.2.5.7)$$

The derivatives appearing in **Equation 2.2.5.2** must be changed accordingly, in order to respect the  $SU(2)_L \times U(1)_Y$  local gauge symmetry. Therefore:

$$\partial_\mu \rightarrow D_\mu = \partial_\mu + ig_w \mathbf{T} \cdot \mathbf{W}_\mu + ig' \frac{Y}{2} B_\mu \quad (2.2.5.8)$$

In **Equation 2.2.5.8**,  $\mathbf{T} = \frac{1}{2}\boldsymbol{\sigma}$ , corresponding to the one half of the Pauli matrices, which are the generators of the  $SU(2)$  symmetry. Also,  $Y$  corresponds to the weak hypercharge, which is given from  $Y = 2(Q - I_W^{(3)})$ , where  $Q$  and  $I_W^{(3)}$  correspond to the electric charge and the third component of the weak isospin respectively.

The lower component of the doublet is electrically neutral and has  $I_W^{(3)} = -\frac{1}{2}$ , and resulting in  $Y = 1$ . Hence, the effect of the covariant derivative on  $\phi$  can be expressed as:

$$D_\mu \phi = \frac{1}{2} [2\partial_\mu + ig_w \boldsymbol{\sigma} \cdot \mathbf{W}_\mu + ig' B_\mu] \phi \quad (2.2.5.9)$$

From **Equation 2.2.5.9** it can be seen that  $D_\mu$  is described by a  $2 \times 2$  matrix, which will act on the perturbed field. By doing the calculations:

$$\begin{aligned} D_\mu \phi &= \frac{1}{2\sqrt{2}} \begin{pmatrix} 2\partial_\mu + ig_w W_\mu^{(3)} + ig' B_\mu & ig_w [W_\mu^{(1)} - iW_\mu^{(2)}] \\ ig_w [W_\mu^{(1)} + iW_\mu^{(2)}] & 2\partial_\mu - ig_w W_\mu^{(3)} + ig' B_\mu \end{pmatrix} \begin{pmatrix} 0 \\ v + h \end{pmatrix} \\ &= \frac{1}{2\sqrt{2}} \begin{pmatrix} ig_w [W_\mu^{(1)} - iW_\mu^{(2)}] (v + h) \\ (2\partial_\mu - ig_w W_\mu^{(3)} + ig' B_\mu) (v + h) \end{pmatrix} \end{aligned} \quad (2.2.5.10)$$

By multiplying **Equation 2.2.5.10** with its Hermitian conjugate, what is obtained is:

$$\begin{aligned} (D_\mu \phi)^\dagger D_\mu \phi &= \frac{1}{2} (\partial_\mu h) (\partial^\mu h) + \frac{1}{8} g_w^2 (W_\mu^{(1)} + iW_\mu^{(2)}) (W_\mu^{(1)} - iW_\mu^{(2)}) (v + h)^2 \\ &\quad + \frac{1}{8} (g_w W_\mu^{(3)} - g' B_\mu) (g_w W^{(3)\mu} - g' B^\mu) (v + h)^2 \end{aligned} \quad (2.2.5.11)$$

After doing some algebra and using some identities, some terms appear in the Lagrangian:

$$\frac{1}{8} g_w^2 v^2 (W_\mu^{(1)} W^{(1)\mu} + W_\mu^{(2)} W^{(2)\mu}) \quad (2.2.5.12)$$

These terms in **Equation 2.2.5.12** can be identified as mass terms of the fields  $W_\mu^{(1)}$  and  $W_\mu^{(2)}$ . Comparing these equations with **Equation 2.2.2.5**, it is derived that the mass of the W boson is:

$$m_W = \frac{1}{2} g_w v \quad (2.2.5.13)$$

Also, inside the Lagrangian appear terms that are associated with the  $W_\mu^{(3)}$  and  $B_\mu$  fields. These terms can be written as:

$$\begin{aligned} \frac{v^2}{8} (g_w W_\mu^{(3)} - g' B_\mu) (g_w W^{(3)\mu} - g' B^\mu) &= \frac{v^2}{8} \begin{pmatrix} W_\mu^{(3)} & B_\mu \end{pmatrix} \begin{pmatrix} g_w^2 & -g_w g' \\ -g_w g' & g'^2 \end{pmatrix} \begin{pmatrix} W_\mu^{(3)} \\ B_\mu \end{pmatrix} \\ &= \frac{v^2}{8} \begin{pmatrix} W_\mu^{(3)} & B_\mu \end{pmatrix} \mathbf{M} \begin{pmatrix} W_\mu^{(3)} \\ B_\mu \end{pmatrix} \end{aligned} \quad (2.2.5.14)$$

In **Equation 2.2.5.14**,  $\mathbf{M}$  corresponds to a non-diagonal mass matrix. The fields  $W_\mu^{(3)}$  and  $B_\mu$  do not correspond to the physical fields. In order to produce the physical fields, we must choose a basis in which  $\mathbf{M}$  will be diagonal. The eigenvectors of this diagonal matrix will correspond to the physical fields themselves, whereas the diagonal



elements, which will be the eigenvalues of the matrix, will correspond to the masses of the physical fields. In order to diagonalize  $\mathbf{M}$ , the characteristic equation must be used:

$$\begin{aligned}\mathbf{M} - \lambda I &= 0 \Leftrightarrow \\ (g_w^2 - \lambda)(g'^2 - \lambda) &= 0\end{aligned}\tag{2.2.5.15}$$

By solving **Equation 2.2.5.15**, it is obtained that:

$$\lambda = 0 \quad \text{or} \quad \lambda = g_w^2 + g'^2\tag{2.2.5.16}$$

Hence, in the diagonal basis **Equation 2.2.5.14** can be written as:

$$\frac{v^2}{8} \begin{pmatrix} A_\mu & Z_\mu \end{pmatrix} \begin{pmatrix} 0 & 0 \\ 0 & g_w^2 + g'^2 \end{pmatrix} \begin{pmatrix} A_\mu \\ Z_\mu \end{pmatrix}\tag{2.2.5.17}$$

In order for **Equation 2.2.5.17** to resemble a mass term in the Lagrangian, it must be written as:

$$\frac{1}{2} \begin{pmatrix} A_\mu & Z_\mu \end{pmatrix} \begin{pmatrix} m_A^2 & 0 \\ 0 & m_Z^2 \end{pmatrix} \begin{pmatrix} A_\mu \\ Z_\mu \end{pmatrix}\tag{2.2.5.18}$$

Comparing **Equation 2.2.5.18** with **Equation 2.2.2.5**, it is derived that:

$$m_A = 0 \quad \text{and} \quad m_Z = \frac{1}{2}v\sqrt{g_w^2 + g'^2}\tag{2.2.5.19}$$

From **Equation 2.2.5.19**, it can be noticed that one massless and one massive field appears, which can be identified as the photon and the Z boson respectively. The physical fields, can be expressed in terms of the fields  $W_\mu^{(3)}$  and  $B_\mu$ :

$$A_\mu = \frac{g'W_\mu^{(3)} + g_w B_\mu}{\sqrt{g_w^2 + g'^2}}\tag{2.2.5.20}$$

$$Z_\mu = \frac{g_w W_\mu^{(3)} - g' B_\mu}{\sqrt{g_w^2 + g'^2}}\tag{2.2.5.21}$$

By defining:

$$\frac{g'}{g_w} = \tan \theta_w\tag{2.2.5.22}$$

And by substituting in **Equation 2.2.5.20** and **Equation 2.2.5.21**, and by doing some algebra, it can be derived that:

$$\begin{aligned} A_\mu &= \cos \theta_w W_\mu^{(3)} + \sin \theta_w B_\mu \\ Z_\mu &= -\sin \theta_w W_\mu^{(3)} + \cos \theta_w B_\mu \end{aligned} \quad (2.2.5.23)$$

**Equation 2.2.5.23** describes the mixing between the physical fields and the fields arising in order for the Lagrangian to respect the  $SU(2)_L \times U(1)_Y$  local gauge symmetry. This mixing is put by hand in the electroweak theory, whereas, in the Higgs mechanism, it is predicted directly. Furthermore, using **Equation 2.2.5.22**, the mass of the Z boson can be expressed as:

$$m_Z = \frac{1}{2} \frac{g_w}{\cos \theta_w} v \quad (2.2.5.24)$$

Therefore, combining the expression found for the mass of the Z boson and the expression found for the mass of the W boson, it can be derived that:

$$\frac{m_W}{m_Z} = \cos \theta_w \quad (2.2.5.25)$$

Having measured the parameters  $g_w$  and  $m_W$  experimentally, using **Equation 2.2.5.13**, the vacuum expectation value can be calculated:

$$v = 246 \text{ GeV} \quad (2.2.5.26)$$

Of course, by measuring the mass of the Higgs boson experimentally, and using **Equation 2.2.4.21** and **Equation 2.2.5.26**, the parameter  $\lambda$  can be calculated.

In **Equation 2.2.5.11**, the right hand side contains terms in the form of  $VV(v+h)^2$ . Beside giving mass to the gauge boson, these terms are also useful in order to calculate the coupling between the physical fields and the Higgs field. The physical W boson field is a mixing between the fields  $W_\mu^{(1)}$  and  $W_\mu^{(2)}$ :

$$W^\pm = \frac{1}{\sqrt{2}} (W^{(1)} \mp W^{(2)}) \quad (2.2.5.27)$$

Therefore, the right hand side of **Equation 2.2.5.11** can be written:

$$\frac{1}{4} g_w^2 W_\mu^- W^{+\mu} (v+h)^2 = \frac{1}{4} g_w^2 v^2 W_\mu^- W^{+\mu} + \frac{1}{2} g_w^2 v W_\mu^- W^{+\mu} h + \frac{1}{4} g_w^2 W_\mu^- W^{+\mu} h h \quad (2.2.5.28)$$

The first term in **Equation** 2.2.5.28 gives mass to the  $W^+$  and  $W^-$  bosons. The second terms gives the coupling of the  $W^+W^-h$  vertex:

$$g_{HWW} = \frac{1}{2}g_w^2 v = g_w m_W \quad (2.2.5.29)$$

In the same manner, it can be shown that the coupling of the vertex  $ZZh$  is:

$$g_{HZZ} = g_Z m_Z \quad (2.2.5.30)$$

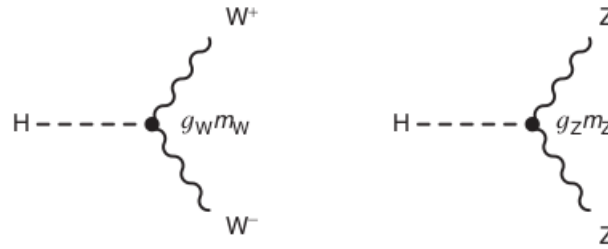


FIGURE 2.2.8: The  $W^+W^-H$  and  $ZZH$  vertices, with their couplings.

## 2.3 Beyond Standard Model Theories

After the latest LHC triumph of discovering the Higgs boson, the periodic table of particle physics seems to be complete. There is no other particle predicted by the SM, which has not been discovered. In principle, we can describe the world around us based on our knowledge for quarks, leptons and their fundamental interactions, which are all described by SM.

However, we are fully aware that SM is not a complete theory. For example, SM predicts stable and massless neutrinos, whilst many great experiments have proved that neutrinos change their flavour while travelling. This phenomenon is known as neutrino oscillations. Neutrino oscillations dictate that neutrinos are not massless. On the contrary, they must have a very small mass. Also, SM does not incorporate gravity and fails in giving explanations to questions such as to what is dark matter or what is dark energy.

In order to explain the deficiencies of the SM, we could assume that the SM is a low energy limit of a more fundamental higher energy theory. Several theoretical models have been proposed for this purpose. In this thesis, the **Heavy Vector Triplet** model

is going to be briefly presented, and experimentally tested using data for the ATLAS detector.

### 2.3.1 Heavy Vector Triplet Model

Before developing the idea of the Heavy Vector Triplet (HVT) model it is necessary to introduce the general strategy behind it, which is the **Simplified Model** approach developed below.

In order to explore the possible existence of New Physics which consists of the production of narrow new particles, we should keep in mind that these resonance searches are only sensitive to parameters that are correlated to the mass of the resonance and to interactions involved in its production and decay. As a result, we can establish a **phenomenological Lagrangian** in order to describe the new resonance, including only mass parameters and relevant couplings. It should also be noted that the **Simplified Model** is not a complete theory, so it should only be used in its region of validity which is the on-shell resonance production and decay.

In the context of a simplified Lagrangian, the case of electroweak-charged spin-1 heavy resonances are considered, called Heavy Vector Triplets. Beside the known SM fields, the HVT model inserts three new fields  $V_\mu^\alpha$ , where  $\alpha = 1, 2, 3$ , in the adjoint representation of  $SU(2)_L$ . The new fields  $V_\mu^\alpha$  represent the electroweak eigenstates. The mass eigenstates, which are two charged fields and one neutral field, are obtained from the below linear combinations:

$$V_\mu^\pm = \frac{V_\mu^1 \mp iV_\mu^2}{\sqrt{2}}, \quad V_\mu^0 = V_\mu^3 \quad (2.3.1.1)$$

As described in [16], the phenomenological Lagrangian describing the interactions of the new bosons is the following:

$$\begin{aligned} \mathcal{L}_V = & -\frac{1}{4}D_{[\mu}V_{\nu]}^\alpha D^{[\mu}V^{\nu]\alpha} + \frac{m_V^2}{2}V_\mu^\alpha V^{\mu\alpha} \\ & + ig_V c_H V_\mu^\alpha H^\dagger \tau^\alpha \overleftrightarrow{D}^\mu H + \frac{g^2}{g_V^2} c_F V_\mu^\alpha J_F^{\mu\alpha} \\ & + \frac{g_V}{2} c_{VVV} \epsilon_{abc} V_\mu^\alpha V_\nu^b D^{[\mu}V^{\nu]c} + g_V^2 c_{VVHH} V_\mu^\alpha V^{\mu\alpha} H^\dagger H - \frac{g}{2} c_{VW} \epsilon_{abc} W^{\mu\nu\alpha} V_\mu^b V_\nu^c \end{aligned} \quad (2.3.1.2)$$

In **Equation 2.3.1.2**,  $g$  stands for the  $SU(2)_L$  coupling constant and  $\tau^\alpha = \sigma^\alpha/2$  are the Pauli matrices. The first line of **Equation 2.3.1.2** describes the kinetic and the mass term of the new vector boson  $V$ .

The second line includes the direct interactions between  $V$  and the Higgs field, as well as the interactions between  $V$  and the SM left-handed fermionic currents:

$$J_F^{\mu\alpha} = \sum_f \bar{f} \gamma^\mu \tau^\alpha f_L \quad (2.3.1.3)$$

The parameter  $c_H$  controls the interactions of the boson  $V$  with the physical Higgs field, and with the SM  $W$  and  $Z$  bosons. The parameter  $c_F$  describes the direct interaction of  $V$  with fermions, responsible for both its fermionic decays and its production via quark-antiquark fusion (Drell-Yan) process. The form presented here is a generalization for different couplings to leptons, light quarks and third generation quarks, taking into account the corresponding currents:

$$c_F V \cdot J_F \rightarrow c_l V \cdot J_l + c_q V \cdot J_q + c_3 V \cdot J_3 \quad (2.3.1.4)$$

The parameter  $c_F$  is of order one and  $c_H$  is of order one in the strongly coupled scenario, but can be lower in the weakly coupled scenario.

The third line introduces the parameters  $c_{VVV}$ ,  $c_{VVHH}$  and  $c_{V VW}$ . However, these parameters are disregarded because they do not contain vertices of one  $V$  and light SM fields or single production processes, and therefore are irrelevant with LHC searches.

Finally, the last parameter introduced is  $g_V$ , which stands for the typical strength of the  $V$  boson interactions. The parameter  $g_V$  can vary over one order of magnitude from a weakly-coupled scenario with  $g_V \approx 1$  up to the extreme strong limit where  $g_V \approx 4\pi$ .

Assuming that we call  $W'$  the electrically charged heavy resonance and  $Z'$  the neutral heavy resonance, with masses  $M_\pm$  and  $M_0$  respectively, a generalized custodial relation among physical masses is obtained:

$$M_{W'}^2 M_\pm^2 = \cos \theta_w M_{Z'}^2 M_0^2 \quad (2.3.1.5)$$

The goal of this model is to describe new vectors at or above the TeV scale, while being able to reproduce the SM masses  $M_{W,Z} \approx 100$  GeV. This is possible via applying

a hierarchy in the mass spectrum :

$$\frac{M_{W,Z}}{M_{\pm,0}} \lesssim 10^{-1} \ll 1 \quad (2.3.1.6)$$

The decay modes of  $V$  are di-lepton, di-quark and di-boson. All the coupling to fermions are controlled by the parameter  $g^2/c_F g_V$ . The partial width to fermions is given by:

$$\Gamma_{V_{\pm} \rightarrow f \bar{f}'} \approx 2\Gamma_{V_0 \rightarrow f \bar{f}} \approx N_c[f] \left( \frac{g^2 c_F}{g_V} \right)^2 \frac{M_V}{48\pi} \quad (2.3.1.7)$$

In **Equation** 2.3.1.7,  $N_c[f]$  stands for the number of colors, and is equal to 3 for di-quark productions and equal to 1 for di-lepton productions. For the di-boson case, the Equivalence theorem is considered [3]. The Equivalence theorem states that in the high energy regime, the longitudinal polarization of the vector boson will dominate. Thus, the coupling to the Higgs boson  $c_H$  will be the same as as to the SM  $W$  and  $Z$  bosons. Hence, the partial width will be given from:

$$\Gamma_{V_0 \rightarrow W_L^+ W_L^-} \approx \Gamma_{V_{\pm} \rightarrow W_L^{\pm} Z_L} \approx \frac{g_V^2 c_H^2 M_V}{192\pi} \quad (2.3.1.8)$$

The production cross section is found to be proportional to the partial width  $\Gamma_{V \rightarrow ij}$ :

$$\sigma(pp \rightarrow V + X) \propto \sum_{i,j} \frac{\Gamma_{V \rightarrow ij}}{M_V} \quad (2.3.1.9)$$

In **Equation** 2.3.1.9,  $i, j = q, \bar{q}, W, Z$  denote the resulting particles of the  $V$  boson decay.

There are three explicit models associated with the HVT model. In this thesis, only **Model A** is studied, for which the couplings are of order:

$$c_H \sim -g^2/g_V^2, \quad c_F \sim 1 \quad (2.3.1.10)$$

Also, this thesis only considers the Drell-Yan production of a  $W'$  boson. In **Figure** 2.3.1, the quark-antiquark fusion Feynman diagram is illustrated, which leads to the production a  $W^{\pm'}$ . The  $W^{\pm'}$  decays to  $W^{\pm}$  and  $Z$  boson, which then decay into  $l^+ l^- l^{\pm} \nu$ . This particular channel is the channel of interest in this thesis.

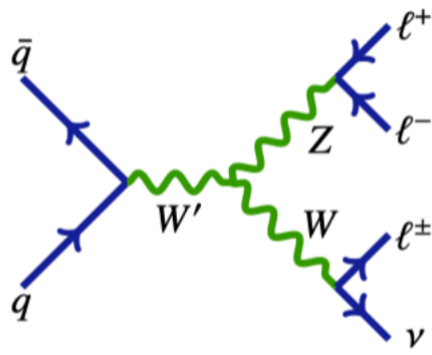


FIGURE 2.3.1: Feynman diagram of the  $W'$  production via the Drell-Yan process, its decay to  $W$  and  $Z$  bosons and the subsequent production of  $\ell^+ \ell^- \ell^\pm \nu$ .

## THE LARGE HADRON COLLIDER AND THE ATLAS DETECTOR

### 3.1 The Large Hadron Collider

The **Large Hadron Collider** (LHC) is the world's largest and highest energy particle collider. LHC accelerates particle beams, who travel in opposite directions. The particles that make up the beams are usually protons or ions, particles known as hadrons. During the acceleration, the beams reach approximately the speed of light, before colliding at certain interaction points, where detectors are situated.

The LHC consist of a 27-kilometer ring of superconducting magnets with a number of accelerating structures that boost the energy of the particles along the way, located in a tunnel 100 meters underground at the European Organization for Nuclear Research (CERN), on the Franco-Swiss border near Geneva, Switzerland. [2]

The LHC is the last piece of the CERN accelerator complex chain, which is a group of machines that gradually increase the energy of the beam. The beam is inserted in one machine, is accelerated and then is inserted in the next machine. Following this procedure, the beam reaches its highest energy.

The first collisions were achieved in 2010 with energies between 3.5 TeV and 4 TeV per beam (Run 1). After some upgrades, it reached the energy of 6.5 TeV per beam, which means a total of 13 TeV in the center of mass frame ( $\sqrt{s} = 13$  TeV, Run 2). At 2018, it was shut down for maintenance and upgrading reasons. During 2022 it restarted, aiming at an energy of  $\sqrt{s} = 14$  TeV (Run 3).

Each of the energies achieved was accompanied by its own luminosity. For a center



of mass energy of  $\sqrt{s} = 7$  TeV, the corresponding luminosity was  $L = 6.1 \text{ fb}^{-1}$ . For a center of mass energy of  $\sqrt{s} = 8$  TeV, the luminosity was  $L = 23 \text{ fb}^{-1}$ , and finally, for a center of mass energy of  $\sqrt{s} = 13$  TeV, the luminosity was  $L = 139 \text{ fb}^{-1}$ .

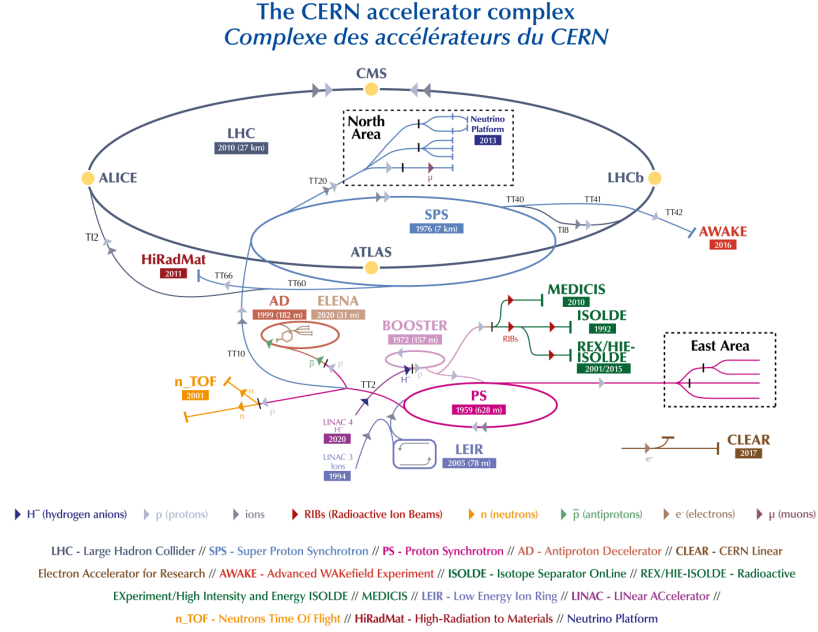


FIGURE 3.1.1: LHC acceleration complex.

At the collision points, four main detectors are situated, which constitute the main experiments in the LHC:

- **ATLAS (A Torroidal LHC ApparatuS)**: A general purpose detector, that focuses on High-Energy Physics Studies.
- **CMS (Compact Muon Solenoid)**: Again a general purpose detector, that focuses on High-Energy Physics Studies.
- **ALICE (A Ion Collider Experiment)**: A detector for heavy ion collisions, that aims to study the strong interactions and the quark gluon plasma, at extreme energy density and temperature.
- **LHC-b**: A detector that aims to study the physics of b-quarks.

## 3.2 The ATLAS detector

ATLAS is one of the two general - purpose detectors at the LHC. It investigates a wide range of physics, from the Higgs boson to extra dimensions and particles that could make up dark matter. ATLAS has the dimensions of a cylinder, 46 meters long, 25 meters in diameter and sits in a cavern 100 meters below the ground. It weights over 7000 tons and has a solid angle coverage of almost  $4\pi$ .

### 3.2.1 ATLAS structure

The detector itself is a many-layered instrument. It consists of six different detecting subsystems wrapped concentrically in layers around the collision point to record the trajectory, momentum and energy of the particles, allowing them to be individually identified and measured. A huge magnet system bends the paths of the charged particles so that their momenta can be measured as precisely as possible [10]. Bellow the main components of the ATLAS detector are briefly presented:

- **Inner Detector**

The Inner Detector is very compact and highly sensitive. It consists of three different systems of sensors all immersed in a magnetic field parallel to the beam axis. The Inner Detector measures the direction, momentum, and charge of electrically-charged particles produced in each collision. [11]

- **Caloreimeters**

The ATLAS detector consinsts of two types caloremeters. The **Eletromagnetic Caloremeter** and the **Hadronic Caloremeter**. Electromagnetic calorimeters measure the energy of electrons and photons as they interact with matter. Hadronic calorimeters sample the energy of hadrons (particles that contain quarks, such as protons and neutrons) as they interact with atomic nuclei. Calorimeters can stop most known particles except muons and neutrinos. [9]

- **Muon Spectrometer**

The outer layer of the ATLAS experiment is made of muon detectors. They identify and measure the momenta of muons. Muons are very penetrative particles which allows them to cross the thick layers of the ATLAS Calorimeters. [13]

### • Magnet System

The magnet system of ATLAS bends the trajectories of charged particles, enabling scientists to measure their momentum and charge. This is done using two different types of superconducting magnet systems – solenoidal and toroidal. These impressive systems are cooled to about 4.5 K ( $-268^{\circ}\text{C}$ ) in order to provide the necessary strong magnetic fields. [12]

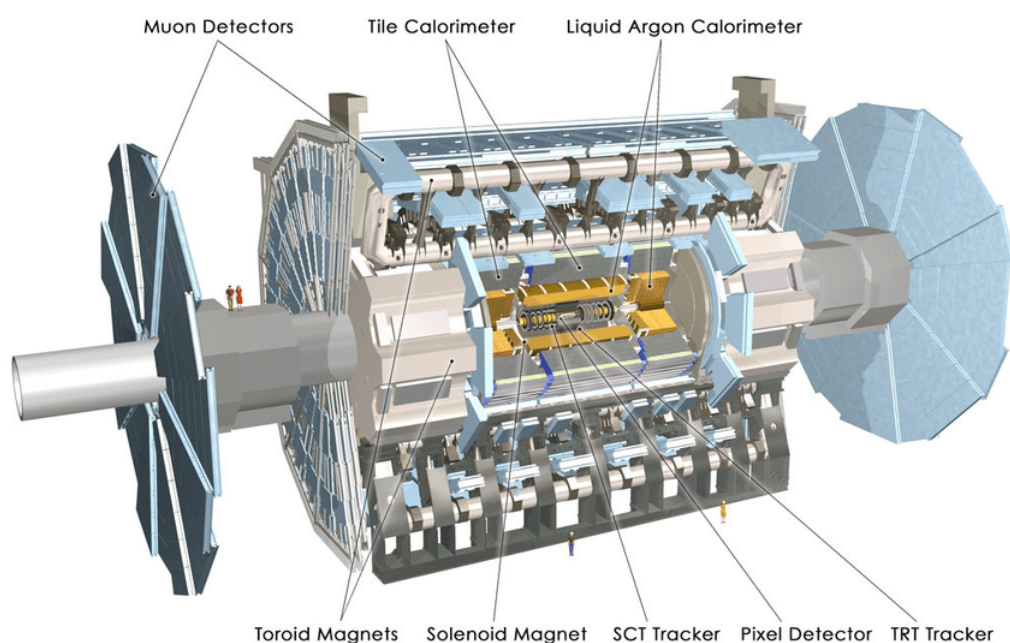


FIGURE 3.2.1: The ATLAS detector and its main components.

### 3.2.2 ATLAS coordinate system

The ATLAS detector defines its own coordinate system, where the  $z$ -axis is defined as parallel to the direction of the beam, while the  $x$ - $y$  is transverse to the direction of the beam. The positive  $x$ -axis is defined as pointing from the interaction point to the centre of the LHC ring while the positive  $y$ -axis is defined as pointing upwards. The azimuthal angle  $\phi$  is measured around the beam axis and the polar angle  $\theta$  is the angle from the beam axis.

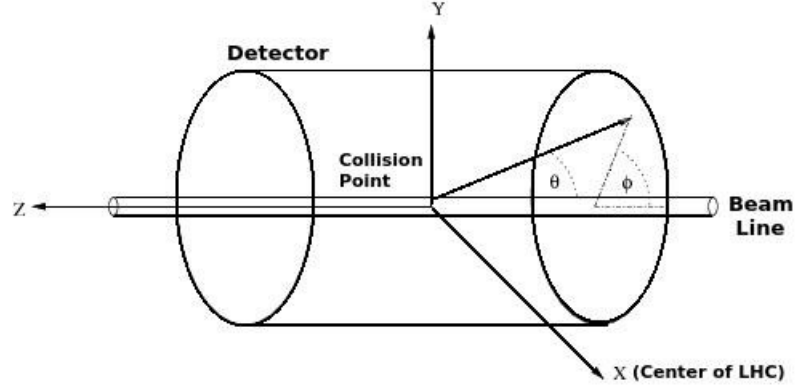


FIGURE 3.2.2: The coordinate system of the ATLAS detector.

Based on the coordinate system and on the polar and azimuthal angles, some useful variables are defined. First of all, **pseudorapidity** is defined as:

$$\eta = -\ln \tan \left( \frac{\theta}{2} \right) \quad (3.2.2.1)$$

From **Equation** 3.2.2.1 it is clear that there is a correspondence between the polar angle and the quantity of pseudorapidity, which is illustrated in **Figure** 3.2.3:

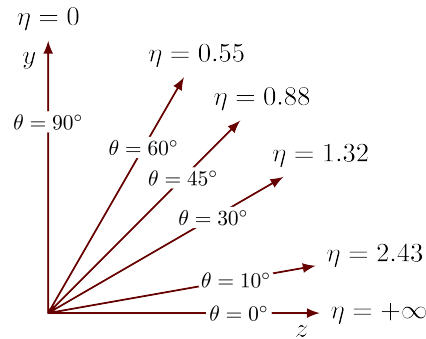


FIGURE 3.2.3: The correspondence between  $\eta$  and the polar angle  $\theta$ .

Moreover, the quantity of rapidity is defined as:

$$y = \frac{1}{2} \ln \left( \frac{E + p_z}{E - p_z} \right) \quad (3.2.2.2)$$

Finally, the distance  $\Delta R$  in the pseudorapidity-azimuthal plane is defined as :

$$\Delta R = \sqrt{\Delta \eta^2 + \Delta \phi^2} \quad (3.2.2.3)$$

## DATA AND MONTE CARLO SAMPLES

In the present thesis, all the data used for the analysis were stored in NTuples. NTuples are suitable for storing information event by event and contain all the information needed for the analysis. Each event is associated with a set of values, which correspond to the kinematic variables of the reconstructed objects. Objects such as electrons, muons, jets and missing transverse energy have been reconstructed prior to the analysis performed in the rest of this thesis. The information for all the events is then stored in ROOT files, and can be accessed via the MakeClass command, which creates code that loops over all the events. Via this loop, the information for the kinematic variables can be stored in histograms and analyzed further.

### 4.1 Data Samples

The data samples used in the analysis that is performed in this thesis are collected from proton - proton collisions with a center of mass energy of  $\sqrt{s} = 13$  TeV, with the ATLAS detector at the LHC. The samples used have an integrated luminosity of  $139 \text{ fb}^{-1}$ , that comes with an uncertainty of 2%, which will later be used as a source of systematic uncertainty.

### 4.2 Monte-Carlo Signal Samples

The MC signal samples are used to simulate the physics processes, based on the benchmark models described in **Chapter 2.2** in [19]. In the present thesis, only the Heavy Vector Triplet model is considered.

For the case of the Drell-Yan production, the samples were generated at Leading Order (LO) in QCD with Madgraph 2.6.5 interfaced to Pythia8 (for parton-level hadronization), for masses of diboson resonances range from 250 GeV to 5 TeV. All lepton flavors were included in  $Z \rightarrow ll$  and  $W \rightarrow lv$  decays.

The HVT production via the Drell-Yan process, which predicts the decay  $W' \rightarrow WZ \rightarrow lvll$ , uses two benchmark models to describe the results, as stated in **Chapter 2.2.2.1** of [19]. In the present thesis, only Model A was considered. Model A describes weakly coupled vector resonances arising from an extension of the SM gauge group with an additional  $SU(2)$  symmetry. The parameter  $g_v$  is set to 1 for Model A, while the parameter  $c_F$  is also set to 1 and remains the same for all fermions.

### 4.3 Monte-Carlo Background Samples

The dominant background for this analysis, is the SM WZ Inclusive process. This background was simulated using the *SHERPA 2.2.2* generator. The simulation of this background was performed requiring the existence of two QCD vertices and four electroweak vertices at LO. Thus, the matrix element squared is proportional to  $\alpha_S^2 \alpha_{EW}^4$ . Since  $\alpha_S$  is much larger than  $\alpha_{EW}$  in the typical energies we are studying, this process is much more probable to occur than the purely electroweak process. This specific background will be referred to as **WZ-QCD**. Any information about the associated jets is neglected, since only the Drell-Yan  $W'$  production is studied in this thesis.

Moreover, MC samples were used to simulate the purely electroweak process  $WZjj \rightarrow lvlljj$ , which will be referred to as **WZ-EW**. This background was simulated using the *MADGRAPH 2.7.3* along with *PYTHIA 8.244* generators. Since this process is purely electroweak, the simulation was performed requiring the existence of six electroweak vertices at LO. Thus, the matrix element squared is proportional to  $\alpha_{EW}^6$ , making this process less probable than the QCD production. Again here, due to the study of the Drell-Yan  $W'$  production, any information about the associated jets is neglected.

Furthermore, processes that involve the production of two Z bosons, such as  $\bar{q}q \rightarrow ZZ \rightarrow 4l$ ,  $\bar{q}q \rightarrow ZZ \rightarrow 2l2\nu$  and gluon - gluon fusion processes such as  $gg \rightarrow ZZ \rightarrow 4l$  are also considered a background in this analysis, and will be referred to as **ZZ**. All of these processes are simulated using the *SHERPA 2.2.2* generator.

Processes that include triboson decays to leptons and neutrinos are also simulated using *SHERPA 2.2.2*. Along with triboson decays, the contribution of  $\bar{t}tV$  processes are considered. The latter are simulated using the *MADGRAPH 2.3.3* generator. The total contribution of these two backgrounds is summed up and will be referred to as  $\bar{t}tV + VVV$ .

Last but not least, SM processes that produce at least one misidentified lepton or non-prompt lepton, such as  $Z + \gamma$ ,  $Z + \text{jets}$  or  $\bar{t}t$  pairs are contributing as background and will be referred to as **Fake/Non - prompt**. The process via which the distributions of this particular background are generated is data driven method, which is not performed or discussed in this thesis. All the distributions concerning this background are taken from [19].

As a final note, it can be commented that SM processes that include the Higgs boson ( $H$ ,  $\bar{t}tH$ ,  $VVH$ ) are neglected in this analysis, because they are expected to contribute less than 0.1% of the total background because of their low cross-section.

## EVENT SELECTION

### 5.1 Determination of basic variables

The determination of some kinematic variables are of paramount importance in the present analysis. This section presents the way in which some of the most important kinematic variables are calculated.

#### 5.1.1 WZ system Invariant Mass

The invariant mass of the WZ system is one of the most important variables that are about to be used in this analysis. However, the challenge in achieving an accurate measurement of the invariant mass lies in the lack of knowledge associated with the neutrino four - vector. In order to calculate the invariant mass of the system, one has to solve the equation:

$$E_{WZ}^2 = p_{WZ}^2 + m_{WZ}^2 \quad (5.1.1.1)$$

The energies and momenta of the Z leptons can be measured, and the four - vector of the Z boson can be reconstructed. The ambiguity in the calculation is inserted via the unknown neutrino four - vector. Since we can only measure  $E_T^{miss}$ , which is the energy associated with the neutrino, and the four - vector of the W lepton is determined, the unknown longitudinal component  $p_z^\nu$  can be calculated. If this component is calculated, then the four - vector of the neutrino is also known. Hence, the four - vector of the W boson is determined, as well as the mass of the WZ system. In the rest frame of the W



boson:

$$\begin{aligned} m_W^2 &= (p_l + p_\nu)^2 = (E_l + E_\nu)^2 - (\vec{p}_l + \vec{p}_\nu)^2 \Leftrightarrow \\ \frac{m_W^2}{2} &= E_l E_\nu - \vec{p}_l \cdot \vec{p}_\nu \end{aligned} \quad (5.1.1.2)$$

where:

$$E_\nu = \sqrt{(p_T^\nu)^2 + (p_z^\nu)^2} \quad (5.1.1.3)$$

$$\vec{p}_l \cdot \vec{p}_\nu = p_T^\nu p_T^l \cos(\phi^\nu - \phi^l) + p_z^\nu p_z^l \quad (5.1.1.4)$$

By substituting **Equations** 5.1.1.3 and 5.1.1.4 in **Equation** 5.1.1.2, the latter will take the form:

$$(p_z^\nu)^2 [E_l^2 - (p_z^l)^2] - 2B p_z^\nu p_z^l + [E_l^2 (p_T^\nu)^2 - B^2] = 0 \quad (5.1.1.5)$$

where:

$$B = \frac{m_W^2}{2} + p_T^\nu p_T^l \cos(\phi^\nu - \phi^l) \quad (5.1.1.6)$$

The **Equation** 5.1.1.5 is a quadratic equation, which will lead to two solutions. These two solutions will either be real or complex:

$$p_z^\nu = \frac{B p_z^l \pm E_l \sqrt{B^2 + (p_T^\nu)^2 [(p_z^l)^2 - E_l^2]}}{E_l^2 - (p_z^l)^2} \quad (5.1.1.7)$$

From **Equation** 5.1.1.7 it can be seen that there is no obvious reasoning behind which solution is the optimal to accurately reconstruct the invariant mass. The option that provides the best resolution in the invariant mass calculation has been studied in section 5.6.2 in [14] and is the following: In the case of two real solutions, the one with the smaller magnitude is chosen. If there is no real solution, the real part of the solution with the smaller magnitude is chosen. Using the reconstructed neutrino four-vector, the four-vector of the W boson can be reconstructed, as well as the invariant mass of the WZ system.

## 5.1.2 W boson and WZ system Transverse Mass

The transverse mass of the W boson is defined as:

$$m_T^W = \sqrt{2 p_T^l E_T^{miss} (1 - \cos(\phi^\nu - \phi^l))} \quad (5.1.2.1)$$

In **Equation** 5.1.2.1, the variables  $\phi^\nu$  and  $\phi^l$  stand for the angles of the momenta for the neutrino and the W lepton respectively, in the transverse plane.

The WZ transverse mass is reconstructed by taking the four-vectors of the final state leptons (associated to the W and Z bosons) projected on the transverse plane by neglecting their longitudinal component. Hence, the transverse mass of the WZ system is defined as:

$$m_T^{WZ} = \sqrt{\left(\sum_{l=1}^3 p_T^l + E_T^{miss}\right)^2 - \left(\sum_{l=1}^3 p_x^l + E_x^{miss}\right)^2 - \left(\sum_{l=1}^3 p_y^l + E_y^{miss}\right)^2} \quad (5.1.2.2)$$

## 5.2 Inclusive WZ event selection

This section will present WZ inclusive selection criteria. The selection is performed in order to secure an Inclusive Phase Space, which will lead to more of the desired signal. The criteria for this analysis is summarized briefly in **Table** 5.2.1 and are discussed in greater detail in [5].

WZ Inclusive Selection	
Event Cleaning	Reject LAr, Tile and SCT corrupted events and incomplete events
Primary vertex	Hard scattering vertex with at least two tracks
Trigger	Single lepton (electron or muon) trigger
Jet cleaning	Pass DFCommonJetseventCleanLooseBad
ZZ veto	Veto events with additional Baseline leptons
N Leptons	Exactly three leptons passing the “loose” lepton selection with $p_T > 25$ GeV
Z candidate	Built from Same-Flavor-Opposite-Sign (SFOS) lepton pair with $m_{ll}$ closest to Z PDG mass
W candidate	Built from the third lepton and $E_T^{miss}$
W , Z selection	Z leptons passing “tight(Z)” lepton selection W leptons passing “tight(W)” lepton selection
Mass Window	$ m_{ll} - m_Z  < 20$ GeV
Missing Energy	$E_T^{miss} > 25$ GeV

TABLE 5.2.1: The analysis’ event selection criteria

### 5.3 WZ Inclusive Control Distributions

To verify the agreement between MC and data, the inclusive distributions for sixteen different kinematic variables are presented, for all events satisfying the selection criteria described in **Table 5.2.1**.

These control distributions depict the agreement between the data and the sum for all possible contributions that pass the above mentioned selection criteria. Each event that comes from a MC sample is scaled to the luminosity of the data using the MC cross section and the k-factor of each sample. This leads to an overall scaling factor:

$$\text{Scaling factor} = \frac{\text{k-factor} \cdot \text{Cross Section} \cdot \text{Luminosity}}{\text{Sum of Weights}} \quad (5.3.0.1)$$

As it can be witnessed from the figures following, there is good agreement between data and MC predictions.

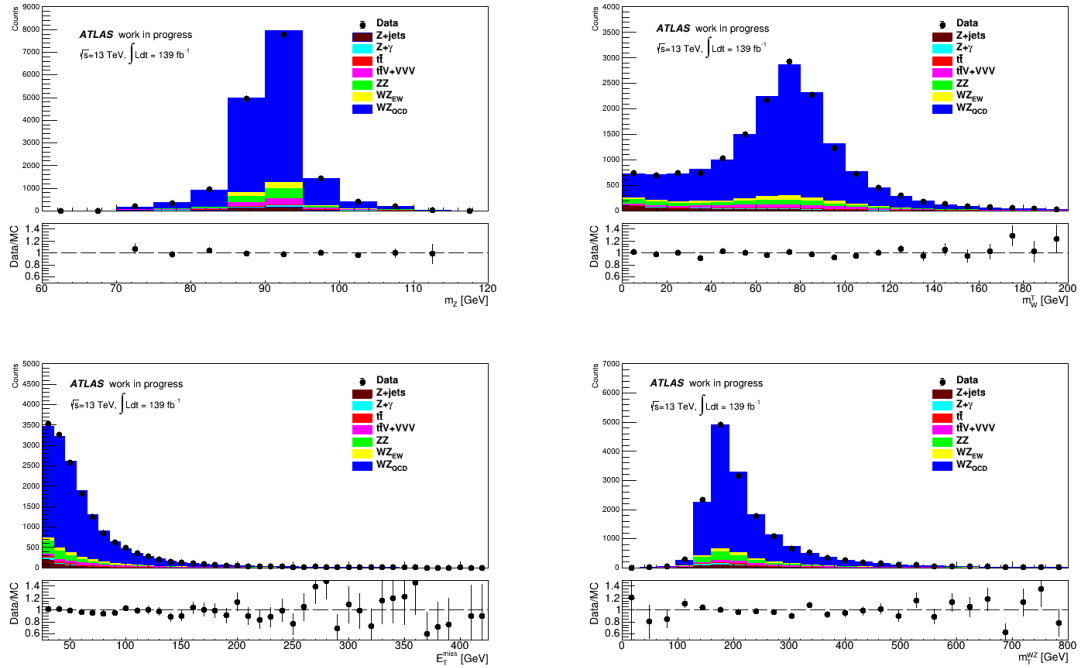


FIGURE 5.3.1: Control distributions of Z boson mass  $m_Z$  (upper left), W boson transverse mass  $m_T^W$  (upper right), missing transverse energy  $E_T^{miss}$  (down left) and WZ system transverse mass  $m_T^{WZ}$  (down right). All MC expectations are scaled to the scaling factor of 5.3.0.1.

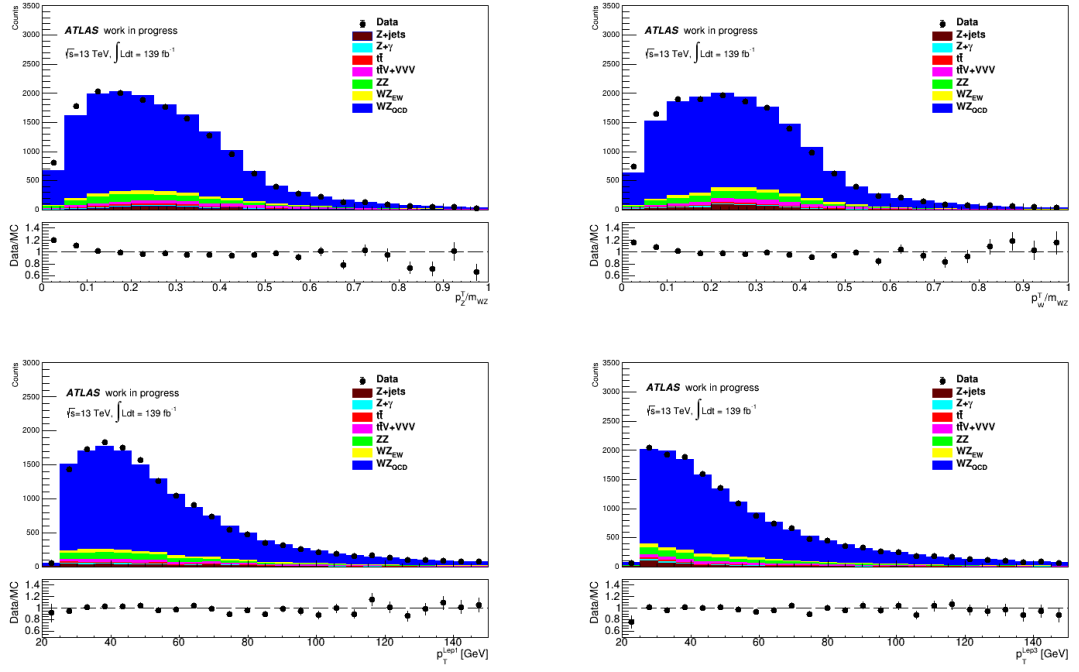


FIGURE 5.3.2: Control distributions of  $\text{PtBalanceZ } p_T^Z / m_{WZ}$  (upper left),  $\text{PtBalanceW } p_T^W / m_{WZ}$  (upper right), first and third lepton transverse momenta  $p_T^{Lep1}$  (down left) and  $p_T^{Lep3}$  (down right).

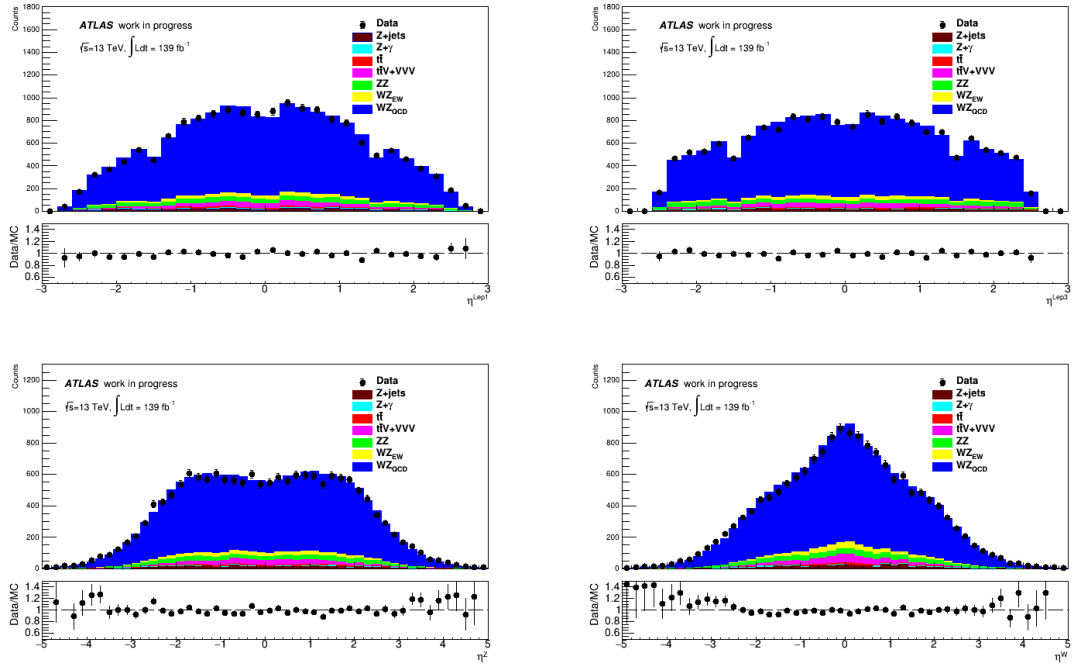


FIGURE 5.3.3: Control distributions of first and third lepton pseudorapidities  $\eta^{Lep1}$  (upper left) and  $\eta^{Lep3}$  (upper right) and the pseudorapidities of the Z and W bosons  $\eta^Z$  (down left) and  $\eta^W$  (down right).

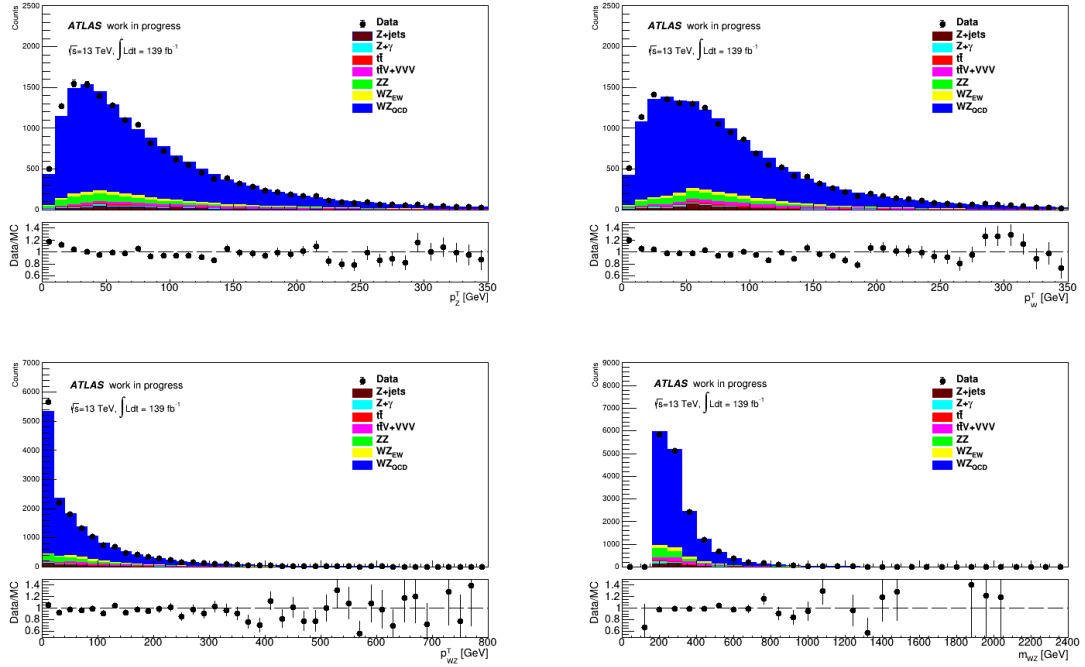


FIGURE 5.3.4: Control distributions of the W and Z bosons transverse momenta  $p_T^Z$  (upper left) and  $p_T^W$  (upper right), the transverse momentum of the WZ system  $p_T^{WZ}$  (down left) and the invariant mass of the WZ system  $m_{WZ}$  (down right).

## 5.4 Drell-Yan Signal Region Definition

The Drell-Yan SR is built on top of the WZ Inclusive criteria that were mentioned before. However, in order to reduce the events that pass the WZ Inclusive criteria, we need a few more selection criteria, that will help us discriminate between the main WZ SM background and the resonant WZ events.

Two interesting variables that succeed in discriminating between the signal and the main WZ SM background are the ratios  $p_T^Z/m_{WZ}$  and  $p_T^W/m_{WZ}$ , which will be referred to as **PtBalanceZ** and **PtBalanceW**, respectively. So, in order to keep as many resonant events as possible, the events that belong to the Drell-Yan SR are also required to satisfy  $p_T^Z/m_{WZ} > 0.35$  and  $p_T^W/m_{WZ} > 0.35$ . The optimal cut value of 0.35 has been used in earlier publications and its study is beyond the scope of this thesis.

As it obvious from **Figure 5.4.1** and **Figure 5.4.2**, PtBalanceZ and PtBalanceW offer a great separation between the signal and the main WZ SM background.

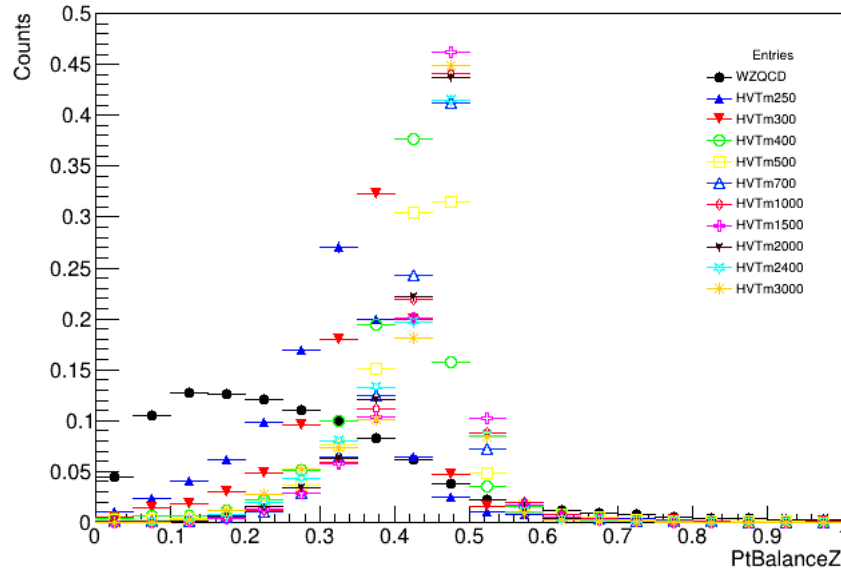


FIGURE 5.4.1: WZ QCD background versus various Drell-Yan signals for PtBalanceZ normalized to unit.

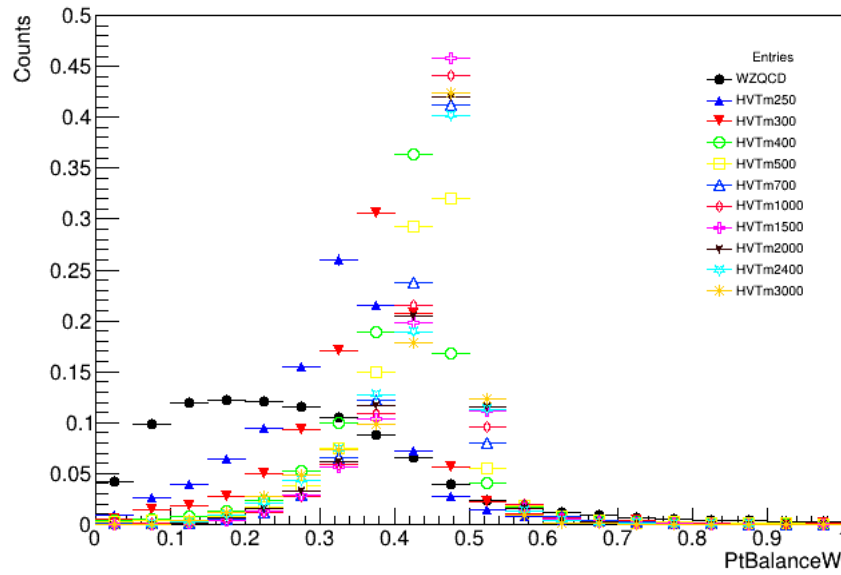


FIGURE 5.4.2: WZ QCD background versus various Drell-Yan signals for PtBalanceW normalized to unit.

## BACKGROUND ESTIMATION

As background processes are defined all the processes that have the same  $W^\pm Z$  signature and leptonic final state, but differ from the desired signal process. The background processes can be classified into two categories:

- **Irreducible Backgrounds:** All the final state leptons arise from the primary process (prompt leptons)
- **Reducible Backgrounds:** At least one lepton is not prompt (fake/non prompt leptons)

### 6.1 Reducible Background

Reducible backgrounds consist of SM processes where one or two leptons coming from jets or photons, for example:

- Background due to fake leptons. These leptons come from kaon, pion or heavy quark decays to real leptons, in addition to jets being misidentified as leptons. The main sources of this background are processes like  $Z$ +jets,  $t\bar{t}$ ,  $Wt$ ,  $WW$  or QCD multijet processes where one or two jets are misidentified as leptons
- $Z + \gamma$  processes where the photon is misidentified as an electron

As it was stated in **Chapter 4.3**, the distributions involving the reducible background, which is referred to as **Fake/Non prompt** are obtained using a data driven method

that is based on a global matrix which exploits the differences in object characteristics between real and fake/non-prompt leptons on a statistical basis. This method is not discussed or performed in this thesis. All the the distributions concerning this background are taken from [19].

## 6.2 Irreducible Background

Irreducible backgrounds consist of SM processes that produce three prompt leptons, which are leptons that come directly from the decays of the vector bosons:

- WZ process that has exactly three leptons passing the event selection. This process comes in two modes, the QCD and the EW, with the QCD being the dominant in all signal regions
- ZZ process where three leptons pass the selection criteria and the fourth lepton is not reconstructed or identified
- $t\bar{t}V$  where  $V = W, Z$
- $VVV$  where  $V = W, Z$

In the analysis performed in the present thesis, the distributions for all the above stated backgrounds are taken from MC simulations. The Drell-Yan SR is associated with two CRs, the WZ-QCD CR and the ZZ CR, which are designed to have high purity, small statistical uncertainties in terms of the background process of interest and to contain only a small fraction of the potential signal. These CRs are built in order to estimate the normalization factors associated with each one, and thus correct our MC predictions with respect to the data. The selection requirements for the Drell-Yan SR and its associated CRs are demonstrated in the **Table 6.2.1**:

Regions	Signal Region	Control Regions	
Selection	Drell-Yan	ZZ Drell-Yan	WZ-QCD Drell-Yan
$E_T^{miss} > 25 \text{ GeV}$	✓	fail	✓
4 lepton veto	✓	fail	✓
WZ Inclusive	✓	fail	✓
$p_T^{W/Z}/m_{WZ} > 0.35$	✓		fail (but $p_T^{W/Z}/m_{WZ} > 0.1$ )

TABLE 6.2.1: Selection Criteria for the Drell-Yan SR and the dedicated CRs.



### 6.3 Drell-Yan Control Regions

In this section, the CR distributions of three different kinematic variables are about to be presented. These CRs are expected to be enriched in background events of the type we are interested to estimate the scale factor (e.g. ZZ or WZ-QCD). After constructing each CR, the background distributions are fitted to the data using the **Binned Maximum Likelihood Method**, in order to extract the corresponding normalization factor and correct the MC predictions with respect to the data.

In this thesis, two approaches are adopted in order to estimate the normalization factors for each CR. The first approach is that each CR is fitted individually, and the best-fit values are inserted directly in the SR to normalize the SR background distributions. The second approach uses a simultaneous Maximum Likelihood Fit, involving the distributions for the two CRs and the Drell-Yan SR. The results for these two methods will be presented and compared later in this Chapter.

### 6.4 The Binned Maximum Likelihood Model

All the distributions that are about to be shown are binned. Each bin is considered to follow a *Poisson Distribution*. Thus, the Likelihood function will be constructed as the product of the Poissonian probabilities for all the bins. Each term that is inserted in the product gives the probability of having  $n_i$  data, when  $\mu s_i + b_i$  are expected. The index  $i$  stands for the corresponding bin, while  $s_i$  and  $b_i$  stand for the signal and background events in each bin correspondingly. More explicitly:

$$L(\mu) = \prod_{i=1}^{N_{bins}} Pois(n_i | \mu s_i + b_i) = \prod_{i=1}^{N_{bins}} \frac{(\mu s_i + b_i)^{n_i}}{n_i!} e^{-(\mu s_i + b_i)} \quad (6.4.0.1)$$

In each CR, the MC events in each bin for the process associated with the CR play the role of the signal events, while all the other events coming from the other background processes play the role of the background events. For example, in the ZZ Drell-Yan CR, the bin content of the distribution corresponding to the ZZ background stands for  $s_i$ , while the sum of the bin contents of all the other background contributions stands for  $b_i$ . The unknown parameter we desire to estimate is  $\mu$ , and is obtained by maximizing the Likelihood function. For calculation purposes, it is easier to minimize the NLL

ratio:

$$-2 \ln \lambda(\mu) = -2 \ln \frac{L(\mu)}{L(\hat{\mu})} \quad (6.4.0.2)$$

In **Equation** 6.4.0.2,  $\hat{\mu}$  corresponds to the Maximum Likelihood estimator for  $\mu$ . According to the statistical theory, the value that corresponds to the minimum of the NLL ratio, is the best estimate of the unknown parameter. It is obvious that when  $\mu$  will take its best-fit value, the value of the NLL ratio will be zero. The values of the parameter for which the NLL ratio equals 1 correspond to the  $\hat{\mu} - 1\sigma$  and  $\hat{\mu} + 1\sigma$ . More details can be found in **Appendix C**.

## 6.5 ZZ Drell-Yan Control Region

The ZZ Drell-Yan CR is defined by requiring the presence of at least an additional fourth lepton and no requirement on the missing transverse energy.

**Figures** 6.5.1, 6.5.2 and 6.5.3 show the distributions of the WZ invariant mass, the numerical sum of the transverse momenta for the three leptons and the transverse mass of the WZ system in the ZZ Drell-Yan CR, respectively:

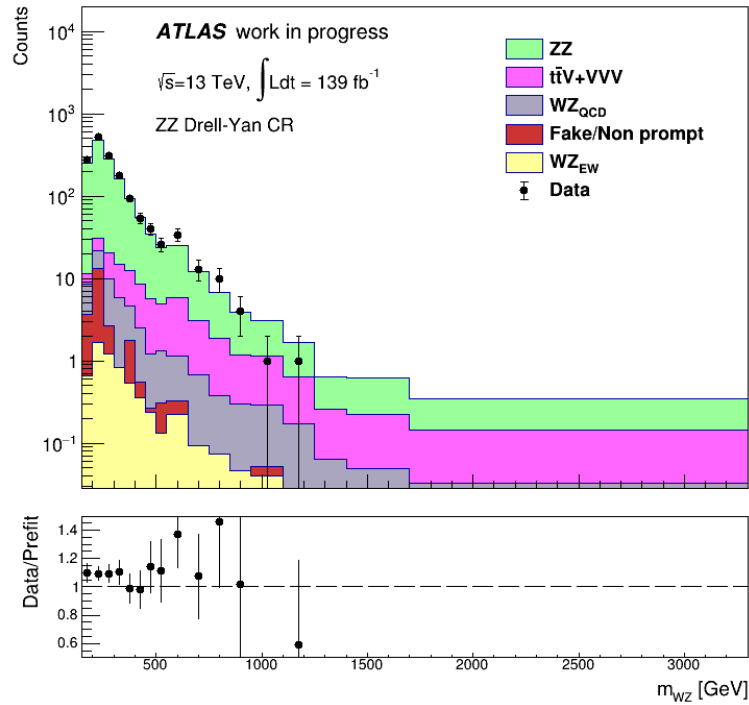
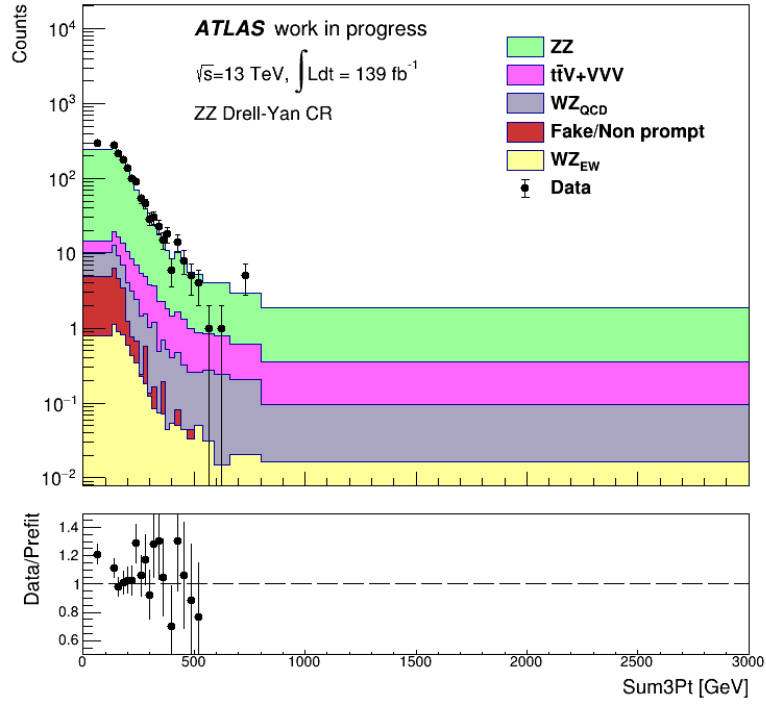
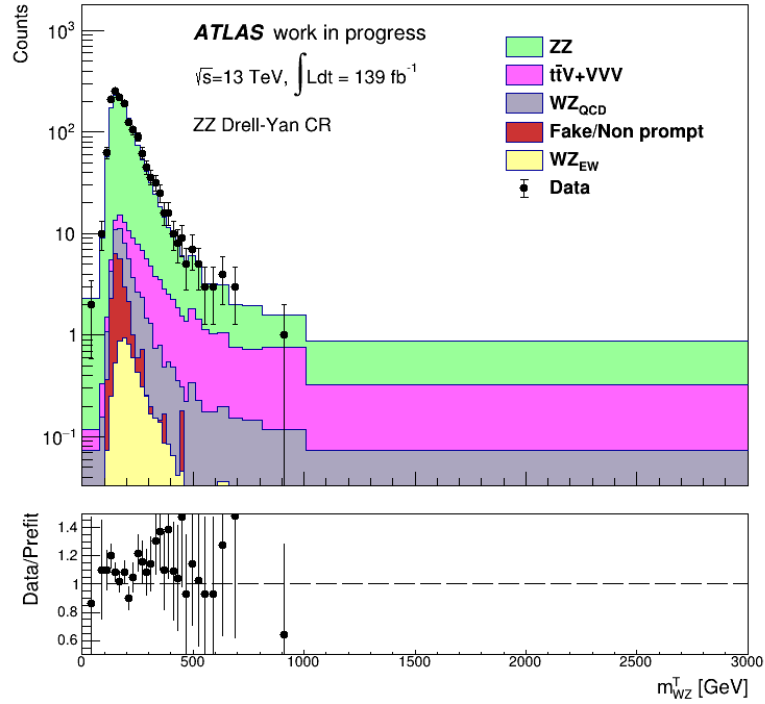


FIGURE 6.5.1: Pre-fit  $m_{WZ}$  distribution in the ZZ Drell-Yan CR.

FIGURE 6.5.2: Pre-fit  $\text{Sum3Pt}$  distribution in the ZZ Drell-Yan CR.FIGURE 6.5.3: Pre-fit  $m_{WZ}^T$  distribution in the ZZ Drell-Yan CR.

After fitting the data to the background distributions by minimizing the NLL ratio from **Equation** 6.4.0.2, the best estimated value for the normalization parameter were obtained for each variable. From the  $m_{WZ}$  distributions, it was obtained:

$$\mu_{ZZ} = 1.0967 \pm 0.0302 \quad (6.5.0.1)$$

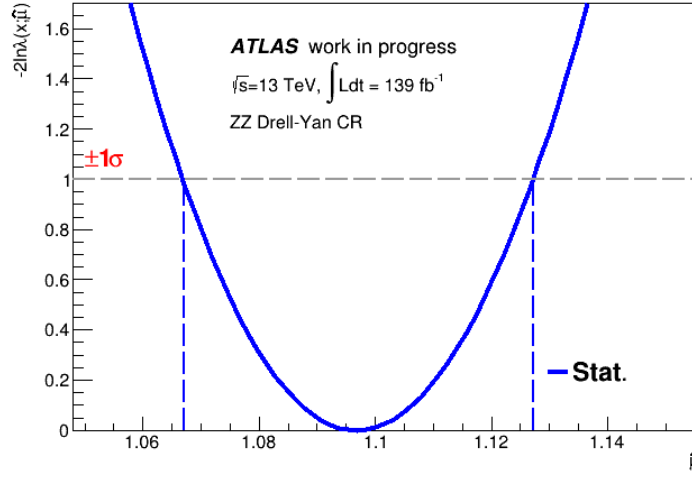


FIGURE 6.5.4:  $\mu_{ZZ}$  NLL ratio estimation using  $m_{WZ}$  as input.

From the  $Sum3Pt$  distributions, it was obtained:

$$\mu_{ZZ} = 1.0967 \pm 0.0302 \quad (6.5.0.2)$$

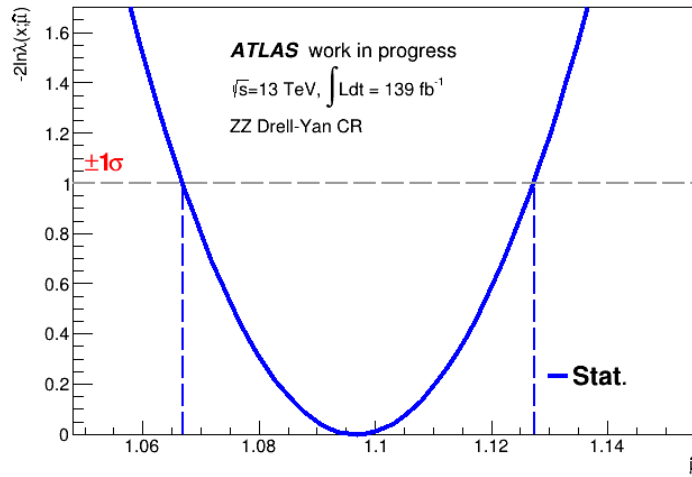


FIGURE 6.5.5:  $\mu_{ZZ}$  NLL ratio estimation using  $Sum3Pt$  as input.

Finally, from the  $m_{WZ}^T$  distributions, it was obtained:

$$\mu_{ZZ} = 1.0957 \pm 0.0302 \quad (6.5.0.3)$$

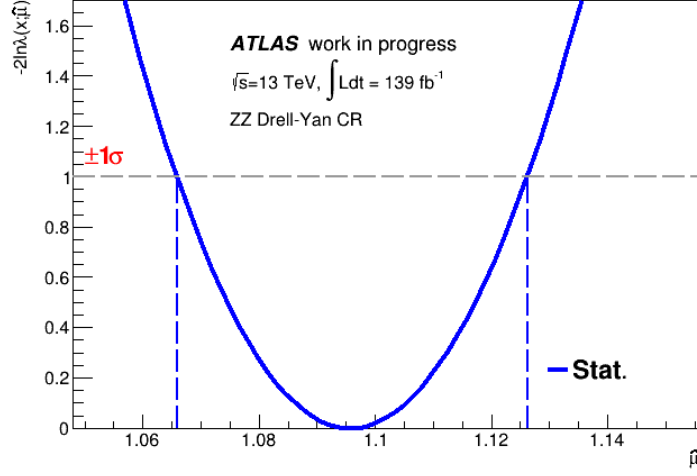


FIGURE 6.5.6:  $\mu_{ZZ}$  NLL ratio estimation using  $m_{WZ}^T$  as input.

The corresponding post-fit distributions are presented below:

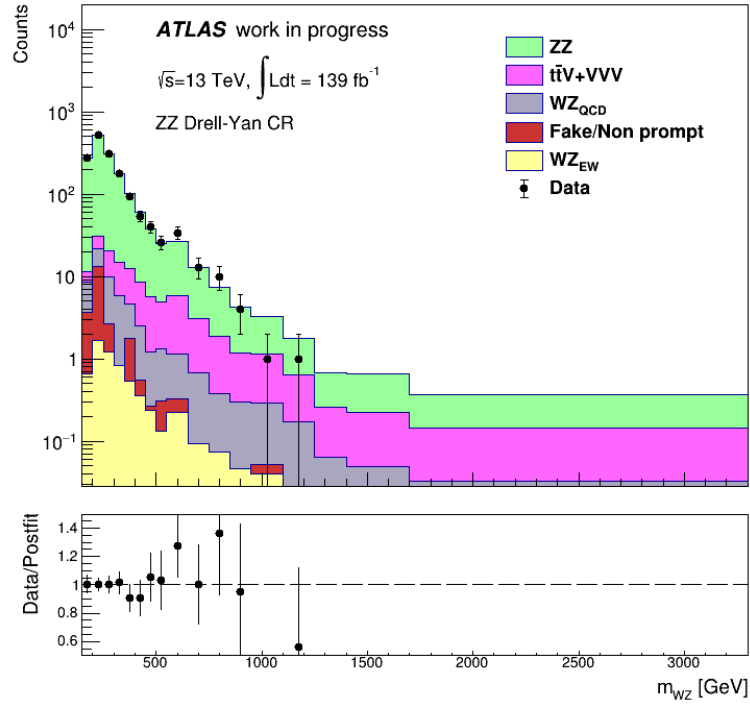


FIGURE 6.5.7: Post-fit  $m_{WZ}$  distribution in the ZZ Drell-Yan CR.

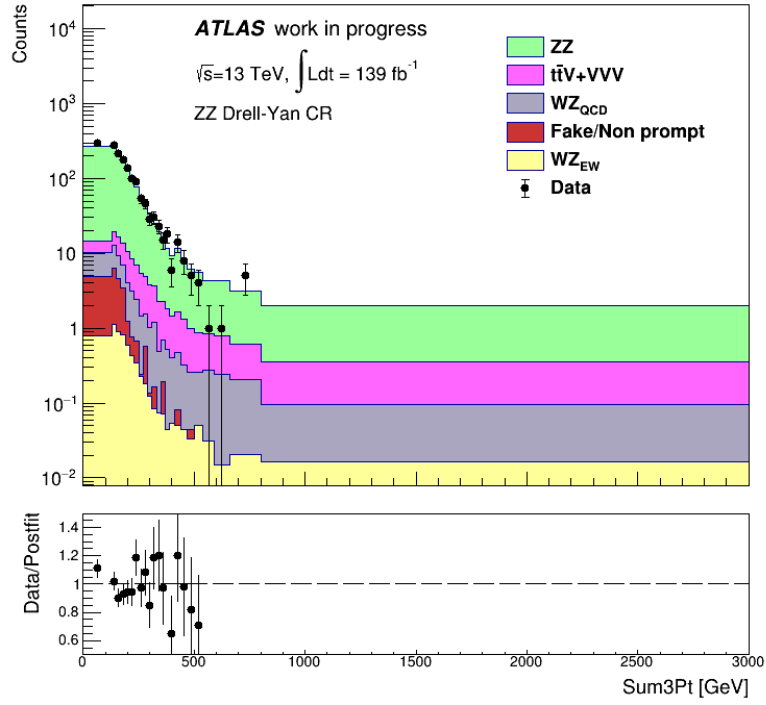


FIGURE 6.5.8: Post-fit  $\text{Sum3Pt}$  distribution in the ZZ Drell-Yan CR.

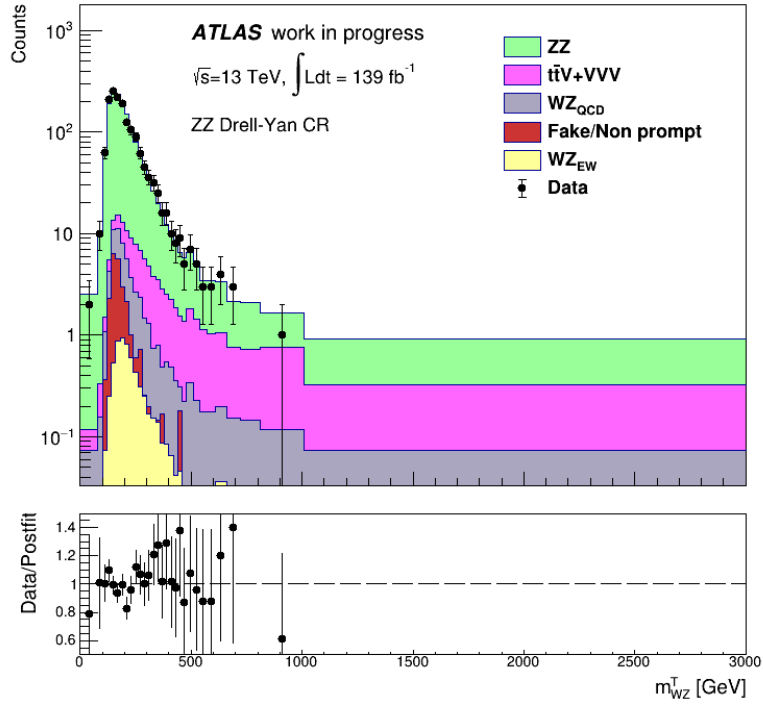


FIGURE 6.5.9: Post-fit  $m_{WZ}^T$  distribution in the ZZ Drell-Yan CR.

It is evident that the best fit-value for  $\mu_{ZZ}$  does not depend on the variable that was used as input for the distributions. The differences start to appear in the fourth decimal digit and are negligible.

Also, as it can be seen from the ratio plots, the data over the post-fit bin content ratio for every bin is closer to the value 1 for each variable, which is the purpose the normalization factor serves.

## 6.6 WZ-QCD Drell Yan Control Region

The WZ-QCD Drell-Yan CR selects WZ Inclusive events that fail the required PtBalance cut by having either  $p_T^W/m_{WZ} < 0.35$  or  $p_T^Z/m_{WZ} < 0.35$ . In order for this CR to be close to the SR, one extra requirement is added, which is that  $p_T^W/m_{WZ} > 0.1$  and  $p_T^Z/m_{WZ} > 0.1$ . By definition, this CR is orthogonal to the Drell-Yan SR.

**Figures 6.6.1, 6.6.2 and 6.6.3** show the distributions of the WZ invariant mass, the numerical sum of the transverse momenta for the three leptons and the transverse mass of the WZ system in the WZ-QCD Drell-Yan CR, respectively:

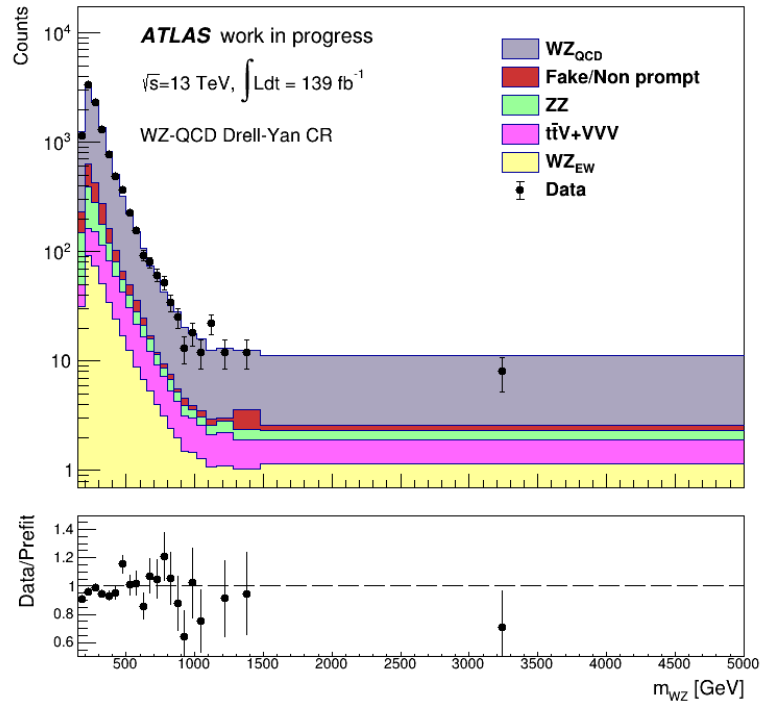
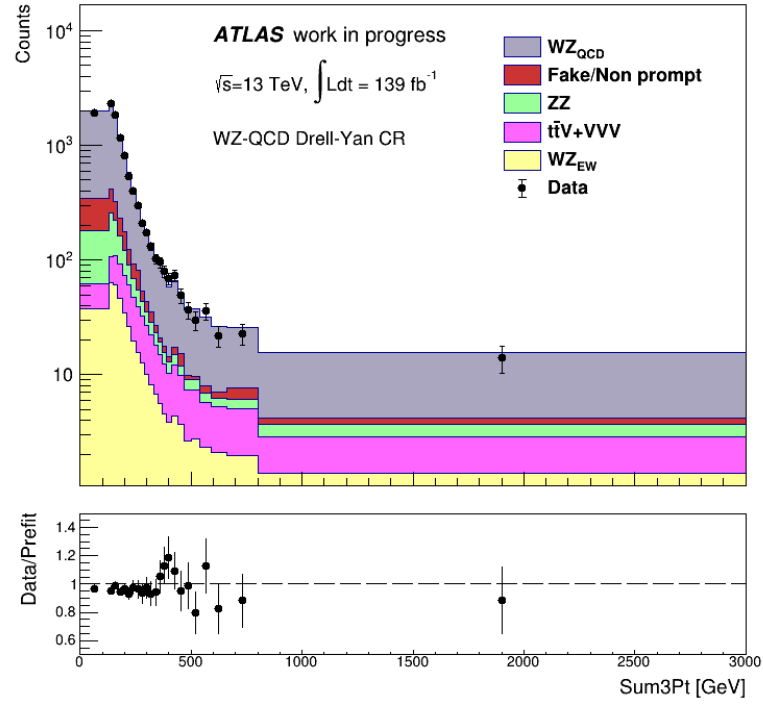
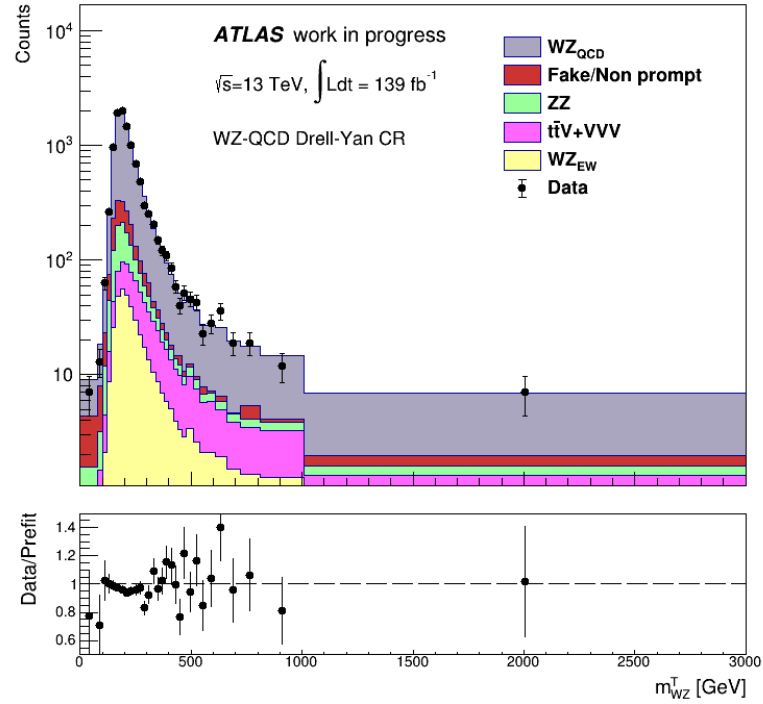


FIGURE 6.6.1: Pre-fit  $m_{WZ}$  distribution in the WZ-QCD Drell-Yan CR.

FIGURE 6.6.2: Pre-fit  $\text{Sum3Pt}$  distribution in the WZ-QCD Drell-Yan CR.FIGURE 6.6.3: Pre-fit  $m_{WZ}^T$  distribution in the WZ-QCD Drell-Yan CR.



By minimizing the NLL ratio from **Equation 6.4.0.2**, the best estimated value for the normalization parameter were obtained for each variable. From the  $m_{WZ}$  distributions, it was obtained:

$$\mu_{WZ}^{QCD} = 0.9559 \pm 0.0116 \quad (6.6.0.1)$$

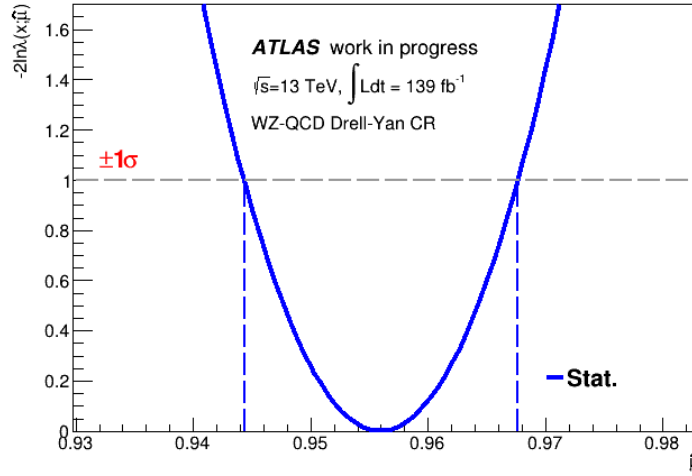


FIGURE 6.6.4:  $\mu_{WZ}^{QCD}$  NLL ratio estimation using  $m_{WZ}$  as input.

From the  $Sum3Pt$  distributions, it was obtained:

$$\mu_{WZ}^{QCD} = 0.9561 \pm 0.0116 \quad (6.6.0.2)$$

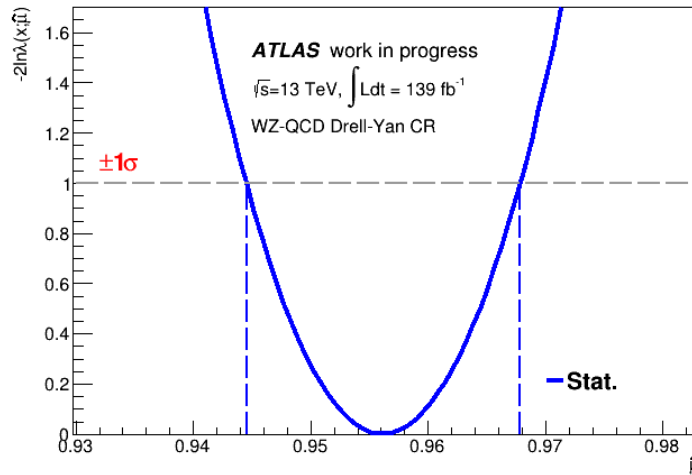


FIGURE 6.6.5:  $\mu_{WZ}^{QCD}$  NLL ratio estimation using  $Sum3Pt$  as input.

Finally, from the  $m_{WZ}^T$  distributions, it was obtained:

$$\mu_{WZ}^{QCD} = 0.9556 \pm 0.0116 \quad (6.6.0.3)$$

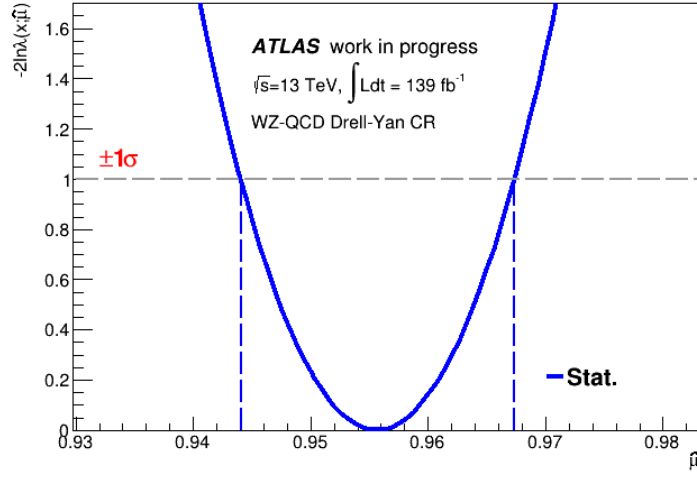


FIGURE 6.6.6:  $\mu_{WZ}^{QCD}$  NLL ratio estimation using  $m_{WZ}^T$  as input.

The corresponding post-fit distributions are presented below:

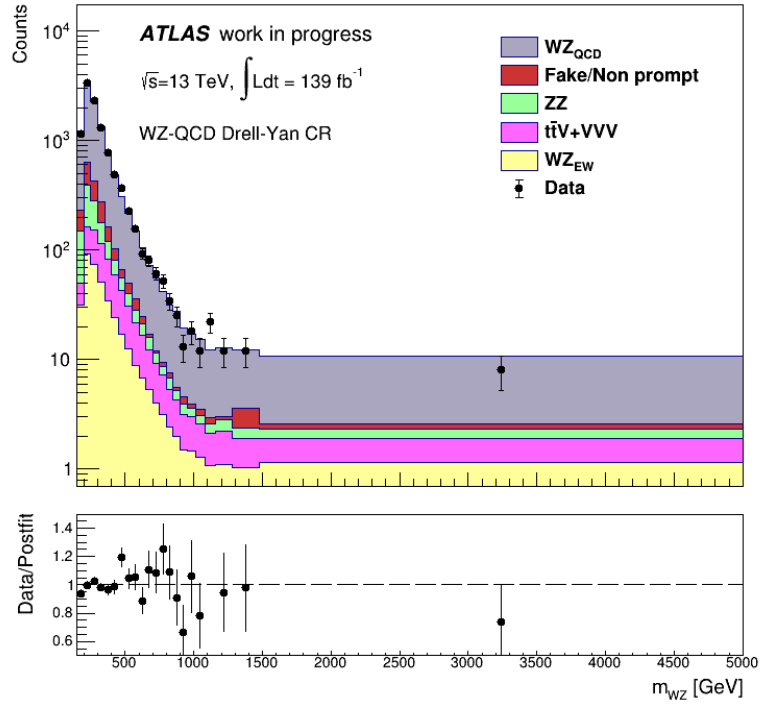
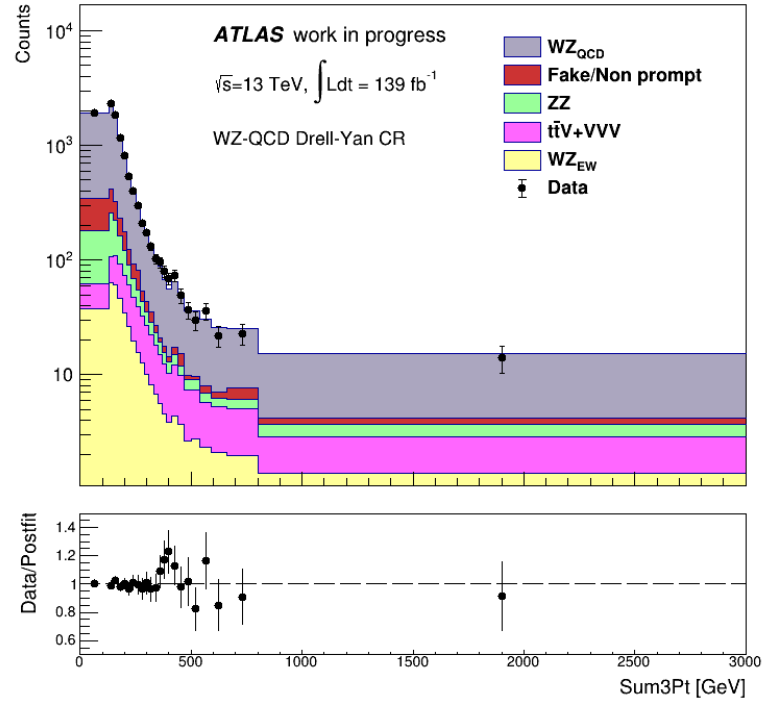
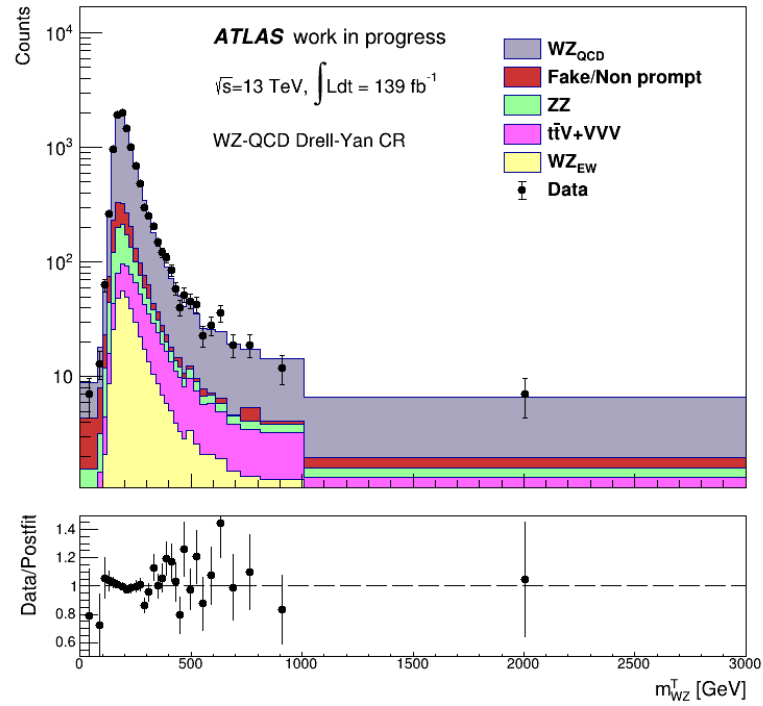


FIGURE 6.6.7: Post-fit  $m_{WZ}$  distribution in the WZ-QCD Drell-Yan CR.

FIGURE 6.6.8: Post-fit  $Sum3Pt$  distribution in the WZ-QCD Drell-Yan CR.FIGURE 6.6.9: Post-fit  $m_{WZ}^T$  distribution in the WZ-QCD Drell-Yan CR.

Again here, the conclusions drawn are the same. The best fit-value for  $\mu_{WZ}^{QCD}$  does not depend on the variable that was used as input for the distributions. Also, the data over the post-fit bin content ratio for every bin is closer to the value 1 for each variable.

## 6.7 Incorporating a Systematic Uncertainty

So far in this analysis, no systematic uncertainty was used in the Maximum Likelihood estimation. In this section, we will exploit the 2% luminosity uncertainty as a source of systematic uncertainty. In order to incorporate the luminosity systematic uncertainty in the Likelihood function, one extra term will be added in **Equation** 6.4.0.1:

$$L(\mu) = \prod_{i=1}^{N_{bins}} Pois(n_i | \mu s_i + b_i) G(L, \sigma_L) \quad (6.7.0.1)$$

The function  $G$  stands for a normalized Gaussian, with a mean value of  $L$  and a standard deviation of  $\sigma_L$ . The uncertainty in the luminosity is a factor that will affect the expected events in each bin. As described in [6], Barlow and Beeston proposed a method for representing such systematic uncertainties where one introduces a separate nuisance parameter multiplying the expected number of events in each bin. In general, these parameters are different in each bin, which is not the case here. Therefore, the Likelihood function of **Equation** 6.7.0.1, will be modified as:

$$L(\mu, x) = \prod_{i=1}^{N_{bins}} Pois(n_i | x(\mu s_i + b_i)) G(1, \sigma_x) \quad (6.7.0.2)$$

The mean value of this new parameter will be 1, whereas  $\sigma_x$  is the relative error of the prediction, which is set to 2%. Again, our main goal is to estimate the parameter of interest, which no other than  $\mu$ . The parameter  $x$  is just a nuisance parameter, and it is of no interest to estimate its best fit value. In order to take into account this nuisance parameter, we have to minimize the Profile Likelihood Ratio:

$$-2 \ln \lambda(\mu, \theta) = -2 \ln \frac{L(\mu, \hat{\theta})}{L(\hat{\mu}, \hat{\theta})} \quad (6.7.0.3)$$

In **Equation** 6.7.0.3,  $\theta$  plays the role of nuisance parameter. In order to minimize the PLR function with respect to  $\mu$ , a scan in its possible values is performed. In the numerator,  $\hat{\theta}$  stands for the best-fit value of the nuisance parameter for a particular

$\mu$ . Therefore, the numerator is the value of the Likelihood function, evaluated at some specific  $\mu$  and at the best-fit value of  $\theta$  for this specific  $\mu$ . The denominator is simply the value of the Likelihood function when both  $\mu$  and  $\theta$  take their best fit values.

Having constructed the Likelihood function that takes into account the luminosity uncertainty, the normalization parameters for each variable can be re-estimated, in order to demonstrate the effect of a systematic uncertainty. By minimizing the PLR from **Equation** 6.7.0.3, the best-fit values were obtained for each variable. From the  $m_{WZ}$  distributions in the ZZ Drell-Yan CR, it was obtained:

$$\mu_{ZZ} = 1.0972 \pm 0.0307 \quad (6.7.0.4)$$

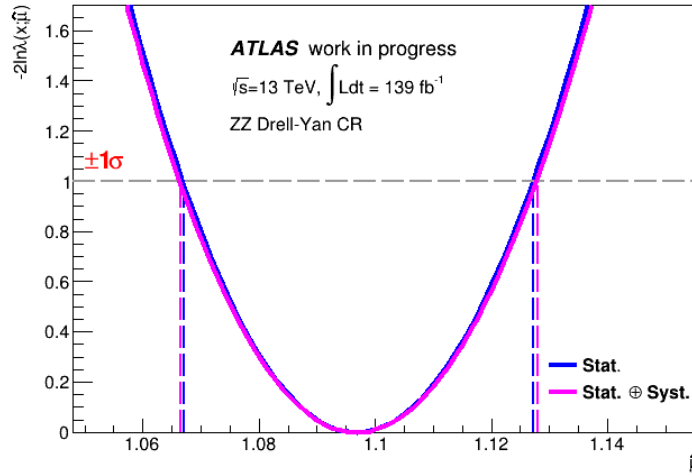


FIGURE 6.7.1:  $\mu_{ZZ}$  PLR ratio estimation using  $m_{WZ}$  as input.

As it evident from **Figure** 6.7.1, in the presence of a systematic uncertainty (purple line), the Likelihood function appears to have bigger spread than in the case of the statistical uncertainty (blue line). This means that the uncertainty in the estimation increases, as it is obvious from **Equation** 6.7.0.4. We can calculate the luminosity uncertainty contribution, by solving the **Equation** 6.7.0.5 with respect to  $\sigma_{lumi}$ :

$$\begin{aligned} \sigma_{total}^2 &= \sigma_{stat}^2 + \sigma_{lumi}^2 \Leftrightarrow \\ \sigma_{lumi} &= \sqrt{\sigma_{total}^2 - \sigma_{stat}^2} \end{aligned} \quad (6.7.0.5)$$

Using **Equation** 6.7.0.5, the contribution of the luminosity is calculated:

$$\mu_{ZZ} = 1.0967 \pm 0.0302 (stat) \pm 0.0062 (lumi) \quad (6.7.0.6)$$

From the  $Sum3Pt$  distributions in the ZZ Drell-Yan CR, it was obtained:

$$\mu_{ZZ} = 1.0967 \pm 0.0302 (stat) \pm 0.0054 (lumi) \quad (6.7.0.7)$$

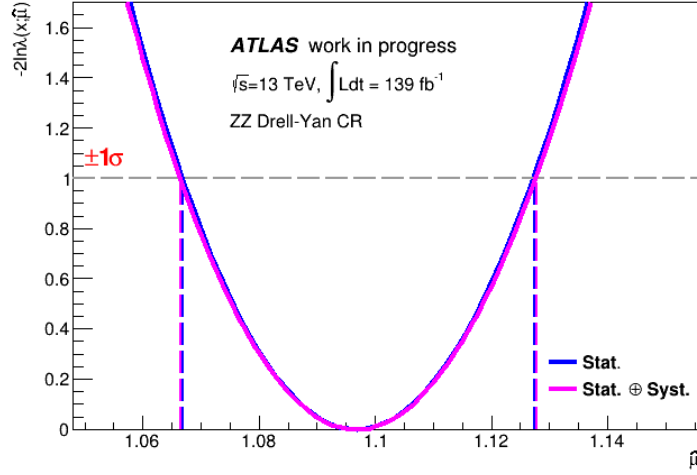


FIGURE 6.7.2:  $\mu_{ZZ}$  PLR ratio estimation using  $Sum3Pt$  as input.

From the  $m_{WZ}^T$  distributions in the ZZ Drell-Yan CR, it was obtained:

$$\mu_{ZZ} = 1.0957 \pm 0.0302 (stat) \pm 0.0049 (lumi) \quad (6.7.0.8)$$

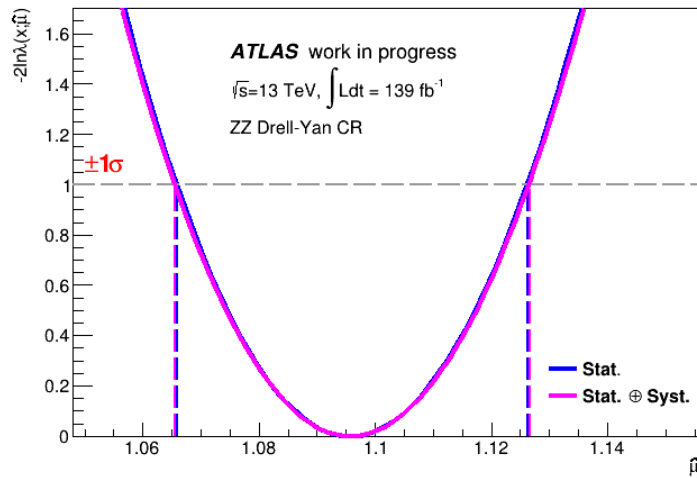


FIGURE 6.7.3:  $\mu_{ZZ}$  PLR ratio estimation using  $m_{WZ}^T$  as input.

The same was done for the normalization factor in the WZ-QCD Drell-Yan CR for each variable. From the  $m_{WZ}$  distributions in the WZ-QCD Drell-Yan CR, it was obtained:

$$\mu_{WZ}^{QCD} = 0.9559 \pm 0.0116 (stat) \pm 0.0051 (lumi) \quad (6.7.0.9)$$

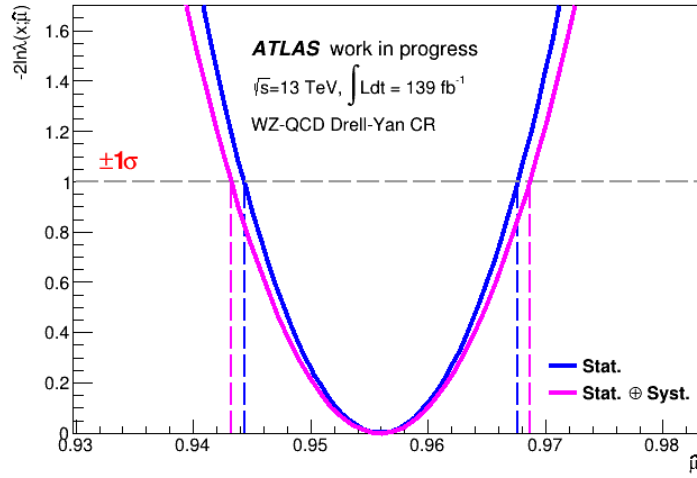


FIGURE 6.7.4:  $\mu_{WZ}^{QCD}$  PLR ratio estimation using  $m_{WZ}$  as input.

From the  $Sum3Pt$  distributions in the WZ-QCD Drell-Yan CR, it was obtained:

$$\mu_{WZ}^{QCD} = 0.9562 \pm 0.0116 (stat) \pm 0.0050 (lumi) \quad (6.7.0.10)$$

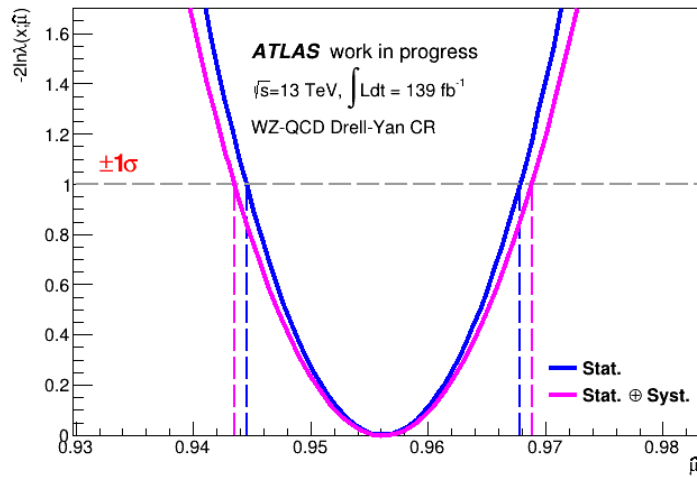


FIGURE 6.7.5:  $\mu_{WZ}^{QCD}$  PLR ratio estimation using  $Sum3Pt$  as input.

From the  $m_{WZ}^T$  distributions in the WZ-QCD Drell-Yan CR, it was obtained:

$$\mu_{WZ}^{QCD} = 0.9556 \pm 0.0116 \text{ (stat)} \pm 0.0044 \text{ (lumi)} \quad (6.7.0.11)$$

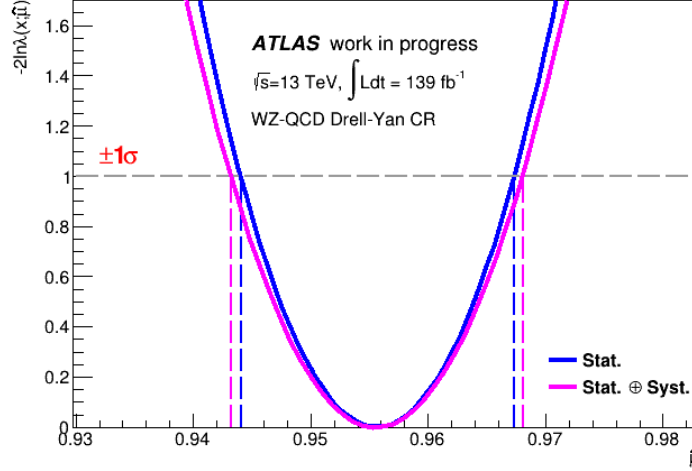


FIGURE 6.7.6:  $\mu_{WZ}^{QCD}$  PLR ratio estimation using  $m_{WZ}^T$  as input.

It should be noted that any other systematic uncertainty that have a Gaussian behaviour, can be described with the method presented in this section.

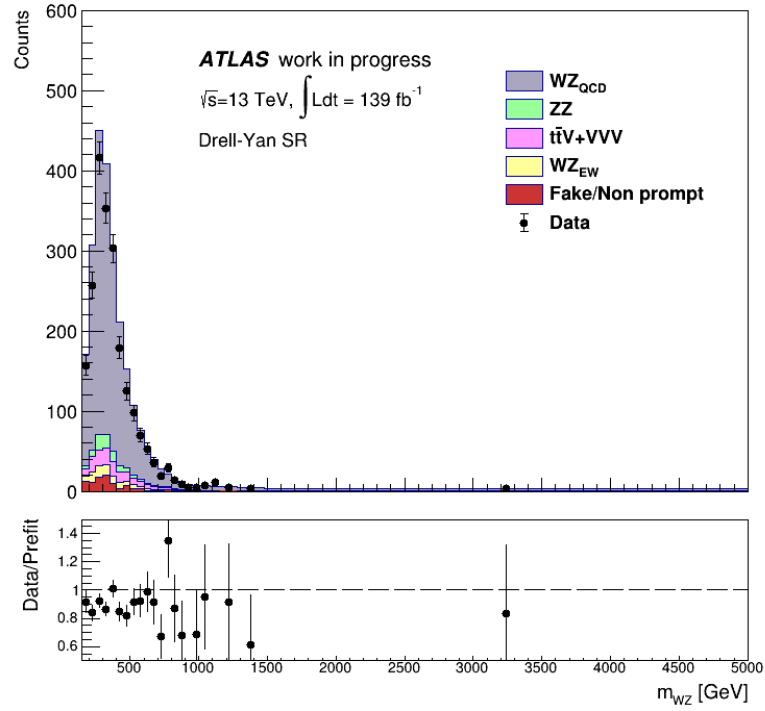
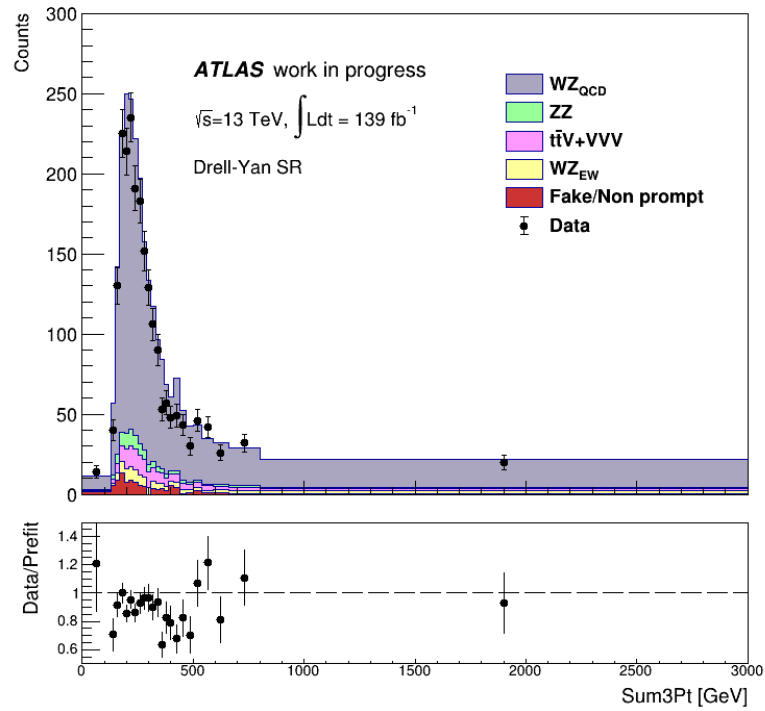
## 6.8 Simultaneous Maximum Likelihood Fit

In this section, a Simultaneous SR/CRs Maximum Likelihood fit is performed. The Likelihood function used to perform the simultaneous fit is in principle the same as the one from **Equation** 6.4.0.1, but takes into account the background distributions from both the ZZ Drell-Yan CR and WZ-QCD Drell-Yan CR, and the Drell-Yan SR. More explicitly:

$$L_{CR+SR}(\mu_{ZZ}, \mu_{WZ}^{QCD}) = L_{ZZ} \cdot L_{WZ-QCD} \cdot L_{SR} \quad (6.8.0.1)$$

In each of these CRs, the parameters of interest are two,  $\mu_{ZZ}$  and  $\mu_{WZ}^{QCD}$ , and scale only the corresponding backgrounds. In the SR, both backgrounds are scaled with their corresponding parameter. No systematic uncertainty is present in this fit. In the following, the pre-fit background distributions are going to be presented, for the variables  $m_{WZ}$ ,  $Sum3Pt$  and  $m_{WZ}^T$ :



FIGURE 6.8.1: Pre-fit  $m_{WZ}$  distribution in the Drell-Yan SR.FIGURE 6.8.2: Pre-fit  $Sum3Pt$  distribution in the Drell-Yan SR.

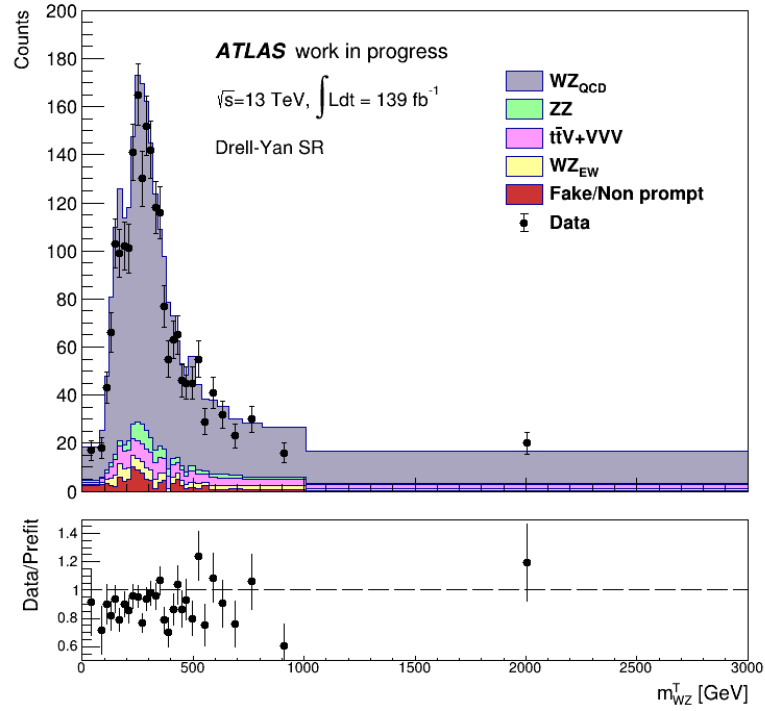


FIGURE 6.8.3: Pre-fit  $m_{WZ}^T$  distribution in the Drell-Yan SR.

After minimizing the Likelihood function from **Equation** 6.8.0.1, from the  $m_{WZ}$  distributions it was obtained:

$$\mu_{ZZ} = 1.0925 \pm 0.0300 \text{ and } \mu_{WZ}^{QCD} = 0.9406 \pm 0.0104 \quad (6.8.0.2)$$

From the  $Sum3Pt$  distributions it was obtained:

$$\mu_{ZZ} = 1.0923 \pm 0.0300 \text{ and } \mu_{WZ}^{QCD} = 0.9409 \pm 0.0104 \quad (6.8.0.3)$$

Finally, from the  $m_{WZ}^T$  distributions it was obtained:

$$\mu_{ZZ} = 1.0915 \pm 0.0300 \text{ and } \mu_{WZ}^{QCD} = 0.9403 \pm 0.0104 \quad (6.8.0.4)$$

As we can see, the results for the normalization factors are very much alike to the ones obtained from the per region fit. Due to the fact the Simultaneous Fit is the nominal process of estimating the normalization factors, in the rest of the analysis, the values presented in this section are going to be used to scale the corresponding backgrounds.

## DRELL-YAN SIGNAL REGION

### 7.1 Drell-Yan Signal Region Distributions

As discussed in **Chapter 5** and presented in **Table 6.2.1**, the definition of the Drell-Yan SR requires the WZ Inclusive criteria to be fulfilled, as well as the extra requirements for PtBalanceW and PtBalanceZ. In the following, the post-fit background distributions are going to be presented, along with a potential HVT signal candidate:

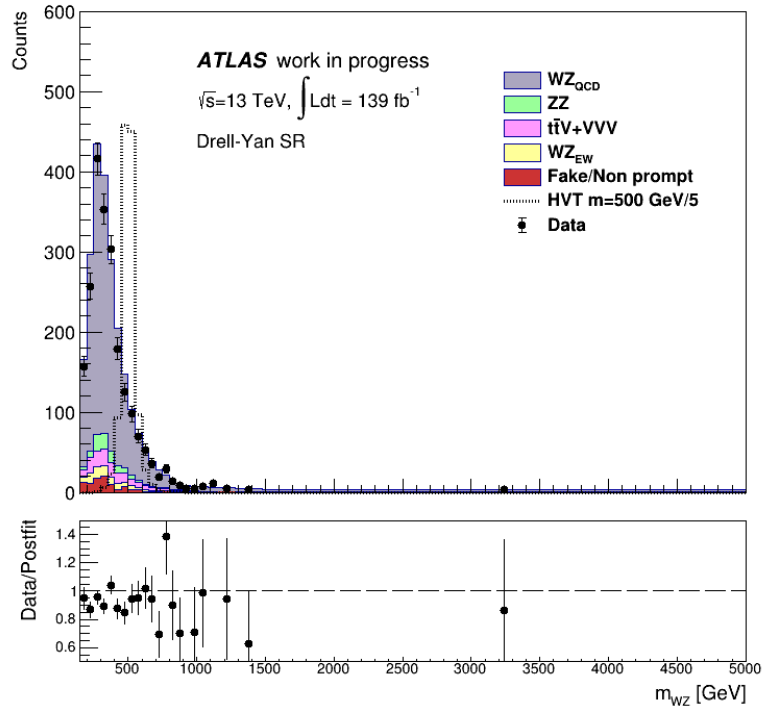
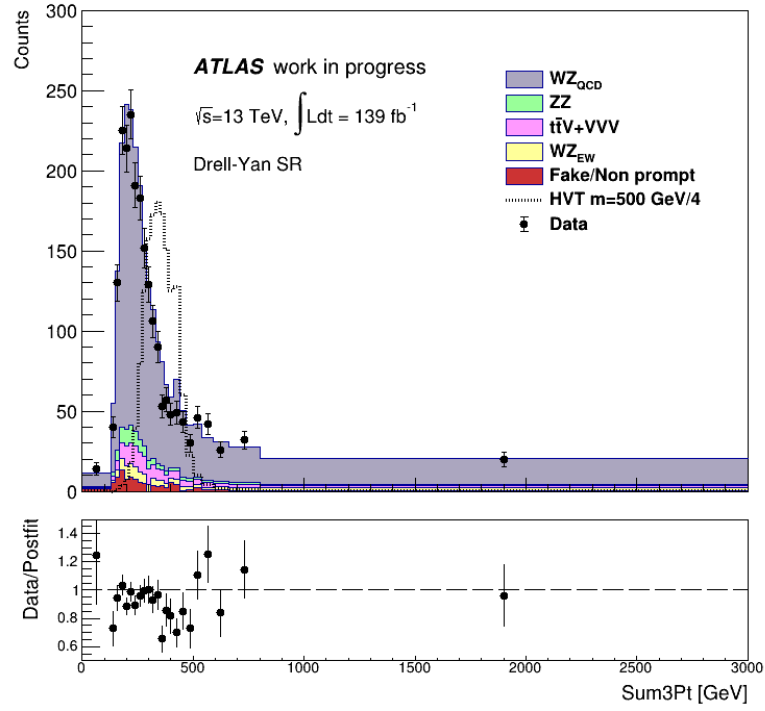
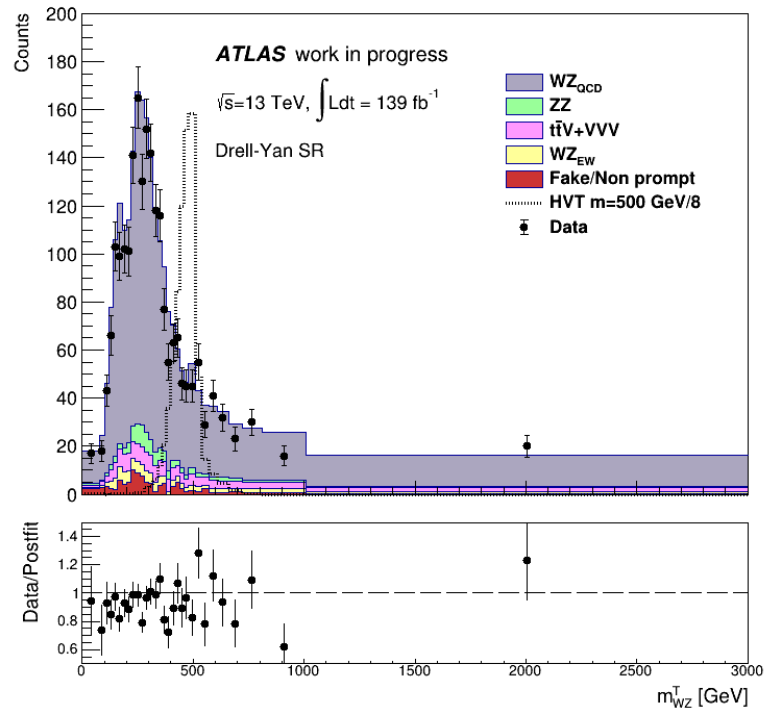


FIGURE 7.1.1: Postfit  $m_{WZ}$  distribution in the Drell-Yan SR.

FIGURE 7.1.2: Postfit  $\text{Sum3Pt}$  distribution in the Drell-Yan SR.FIGURE 7.1.3: Postfit  $m_{WZ}^T$  distribution in the Drell-Yan SR.

## 7.2 Estimating the signal strength parameter

Having constructed the postfit background distributions for each variable, the next step is to fit to the data to the model  $\mu s + b$ , using the same Likelihood function used in **Equation 6.4.0.1**.

In this case, the bin content of the potential HVT candidate distribution stands for the signal events in each bin, whereas the bin contents of all the background distributions stand for the background events in each bin. Our main goal here is to estimate the unknown signal strength parameter  $\mu$ , which will give us a measure of potential signal contribution to our data. After fitting to the data to the signal and background distributions for  $m_{WZ}$ , using the  $W'$  candidate with a mass of 500 GeV , it is obtained:

$$\mu = -0.0059 \pm 0.0031 \quad (7.2.0.1)$$

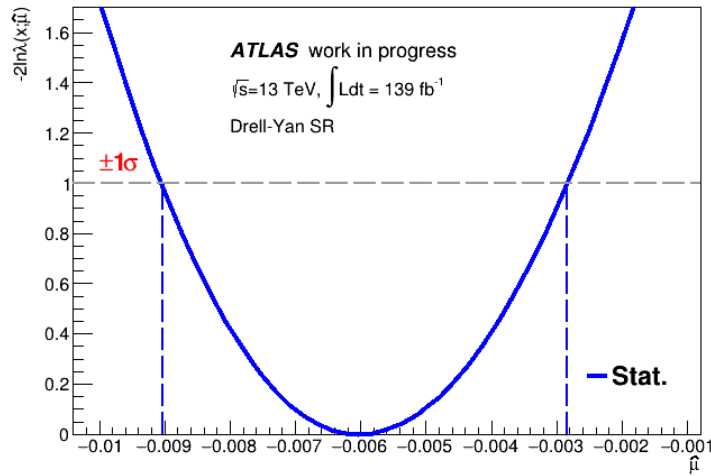


FIGURE 7.2.1: Signal Strength parameter  $\mu$  NLL ratio estimation using  $m_{WZ}$  as input.

After fitting to the data to the signal and background distributions for  $Sum3Pt$ , using the  $W'$  candidate with a mass of 500 GeV , it is obtained:

$$\mu = -0.0204 \pm 0.0048 \quad (7.2.0.2)$$

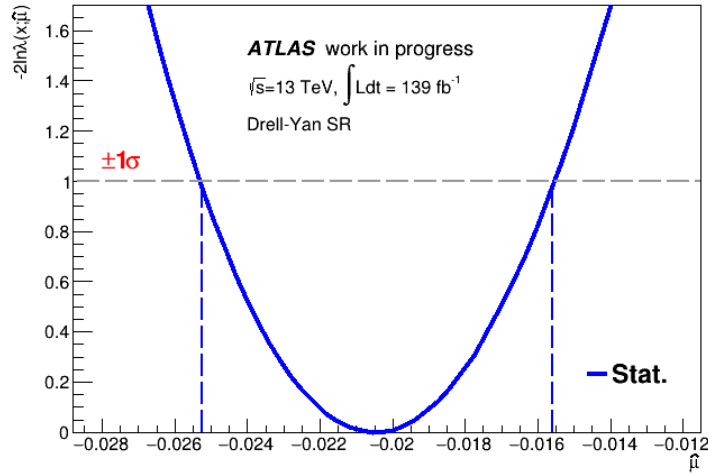


FIGURE 7.2.2: Signal Strength parameter  $\mu$  NLL ratio estimation using  $Sum3Pt$  as input.

Finally, after fitting to the data to the signal and background distributions for  $m_{WZ}^T$ , using the  $W'$  candidate with a mass of 500 GeV , it is obtained:

$$\mu = -0.0040 \pm 0.0031 \quad (7.2.0.3)$$

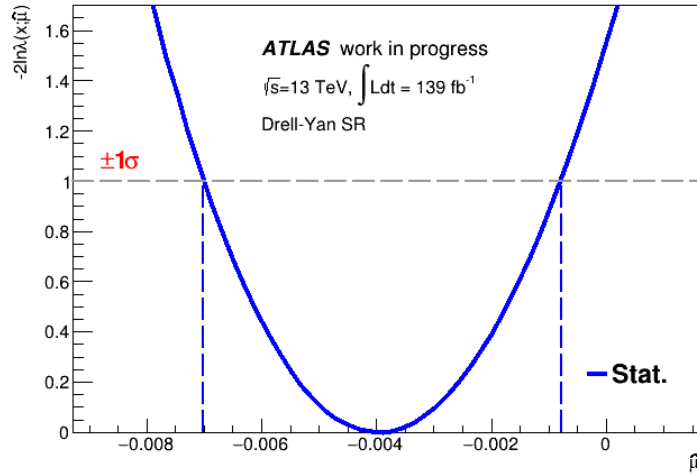


FIGURE 7.2.3: Signal Strength parameter  $\mu$  NLL ratio estimation using  $m_{WZ}^T$  as input.

As it can be seen from the above estimations using the  $W'$  candidate with a mass of 500 GeV, the signal strength parameter seems to be negative and compatible with zero. Such an outcome can be interpreted as a lack of contribution from the 500 GeV to our

data. The same fit was performed for all the  $W'$  candidates used in this analysis. What was found, was that the signal strength parameters estimated, were compatible with zero. Thus, none of the  $W'$  candidates seem to be contributing to our data.

### 7.3 Drell-Yan Signal Region Post-Fit Yields

The fact that there is no contribution from new signal is also evident if the total post-fit expected background events are compared with the actual events observed. In the **Table 7.3.1**, the total expected background events, as well as the total observed events are presented, obtained from the  $m_{WZ}$  distributions:

Backgrounds	Drell-Yan SR Events
WZ-QCD	$1895.96 \pm 8.23$
WZ-EW	$87.68 \pm 0.42$
ZZ	$96.40 \pm 1.08$
$t\bar{t}V + VVV$	$147.05 \pm 0.91$
Fakes	$91.58 \pm 9.26$
Total Expected Background	$2318.68 \pm 12.47$
Total Observed	2155

TABLE 7.3.1: Expected and Observed total post-fit events in the Drell-Yan SR, obtained from the  $m_{WZ}$  distributions.

In the **Table 7.3.2**, the total expected background events, as well as the total observed events are presented, obtained from the  $Sum3Pt$  distributions:

Backgrounds	Drell-Yan SR Events
WZ-QCD	$1896.33 \pm 8.23$
WZ-EW	$87.68 \pm 0.42$
ZZ	$95.59 \pm 1.07$
$t\bar{t}V + VVV$	$147.05 \pm 0.91$
Fakes	$91.58 \pm 9.26$
Total Expected Background	$2318.23 \pm 12.47$
Total Observed	2155

TABLE 7.3.2: Expected and Observed total post-fit events in the Drell-Yan SR, obtained from the  $Sum3Pt$  distributions.

Finally, in the **Table 7.3.3**, the total expected background events, as well as the total observed events are presented, obtained from the  $m_{WZ}^T$  distributions:

Backgrounds	Drell-Yan SR Events
WZ-QCD	$1895.35 \pm 8.23$
WZ-EW	$87.68 \pm 0.42$
ZZ	$95.50 \pm 1.07$
$t\bar{t}V + VVV$	$147.05 \pm 0.91$
Fakes	$91.58 \pm 9.26$
Total Expected Background	$2317.17 \pm 12.47$
Total Observed	2155

TABLE 7.3.3: Expected and Observed total post-fit events in the Drell-Yan SR, obtained from the  $m_{WZ}^T$  distributions.

As it is obvious from the above tables, the expected post-fit background events are compatible with the total observed events, which means that there is no significant contribution to our data, beside the background processes. Thus, there is no discovery of new signal to be made. In the next chapter, will we extract 95% CL upper limits on the production cross section times the branching ratio for  $W'$  candidates of different masses.

The reason that justifies the usage of this statistical process is that since there is no discovery to be made, there is still useful information to extract for the model. In particular, by extracting limits we want to exclude as many values of the parameter space as possible, based on the data. In the present thesis, the parameter space corresponds to the values of the resonance's mass.



## STATISTICAL METHODS FOR UPPER LIMITS

### 8.1 Definition of a statistical test

In particle physics, the most common way to search for a new, yet unknown process, is via the definition of a statistical test. Let's assume that one is trying to discover a new signal process. Then they must define two separate hypotheses. The null hypothesis, often denoted as  $H_0$ , as described in [15], is usually constructed to be the that of the status quo, which means what was always assumed. The null hypothesis is then tested against the alternative hypothesis, often denoted as  $H_1$ . When setting limits, the model with signal plus background plays the role of  $H_0$ , which is tested against the background only hypothesis,  $H_1$ . The compatibility between the data and a certain hypothesis is determined via the so called p-value, which gives the probability of observing data of equal or greater incompatibility with the predictions of the tested hypothesis.

In particle physics, it is also very convenient to convert the p-value into an equivalent significance,  $Z$ , defined such that a Gaussian distributed variable found  $Z$  standard deviations above its mean, has an upper-tail probability equal to  $p$ . These two values are connected via:

$$Z = \Phi^{-1}(1 - p) \quad (8.1.0.1)$$

In **Equation** 8.1.0.1, the function  $\Phi^{-1}$  stands for the inverse cumulative distribution of a standard Gaussian distributed random variable. For a signal process such as the Higgs boson, we tend to reject the background hypothesis with a significance of at least  $Z = 5$  as an appropriate level to constitute a discovery, which corresponds to  $p = 2.87 \times 10^{-7}$ . For purposes of excluding a signal hypothesis, a threshold p-value

of 0.05 (95% confidence level) is often used, which corresponds to  $Z = 1.64$ . The most common way to establish discovery or exclusion, is via using the likelihood ratio as a test statistic. Let's now consider an experiment, where we can measure the values of some kinematic variables, and store them in histograms with  $N$  bins, where the bin content of each bin is assumed to be  $\mathbf{n} = (n_1, n_2, \dots, n_N)$ . The expectation value of  $n_i$  can be written as:

$$E[n_i] = \mu s_i + b_i \quad (8.1.0.2)$$

In **Equation 8.1.0.2**, the parameter  $\mu$  stands for the signal strength parameters, which separates the two hypotheses. The value  $\mu = 0$  corresponds to the background only hypothesis, while the value  $\mu = 1$  corresponds to the nominal signal hypothesis. We often write  $\mu = \sigma/\sigma_{SM}$ , where  $\sigma_{SM}$  is the SM production cross section.

The best one-dimensional test-statistic (in the sense of maximum power and due to its known asymptotic properties) for investigating a hypothesized value of  $\mu$  is the profile likelihood ratio:

$$\lambda(\mu, \boldsymbol{\theta}) = \frac{L(\mu, \hat{\hat{\boldsymbol{\theta}}})}{L(\hat{\mu}, \hat{\hat{\boldsymbol{\theta}}})} \quad (8.1.0.3)$$

In **Equation 8.1.0.3**, the parameters  $\boldsymbol{\theta}$  denote the systematic uncertainties that are described as nuisance parameters. In this analysis, systematic uncertainties are not taken into account for the extraction of limits, and thus, the test statistic used will be the likelihood ratio:

$$\lambda(\mu) = \frac{L(\mu)}{L(\hat{\mu})} \quad (8.1.0.4)$$

The Likelihood function used is the one from **Equation 6.4.0.1**. If we assume that the presence of a new signal will only increase the mean event rate beyond what is expected from background alone, the signal process must yield  $\hat{\mu} > 0$ . If it is found that  $\hat{\mu} < 0$ , then it is assumed that the data are compatible with the background only hypothesis, and thus  $\mu = 0$ . Hence, a modified likelihood ratio test statistic is defined:

$$\tilde{\lambda}(\mu) = \begin{cases} \frac{L(\mu)}{L(\hat{\mu})}, & \hat{\mu} \geq 0 \\ \frac{L(\mu)}{L(0)}, & \hat{\mu} < 0 \end{cases} \quad (8.1.0.5)$$

## 8.2 Test Statistic for upper limits

As we have seen in the previous chapter, our data seem to be compatible with the null hypothesis, which means that there is no discovery to be made. However, we can

still extract useful information from our data and extract the 95% CL upper limits. According to [8], two test statistic are considered for this purpose. The first one is expressed as:

$$q(\mu) = \begin{cases} -2 \ln \lambda(\mu), & \hat{\mu} \leq \mu \\ 0, & \hat{\mu} > \mu \end{cases} \quad (8.2.0.1)$$

In **Equation 8.2.0.1**,  $\lambda(\mu)$  stands for the likelihood ratio, as defined in **Equation 8.1.0.4**. The alternative test statistic used is expressed as:

$$\tilde{q}(\mu) = \begin{cases} -2 \ln \tilde{\lambda}(\mu), & \hat{\mu} \leq \mu \\ 0, & \hat{\mu} > \mu \end{cases} = \begin{cases} -2 \ln \frac{L(\mu)}{L(0)}, & \hat{\mu} < 0 \\ -2 \ln \frac{L(\mu)}{L(\hat{\mu})}, & 0 \leq \hat{\mu} \leq \mu \\ 0, & \hat{\mu} > \mu \end{cases} \quad (8.2.0.2)$$

It has been found in numerical examples that the difference between the two test statistics is negligible. Thus, the test statistic defined in **Equation 8.2.0.2** will be used in the rest of the analysis. What we are interested in is the p-value associated with this test statistic, which will be:

$$p_\mu = \int_{\tilde{q}_{obs}}^{\infty} f(\tilde{q}_\mu | \mu) d\tilde{q}_\mu \quad (8.2.0.3)$$

As it can be seen from **Equation 8.2.0.3**, the p-value depends on the tested value of  $\mu$ . The value of  $\mu$  that fulfills the requirement  $p_\mu = 0.05$ , corresponds to the 95% upper limit on  $\mu$ . Of course, in order to calculate this p-value, we need the pdf of the test statistic. In the next section, the asymptotic approximations that will lead to the approximate calculation of the pdf  $f(\tilde{q}_\mu | \mu)$  will be presented.

### 8.3 Asymptotic Approximations

According to the work of Wald in [20], the exact form of the PLR, with a single parameter of interest, is predicted for a large dataset of size  $N$ :

$$-2 \ln \lambda(\mu) = \frac{(\mu - \hat{\mu})^2}{\sigma^2} + \mathcal{O}(1/\sqrt{N}) \quad (8.3.0.1)$$

In **Equation 8.3.0.1**, the Maximum Likelihood estimator  $\hat{\mu}$  is assumed to follow a Gaussian distribution, with a mean of  $\mu'$  and a standard deviation of  $\sigma$ . The standard deviation of the Maximum Likelihood estimator is a very useful quantity, and its calculation will be shown later in this chapter, via the help of the Asimov dataset. Assuming the

validity of the Wald approximation, the distribution of  $\tilde{q}_\mu$  is calculated as follows:

$$\tilde{q}(\mu) = \begin{cases} \frac{\mu^2}{\sigma^2} - \frac{2\mu\hat{\mu}}{\sigma^2}, & \hat{\mu} < 0 \\ \frac{(\mu - \hat{\mu})^2}{\sigma^2}, & 0 \leq \hat{\mu} \leq \mu \\ 0, & \hat{\mu} > \mu \end{cases} \quad (8.3.0.2)$$

The distribution function is found to be:

$$\begin{aligned} f(\tilde{q}_\mu|\mu) &= \Phi\left(\frac{\mu' - \mu}{\sigma}\right) \delta(\tilde{q}_\mu) \\ &+ \begin{cases} \frac{1}{2} \frac{1}{\sqrt{2\pi}} \exp\left[-\frac{1}{2} \left(\sqrt{\tilde{q}_\mu} - \frac{\mu - \mu'}{\sigma}\right)^2\right], & 0 < \tilde{q}_\mu \leq \mu^2/\sigma^2 \\ \frac{1}{\sqrt{2\pi}(2\mu/\sigma)} \exp\left[-\frac{1}{2} \frac{(\tilde{q}_\mu - (\mu^2 - 2\mu\mu')/\sigma^2)^2}{(2\mu/\sigma^2)}\right], & \tilde{q}_\mu > \mu^2/\sigma^2 \end{cases} \end{aligned} \quad (8.3.0.3)$$

The corresponding cumulative distribution is found to be:

$$F(\tilde{q}_\mu|\mu) = \begin{cases} \Phi\left(\sqrt{\tilde{q}_\mu} - \frac{\mu - \mu'}{\sigma}\right), & 0 < \tilde{q}_\mu \leq \mu^2/\sigma^2 \\ \Phi\left(\frac{\tilde{q}_\mu + \mu^2/\sigma^2}{2\mu/\sigma}\right), & \tilde{q}_\mu > \mu^2/\sigma^2 \end{cases} \quad (8.3.0.4)$$

The p-value associated with the hypothesized  $\mu$  is found from:

$$p_\mu = 1 - F(\tilde{q}_\mu|\mu) \quad (8.3.0.5)$$

In **Equation** 8.3.0.4,  $\Phi$  stands for the standard Gaussian cumulative distribution. Also, as it is obvious from **Equation** 8.3.0.5, the p-value is a function of the tested  $\mu$ . The value of  $\mu$  that satisfies  $p_\mu = 0.05$  is reported as the 95% CL upper limit on the signal strength parameter.

## 8.4 The Asimov dataset and the variance of $\hat{\mu}$

Some of the formulae given require the knowledge of  $\sigma$ , which is the standard deviation of the  $\hat{\mu}$  estimator, if it is assumed that it follows a Gaussian distribution with a mean of  $\mu'$  and a standard deviation of  $\sigma$ . In order to calculate  $\sigma$ , one has to define an artificial dataset, known as the Asimov dataset. The Asimov dataset is defined as an artificial dataset where all the parameters are fixed to their expected values. Therefore, when setting limits, the Asimov dataset coincides with the background prediction. In other words, if the Asimov data are fitted to the  $\mu s + b$  model via the Likelihood function of

**Equation 6.4.0.1**, then  $\hat{\mu}$  should be equal to  $\mu'$ , where  $\mu'$  corresponds to the value of the strength parameter associated with the Asimov dataset. Since the Asimov dataset coincides with the background prediction,  $\mu' = 0$ , but its value will not be substituted for the purpose of generality.

In order to calculate  $\sigma$ , **Equation 8.3.0.1** is going to be used. Because the Asimov data set corresponds to a strength parameter  $\mu'$ , then  $\hat{\mu} = \mu'$ . Therefore, it can be written that:

$$-2 \ln \lambda_A \approx \frac{(\mu - \mu')^2}{\sigma^2} \quad (8.4.0.1)$$

The left hand side of the equation corresponds to the  $\tilde{q}_{\mu,A}$  test statistic, where A stands for Asimov. Therefore, it can be written that:

$$\sigma^2 = \frac{(\mu - \mu')^2}{\tilde{q}_{\mu,A}} \quad (8.4.0.2)$$

As it is obvious from **Equation 8.4.0.2**,  $\sigma$  is a function of the tested value of  $\mu$ , which is inserted in the numerator. Also, it must be noted that in order to calculate  $\tilde{q}_{\mu,A}$ , the  $\mu$  inserted in the formula again corresponds to the tested value of  $\mu$ , while the value of  $\hat{\mu}$  corresponds to the Maximum Likelihood estimator obtained from fitting the Asimov dataset to the  $\mu s + b$  model.

## 8.5 The $CL_s$ method

In Particle Physics,  $CL_s$  represents a statistical method for setting upper limits, also called exclusion limits, on model parameters. It was first introduced by physicists working at the LEP experiment at CERN and has since been used by many high energy physics experiments.

Let's now consider a background dominated experiment and let's suppose one is trying to perform a statistical test of size  $\alpha$  between the null hypothesis, which is the signal plus background hypothesis, against the alternative hypothesis, which is the background only hypothesis. By construction, one may reject the null hypothesis  $\alpha\%$  of the times, without having sensitivity to it. This is the case when one searches for a new heavy boson with a mass so high that its production rate in a given experiment is negligible. Although the sensitivity to a model might be very low, it should not be excluded. This issue was addressed via the  $CL_s$  method [17]. The procedure is

based on a test statistic called  $CL_s$ , which is defined as:

$$CL_s = \frac{p_\mu}{1 - p_b} = \frac{CL_{s+b}}{CL_b} \quad (8.5.0.1)$$

In **Equation 8.5.0.1**, the corresponding p-values are computed from the above formulas:

$$p_\mu = 1 - F(\tilde{q}_\mu | \mu) \quad (8.5.0.2)$$

$$p_b = F(\tilde{q}_\mu | \mu) \quad (8.5.0.3)$$

The definition of those two p-values is better illustrated in **Figure 8.5.1**. In the following subsections we will clarify how to compute the p-values correctly.

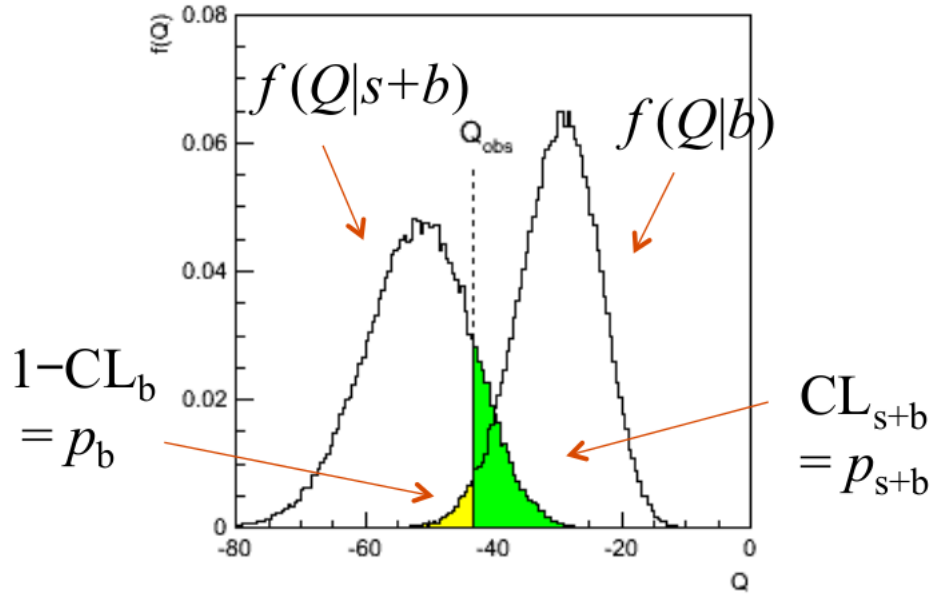


FIGURE 8.5.1: Demonstration of the p-values associated with the signal plus background hypothesis and the background only hypothesis.

### 8.5.1 Observed Limits

In order to report a 95% CL **observed** upper limit, the condition that must be satisfied is that  $CL_{s,obs} = 0.05$ . To compute the test statistic, some steps must be followed:

- $\sigma$  is calculated according to **Equation 8.4.0.2**
- For a tested value of  $\mu$ , the value of  $\tilde{q}_\mu$  is calculated by fitting the **observed data** to the  $\mu s + b$  model, in order to extract  $\hat{\mu}$

- $p_\mu$  is calculated via **Equation 8.5.0.2**, by plugging the value of the test statistic in **Equation 8.3.0.4**, and by setting  $\mu' = \mu$ . This happens because when testing the hypothesis associated with a tested value of  $\mu$ ,  $\hat{\mu}$  will be centered around  $\mu$ .
- $p_b$  is calculated via **Equation 8.5.0.3**, by plugging the value of the test statistic in **Equation 8.3.0.4**, and by setting  $\mu' = 0$ . This happens because when testing the background hypothesis,  $\hat{\mu}$  will be centered around 0.
- Having calculated  $p_\mu$  and  $p_b$ , the test statistic  $CL_{s,obs}$  can be calculated for a tested value of  $\mu$

This sequence is repeated until  $CL_{s,obs} = 0.05$ . The value of the tested  $\mu$  that satisfies this condition, is reported as the 95% CL **observed** upper limit on the signal strength parameter.

## 8.5.2 Expected Limits

In order to report a 95% CL **expected** upper limit, the condition that must be satisfied is that  $CL_{s,exp} = 0.05$ . To compute the test statistic, some steps must be followed:

- $\sigma$  is calculated according to **Equation 8.4.0.2**
- For a tested value of  $\mu$ , the value of  $\tilde{q}_\mu$  is calculated by fitting the **Asimov data** to the  $\mu s + b$  model, in order to extract  $\hat{\mu}$
- $p_\mu$  is calculated via **Equation 8.5.0.2**, by plugging the value of the test statistic in **Equation 8.3.0.4**, and by setting  $\mu' = \mu$ . This happens because when testing the hypothesis associated with a tested value of  $\mu$ ,  $\hat{\mu}$  will be centered around  $\mu$ .
- $p_b$  is calculated via **Equation 8.5.0.3**, by plugging the value of the test statistic in **Equation 8.3.0.4**, and by setting  $\mu' = 0$ . This happens because when testing the background hypothesis,  $\hat{\mu}$  will be centered around 0.
- Having calculated  $p_\mu$  and  $p_b$ , the test statistic  $CL_{s,exp}$  can be calculated for a tested value of  $\mu$

This sequence is repeated until  $CL_{s,exp} = 0.05$ . The value of the tested  $\mu$  that satisfies this condition, is reported as the 95% CL **expected** upper limit on the signal strength

parameter. When setting expected limits, it also crucial to calculate the  $\pm 1\sigma$  and  $\pm 2\sigma$  error bands. The formula used for the  $N\sigma$  bands in this analysis is the following [4]:

$$\mu_{up+N} = \sigma [\Phi^{-1}(1 - 0.05\Phi(N)) + N] \quad (8.5.2.1)$$

By substituting  $N = \pm 1, \pm 2$ , one can get the corresponding 95% CL error bands.



## RESULTS

In this chapter, the 95% observed and expected limits on the production cross section multiplied by the branching fraction for the signal selection in the Drell-Yan SR are going to be presented, for three different variables, and for two variables simultaneously. The  $W'$  mass candidates that were used in the extraction of the limits, as well as their production cross sections are presented in **Appendix A**. The observed and upper limits on the cross section are calculated from:

$$\sigma_{up,obs/exp} = s \cdot \mu_{up,obs/exp} \cdot \sigma_{MC} \quad (9.0.0.1)$$

In **Equation 9.0.0.1**,  $s$  stands for a scaling factor, which is equal  $1/(0.3257 \cdot 0.10099)$  and accounts for the fiducial volume of the detector. Also, a comparison between the observed and expected limits extracted for the three different variables is going to be presented.

### 9.1 Limits

By utilizing the  $CL_s$  method described in the previous chapter, 95% CL upper limits on the cross section multiplied by the branching fraction were extracted using  $m_{WZ}$ ,  $Sum3Pt$  and  $m_{WZ}^T$  as input variables. **Figure 9.1.1** shows the limits obtained from the  $m_{WZ}$  distributions:

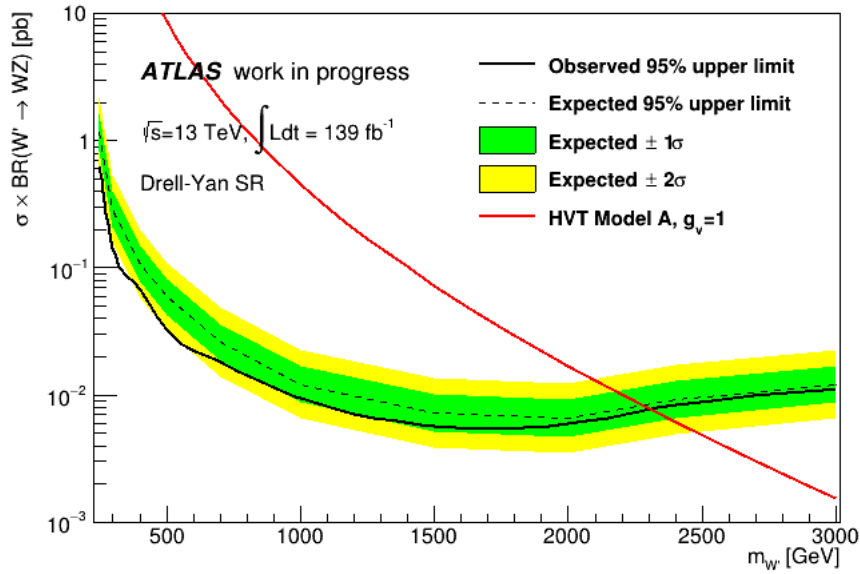


FIGURE 9.1.1: Observed and expected limits on the cross section multiplied by the branching fraction, using  $m_{WZ}$  as input.

The information that can be extracted from **Figure 9.1.1** is that masses below 2300 GeV can be excluded.

The reader can comprehend the previous sentence using the following thought pattern: The observed upper limit on the cross section times the branching ratio which corresponds to a specific mass is obtained by scaling the corresponding cross section with the upper limit on  $\mu$ .

The p-value that corresponds to the the upper limit on  $\mu$  is 0.05. From the statistical theory on upper limits, we know that higher values of  $\mu$  correspond to lower p-values. Thus, any higher value of  $\mu$  would correspond to p-values lower than 0.05 and therefore can be excluded. For more information on hypothesis testing, the reader is advised to read **Appendix B**.

The red line in **Figure 9.1.1** describes the nominal values for the cross sections of each mass. Thus, these values correspond to  $\mu = 1$ . As a matter of fact, resonance masses that have nominal cross sections higher than the corresponding observed limit, correspond to higher  $\mu$  values, and therefore can be excluded by data.

**Figure 9.1.2** shows the limits obtained from the *Sum3Pt* distributions:

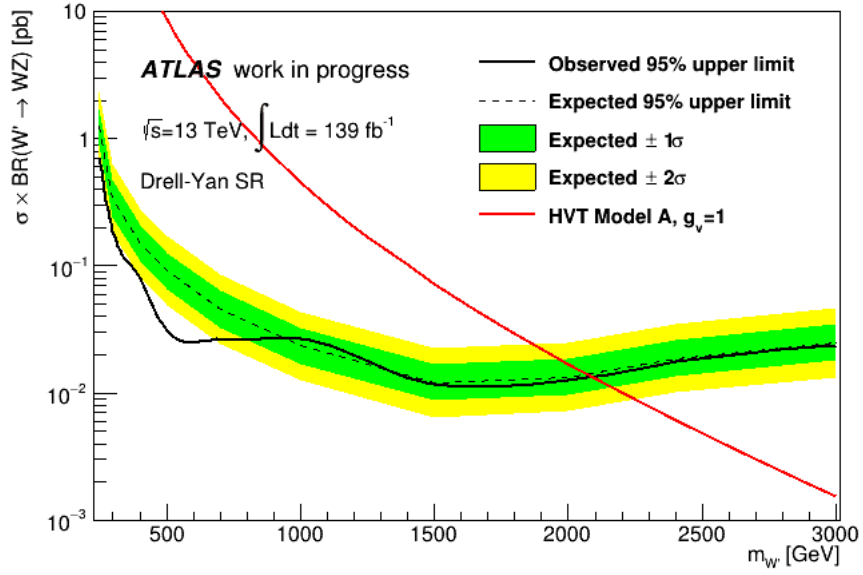


FIGURE 9.1.2: Observed and expected limits on the cross section multiplied by the branching fraction, using *Sum3Pt* as input.

The information that can be extracted from **Figure 9.1.2** is that masses below 2100 GeV can be excluded. Finally, **Figure 9.1.3** shows the limits obtained from the  $m_{WZ}^T$  distributions:

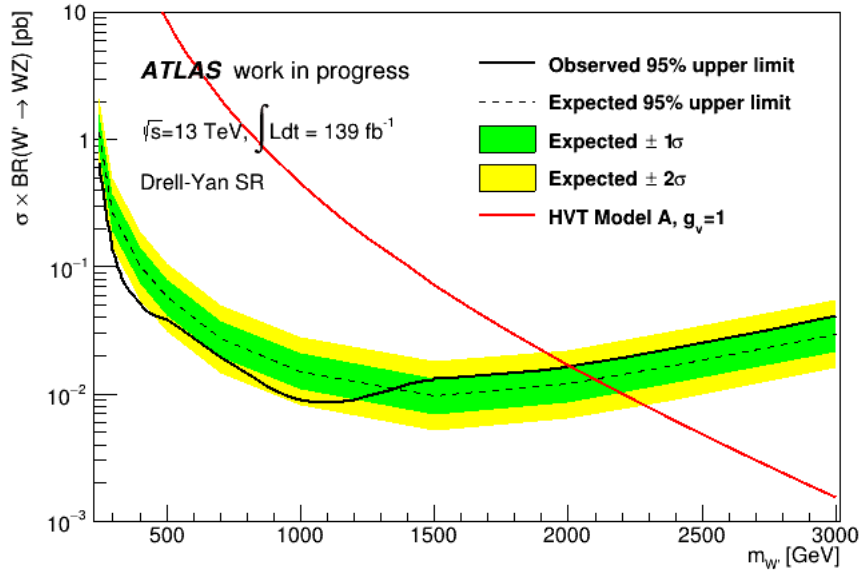


FIGURE 9.1.3: Observed and expected limits on the cross section multiplied by the branching fraction, using  $m_{WZ}^T$  as input.

The information that can be extracted from **Figure 9.1.3** is that masses below 2000 GeV can be excluded.

Limits were also extracted using two variables simultaneously. Of course, that would require that the correlation between them is low. The lowest correlation in the Drell-Yan SR was found between the invariant mass of the three leptons,  $m_{3l}$  and the transverse momentum magnitude of the three leptons,  $p_{3l}^T$ :

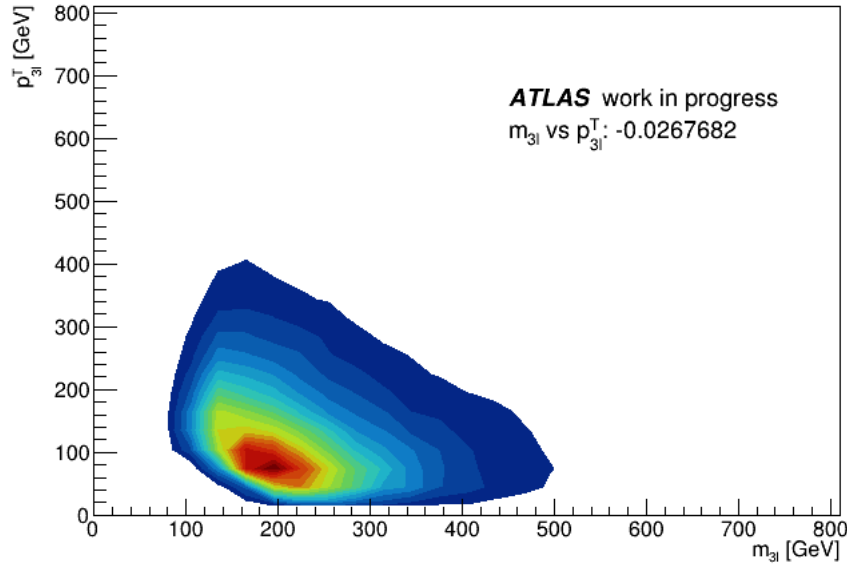


FIGURE 9.1.4: Correlation plot between  $m_{3l}$  and  $p_{3l}^T$ .

The 95% CL upper limits for two variables were extracted using the method of **unrolling**. By "unrolling" the 2D distributions for all the background processes and for all the signal candidates, one can create 1D distributions, which then are treated with the  $CL_s$  method.

In order to implement the method of unrolling correctly, one has to follow some steps. First of all, the 2D distributions for all the backgrounds and the signal candidates have to be constructed. Here, we have used 4 bins in the x-axis for  $m_{3l}$  and 4 bins in the y-axis for  $p_{3l}^T$ . The bins of the final 1D distributions will be  $4 \cdot 4 = 16$ .

Next, through a nested loop, one has to go through every single bin in the 2D distributions and retrieve the bin content, which will be kept and used later. That means that the loop will go through the bin contents  $4 \cdot 4 = 16$  times, keeping 16 values stored.

Finally, the bins of the 1D distribution are constructed to be equidistant from 0 to 16. The bin content of each bin is set to be equal to the corresponding value kept in the

previous step, which means the first bin content is set to the first value and so on. The unrolled distributions are shown in **Figure 9.1.5**:

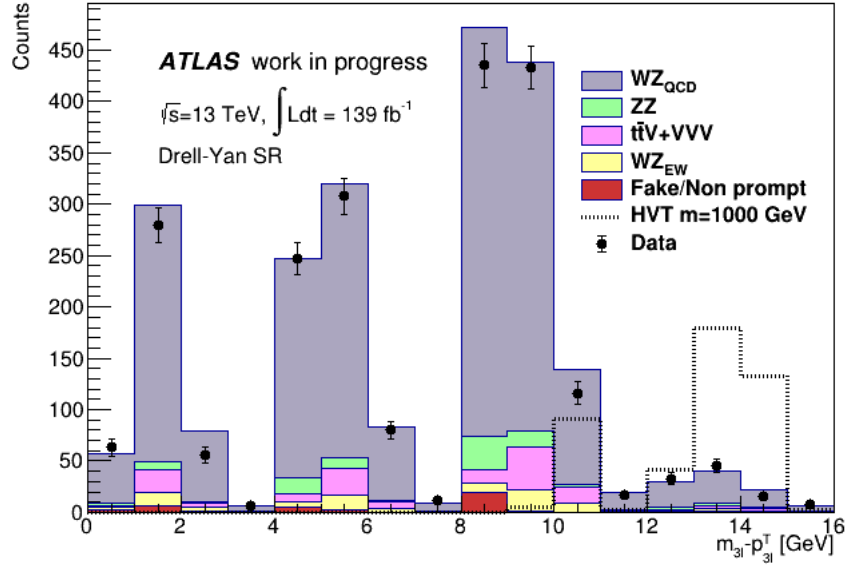


FIGURE 9.1.5: Unrolled distributions obtained from  $m_{3l}$  and  $p_{3l}^T$ .

After the unrolling of the 2D distributions, the 1D distributions are used as input, and 95% CL upper limits are extracted using the method  $CL_s$  described in the previous chapter. **Figure 9.1.6**, shows the limits obtained from the  $m_{3l}$  and  $p_{3l}^T$  distributions:

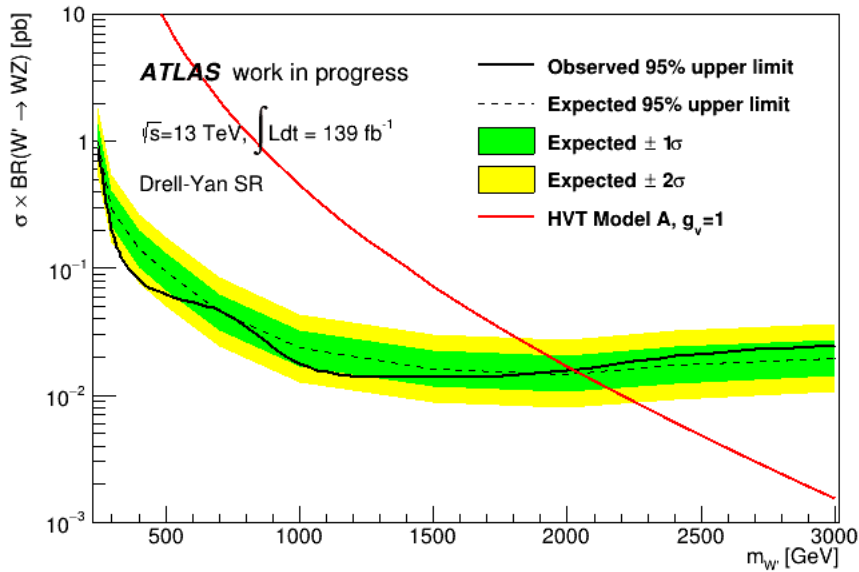


FIGURE 9.1.6: Observed and expected limits on the cross section multiplied by the branching fraction, using  $m_{3l}$  and  $p_{3l}^T$  as input.

The information that can be extracted from **Figure 9.1.6** is that masses below 2000 GeV can be excluded.

## 9.2 Observed and expected limits comparison

**Figures 9.2.1** and **9.2.2**, show the comparison of the observed and expected limits respectively:

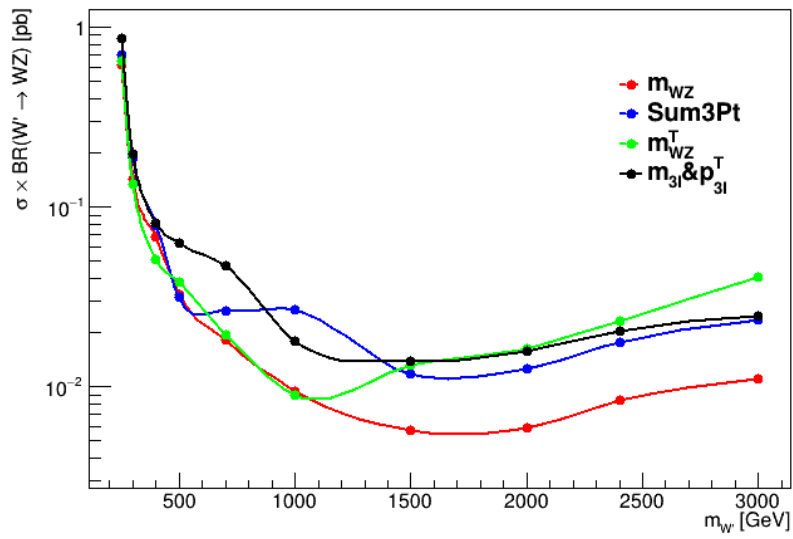


FIGURE 9.2.1: Observed limits comparison for different variables in the Drell-Yan SR.

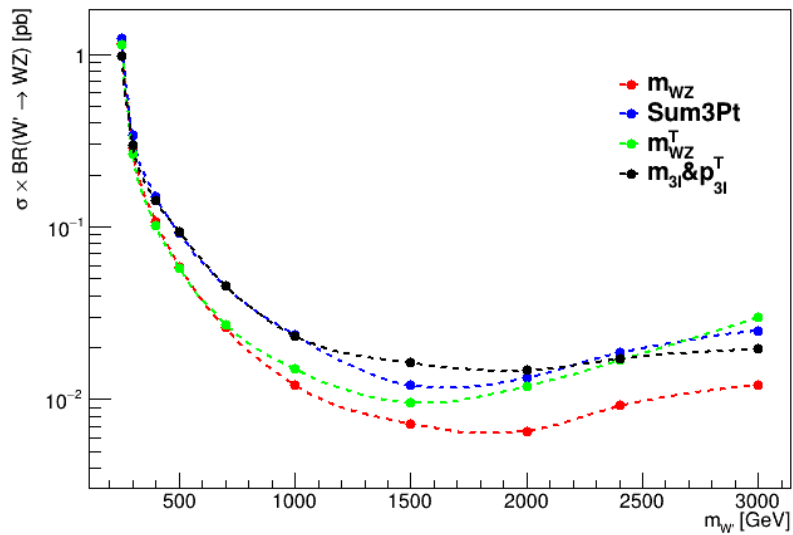


FIGURE 9.2.2: Expected limits comparison for different variables in the Drell-Yan SR.

From **Figure 9.2.1** we can see that although in general  $m_{WZ}$  seems to be the best for setting stricter limits, for masses below around 500 GeV, all the variables give almost equivalent results. Also,  $m_{WZ}^T$  seems to be producing stricter limits than  $Sum3Pt$  in the mass range 500 – 1500 GeV, while  $Sum3Pt$  gives stricter limits  $m_{WZ}^T$  and  $m_{3l}$  &  $p_{3l}^T$  in the mass range 1500 – 3000 GeV. Finally,  $m_{3l}$  &  $p_{3l}^T$  seem to be producing stricter limits than  $m_{WZ}^T$  in the mass range 2000 – 3000 GeV.

From **Figure 9.2.2** we can see that although in general  $m_{WZ}$  seems to be the best for setting stricter limits, for masses below around 300 GeV, all the variables give almost equivalent results. Also,  $m_{WZ}^T$  seems to be producing stricter limits than  $Sum3Pt$  in the mass range 400 – 2500 GeV. Finally,  $m_{3l}$  &  $p_{3l}^T$  seem to be producing stricter limits than  $Sum3Pt$  and  $m_{WZ}^T$  in the mass range 2500 – 3000 GeV.

## CONCLUSIONS

Up until today, Standard Model is the most successful theory in interpreting the obtained experimental data. However, it is not a complete theory. This fact has given rise to many beyond Standard Model theories. In the present thesis, we studied the theory of Heavy Vector Triplets, which predicts a spin-1  $W'$ . More specifically, we studied the resonant WZ diboson production, using data obtained from the ATLAS detector at LHC, at an integrated luminosity of  $139 fb^{-1}$  and a center of mass energy of 13 TeV. The channel studied was the  $W' \rightarrow WZ \rightarrow lvll$ , where  $l = e, \mu$ , considering the Drell-Yan process (quark - antiquark fusion).

As it was stated in the end of Chapter 7, no significant deviation from the Standard Model is observed. However, the analysis performed in this this thesis is carried out without the use of any standard analysis tools and relies purely on personal code. For this reason, not all the factors that impact the analysis have been taken into account, for example theoretical uncertainties. Thus, the analysis carried out in this thesis is far from complete and there is plenty of room for improvement. Also, the LHC now targets to achieve higher luminosity in order to increase the available statistics. As a matter of fact the probability of observing new signal contributions, that might lead us to New Physics is enhanced.



**SIGNAL MONTE CARLO SAMPLES**

All the information about the signal MC samples used in the analysis is in **Table A.0.1**.

<b>DSID</b>	<b>Mass</b>	<b>Cross Section [fb]</b>	<b>k-factor</b>
307376	250	4110	1.0
307377	300	2260	1.0
307378	400	717	1.0
302266	500	283.9	1.0
302268	700	69.23	1.0
302271	1000	15.09	1.0
302276	1500	2.391	1.0
302281	2000	0.5610	1.0
302283	2400	0.2028	1.0
302286	3000	0.05036	1.0

TABLE A.0.1: Summary of the HVT signal samples used in the analysis.

## HYPOTHESIS TESTING

The goal of a statistical test is to make a statement about how well the observed data with a certain hypothesis. The hypothesis under consideration is the null hypothesis, denoted as  $H_0$ . This is to be tested against the alternative hypothesis, denoted as  $H_1$  [7].

In order to investigate the measure of agreement between the observed data and a given hypothesis, one constructs a function of the measured variables called a test statistic  $t(x)$ . Each of the hypotheses will imply a given pdf for the test statistic, for example  $g(t|H_0)$  and  $g(t|H_1)$ .

Often one formulates the statement about the compatibility between the data and the various hypotheses in terms of a decision to accept or reject a given null hypothesis. This is done by defining a critical region for  $t(x)$ . The critical region is defined such that, under the null hypothesis, the probability for  $t(x)$  to be observed there is some value  $\alpha$ , which is called **significance level**, or **size** of the test. Let's suppose we define a value of the test statistic, which will be called cut or decision boundary, denoted as  $t_{cut}$ . The significance level is defined as:

$$\alpha = \int_{t_{cut}}^{\infty} g(t|H_0) dt$$

According to the definition of the decision boundary, one would accept the null hypothesis if the observed value of the test statistic is less than  $t_{cut}$ . This also gives rise to another probability, of observing a value of the test statistic greater than  $t_{cut}$  under the null hypothesis, and therefore rejecting the null hypothesis when it is true. This called **error of first kind**. Correspondingly, there is a probability of accepting the null hypothesis, while the alternative hypothesis is true. . This called **error of second**

**kind.** This probability is given from:

$$\beta = \int_{-\infty}^{t_{cut}} g(t|H_1)dt$$

The probability  $1 - \beta$  is called **power** of the test and describes the probability of rejecting the null hypothesis correctly. All the above are summarized in **Figure B.0.1**.

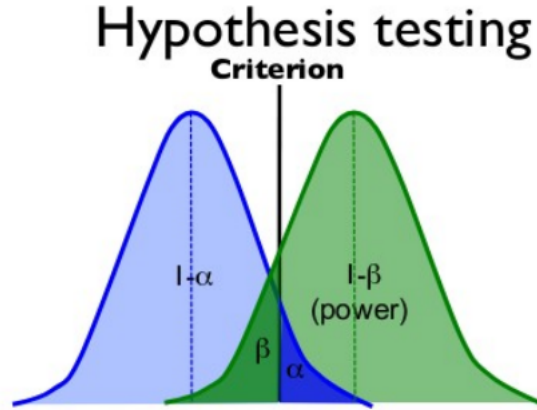


FIGURE B.0.1: Illustration of the type one error probability  $\alpha$ , type two error probability  $\beta$  and power  $1 - \beta$  of a statistical test.

An equivalent way of testing a hypothesis is via the p-value. The p-value is a function that quantifies how often, if an experiment was repeated many times, one would obtain data as far away (or more) from the null hypothesis as the observed data, assuming the null hypothesis to be true:

$$p = \int_{t_{obs}}^{\infty} g(t|H_0)dt$$

The decision of the p-value test is based on the definition of the significance level. If  $p \leq \alpha$ , then the null hypothesis is rejected. If  $p > \alpha$ , the null hypothesis is not rejected. In general, small values of the p-value indicate great incompatibility between the data and the null hypothesis.

## THE MAXIMUM LIKELIHOOD METHOD

Let us suppose we have a dataset of  $N$  measured quantities,  $\mathbf{x} = (x_1, x_2 \dots x_N)$ , where the measurements  $x_i$  are statistically independent and each follows a probability density  $f(x_i, \boldsymbol{\theta})$ . Here  $\boldsymbol{\theta} = (\theta_1, \theta_2 \dots \theta_m)$  is a set of  $m$  parameters with unknown values to be estimated. The joint probability density function for the observed values  $\mathbf{x}$  is given by the likelihood function [1]:

$$L(\mathbf{x}, \boldsymbol{\theta}) = \prod_{i=1}^N f(x_i, \boldsymbol{\theta})$$

The Maximum Likelihood estimate of the parameters  $\boldsymbol{\theta}$  are the values  $\hat{\boldsymbol{\theta}}$  for which the likelihood function has its global maximum. Now, let us suppose we measure  $N$  values for  $\mathbf{y} = (y_1, y_2 \dots y_N)$ , where the measurements  $y_i$  are statistically independent and each follows a Gaussian distribution, with a mean value of:

$$E[y_i] = \lambda(x_i, \boldsymbol{\theta})$$

Also, the variances for each individual measurement are taken to be known:

$$V[y_i] = \sigma_i^2$$

Then, the Likelihood function would be written as:

$$L(\boldsymbol{\theta}) = \prod_{i=1}^N \frac{1}{\sqrt{2\pi}\sigma_i} e^{-\frac{(y_i - \lambda(x_i, \boldsymbol{\theta}))^2}{2\sigma_i^2}}$$

It often more convenient to work with the NLL function, which will yield:

$$-2 \ln L(\theta) = \frac{(y_i - \lambda(x_i, \theta))^2}{2\sigma_i^2} + c$$

Maximizing the Likelihood function is equivalent to minimizing the first quantity on the right hand side of the above equation:

$$\chi^2(\theta) = \frac{(y_i - \lambda(x_i, \theta))^2}{2\sigma_i^2}$$

The above function is called the Least Squares function. As it obvious, it can be written that:

$$-2 \ln L(\theta) = \chi^2(\theta) + c$$

Assuming that the standard deviations of each individual measurement are Gaussianly distributed, the results obtained either by minimizing the Least Squares function, or by minimizing the minus 2 times the NLL function are practically the same. In order to calculate the standard deviation of the Maximum Likelihood estimate, we exploit the fact that the standard deviation of Least Squares estimate is obtained from:

$$\chi^2(\hat{\theta} \pm \sigma_{\hat{\theta}}) = \chi_{min}^2 + 1$$

This property of the Least Squares estimator is illustrated in **Figure C.0.1**.

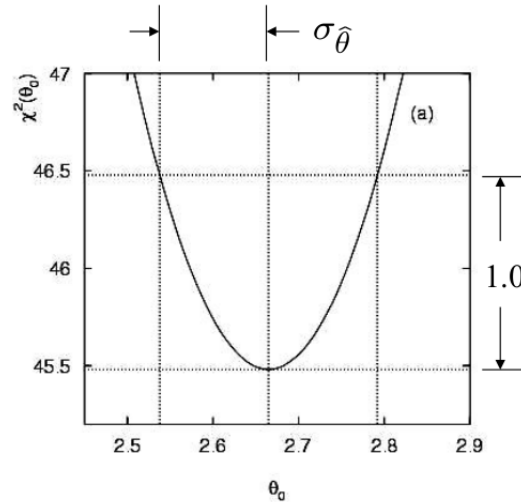


FIGURE C.0.1: The variance of the Least Squares estimator using the graphical method.

Therefore, in order to obtain the Maximum Likelihood estimator, one has to minimize

the minus 2 times the NLL function and ascend by 1 from the minimum to calculate its standard deviation.

## BIBLIOGRAPHY

- [1] Olaf Behnke, Kevin Kröninger, Grégory Schott, and Thomas Schörner-Sadenius. 2013. *Data analysis in high energy physics: a practical guide to statistical methods*. John Wiley & Sons.
- [2] CERN. 2023. *Large Hadron Collider*. <https://www.home.cern/science/accelerators/large-hadron-collider>
- [3] Michael S Chanowitz and Mary K Gaillard. 1985. The TeV physics of strongly interacting W's and Z's. *Nuclear Physics B* 261 (1985), 379–431.
- [4] ATLAS collaboration et al. 2012. Combined search for the Standard Model Higgs boson in pp collisions at  $\sqrt{s}=7$  TeV with the ATLAS detector. *arXiv preprint arXiv:1207.0319* (2012).
- [5] ATLAS Collaboration et al. 2022. Search for resonant  $WZ \rightarrow lv'l'$  production in proton - proton collision at  $\sqrt{s} = 13$  TeV, with the ATLAS detector. *arXiv preprint arXiv:2207.03925* (2022).
- [6] JS Conway. 2011. Incorporating nuisance parameters in likelihoods for multi-source spectra. *arXiv preprint arXiv:1103.0354* (2011).
- [7] Glen Cowan. 1998. *Statistical data analysis*. Oxford university press.
- [8] Glen Cowan, Kyle Cranmer, Eilam Gross, and Ofer Vitells. 2011. Asymptotic formulae for likelihood-based tests of new physics. *The European Physical Journal C* 71 (2011), 1–19.
- [9] ATLAS experiment at CERN. 2023. *Calorimeter*. <https://atlas.cern/Discover/Detector/Calorimeter>

- [10] ATLAS experiment at CERN. 2023. *Detector and Technology*. <https://home.cern/science/experiments/atlas>
- [11] ATLAS experiment at CERN. 2023. *Inner Detector*. <https://atlas.cern/Discover/Detector/Inner-Detector>
- [12] ATLAS experiment at CERN. 2023. *Magnet System*. <https://atlas.cern/Discover/Detector/Magnet-System>
- [13] ATLAS experiment at CERN. 2023. *Muon Spectrometer*. <https://atlas.cern/Discover/Detector/Muon-Spectrometer>
- [14] Joany Manjarres Ramos. 2013. *WZ Diboson Measurements with the ATLAS experiment at the LHC and Performance of resistive Micromegas in view of HL-LHC applications*. Ph. D. Dissertation. Saclay.
- [15] Donna L Mohr, William J Wilson, and Rudolf J Freund. 2021. *Statistical methods*. Academic Press.
- [16] Duccio Pappadopulo, Andrea Thamm, Riccardo Torre, and Andrea Wulzer. 2014. Heavy vector triplets: bridging theory and data. *Journal of High Energy Physics* 2014, 9 (2014), 1–50.
- [17] Alexander L Read. 2002. Presentation of search results: the CLs technique. *Journal of Physics G: Nuclear and Particle Physics* 28, 10 (2002), 2693.
- [18] Mark Thomson. 2013. *Modern particle physics*. Cambridge University Press.
- [19] Maria-Evanthia Tsopoulou. 2022. *Search for New Physics with the Study of Multi-lepton Final States with the ATLAS Experiment at the LHC at CERN*. Ph. D. Dissertation.
- [20] Abraham Wald. 1943. Tests of statistical hypotheses concerning several parameters when the number of observations is large. *Transactions of the American Mathematical society* 54, 3 (1943), 426–482.